DEPARTAMENTO DE ASTROFISICA

Universidad de La Laguna

TRIDIMENSIONAL DISTRIBUTION OF HORIZONTAL VELOCITY FLOWS UNDER THE SOLAR SURFACE

Memoria que presenta
D. Jesús Patrón Recio
para optar al grado de
Doctor en Astrofísica.

INSTITUTO Đ ASTROFISICA Đ CANARIAS

junio de 1994

A la memoria de mi padre,

que me enseñó cómo trabajar con las manos.

ACKNOWLEDGMENTS

The most valuable help that I can conceive in any task to develop is affect, care and comprehension. I appreciate this very much and I thank Don Neff, Guillermo Montijo, Beatrice Müller, Lourdes Ramirez and Charlie Lindsey, because my stay in a foreign country, where I had not been before the begining of this program, and where I came even without knowing the language, has been very much enjoyable. You made me feel at home and, in fact, you have been my family.

Thank you to all the "Astrofísicos Residentes" at the IAC, for so many good moments back home. Specially Quique, Inma, Sole, Ana, Isa, Javi, Ángel and Mikel, for being my family at the Canary Islands. Thank you Quique and Javi, because without you I couldn't have "stop doing silly things and sing the popurrit". Thank you Inma, because you has been my dayly connection with Tenerife all the time, and my good mornings for all your good afternoons. Thanks, Ana, for being my friend Jacinta.

Thank you, my family in Cádiz, for giving me so much love every time I came back home, and having those delicious see food banquets with me.

Thank you, Frank Hill, for your patience, your help, your care and your good sense of humor, in and out the work environment. Thank you for your help in my instalation in Tucson the first time I came to the Wild West. Thanks for taking me to the wonderfull town of San Francisco (and the wonderfull dinner in "The Stinking Rose"). Thank you Frank, for teaching me so much about helioseismology, solar convection and all the scientific production processes in which we have been involved. Thank you for making me a Phd.

I'm gratefull to Teodoro Roca, for such an enthusiastic support to all my step-by-step progressions on my work. Thank you for having made all this possible. Thank you Pere Lluis Pallé, for your support with Teo in this project. And thanks to all the astro-

and helioseismology staff at the IAC for being so interested in my work.

Thank you, Stuart Jeffereis, Tom Duvall and Jack Harvey, for introducing me in the world of the high resolution helioseismology and giving me the oportunity to work directly with an instrument such as the HLH, what is something that I have enjoyed very much.

Thank you John Leibacher, director of the National Solar Observatory during most of my stay there, because you know how to make people to enjoy science and because you know how to enjoy work and life (thanks for a beautiful gliding ride).

Thank you, Ann Barringer, Linda Johnson, Emmerson and all the personnel people at the NOAO for helping me with all my burocratic problems and, sometimes, even the personal ones.

Thank you, Jeannette Barnes, Nigel Sharp, Mike Peralta and all the computer staff for helping me with the day-to-day computer problems. I really appreciate the help of Jeannette, teaching me so many things and tricks about these "dark guys" that the computer systems are.

Thank you, Don Ferris, Warren Bull, Susane, and the rest of the technicians involved in the GONG project, for making my "walking-around-the-basement rests", and my english practice lessons at the Big-A, more confortable and fun.

Thank you, Ed Anderson, Dave Armet, Jim Pintar and all the rest of the people working in the GONG project, for helping me to introduce myself into the GONG data analysis. Thank you Dave for helping me to fight against the OCTANS computer. Thank you OCTANS, anyway.

Thanks to all the spaniards I met at the University of Arizona, for giving me so many fun times. Specially Alberto and Miguel, for being my spanish confessors.

Thank you Lourdes, because you helped me in the very emotional and confusing state of the last months of my work. Thank you for your beautiful smile and for making me happy in my hard moments. Thank you for been such a wonderful friend.

Thanks to Geoff Verderosa (I hope he can make to be the president of the USA some day) and Robert Blackman, for being my housemates and bear with me for two years.

This work has been possible thanks to a grant of the Instituto de Astrofísica de Canarias (Tenerife), and the financial support from the SOI project (Solar Oscillation Investigation), through AURA (Association of Universities for Research in Astronomy), in the last months of my work. I appreciate also the contribution and help of the Astrophysics department of the University of La Laguna (Tenerife) and the National Solar Observatory, this last I thank especially for adopting me as a cientific visitor for about three years, giving me the necesary means to develop my thesis.

Thank you, my keyboard, for giving me so many hours of relaxing and learning about music.

AGRADECIMIENTOS

El afecto, el cariño y la comprensión son la mejor ayuda que se puede prestar a la hora de realizar cualquier tipo de tarea. Yo aprecio mucho esto, y le doy las gracias por ello a Don Neff, Guillermo Montijo, Beatrice Müller, Lourdes Ramírez y Charlie Lindsey, por haber convertido mi estancia en un país extrangero, donde nunca había estado antes de comenzar este programa y a donde llegué sin ni siquiera saber el idioma, en una experiencia inolvidable. Me habeis hecho sentir como en mi casa y, en cierto modo, habeis sido mi familia.

Gracias a todos los Astrofísicos Residentes en el IAC, por tantos buenos momentos de vuelta a casa. Especialmente a Quique, Inma, Sole, Ana, Isa, Javi, Ángel y Mikel, por ser mi familia en las islas afortunadas. Gracias, Quique y Javi, porque sin vosotros nunca me hubiera dejado de tonterías y no hubiera cantado el popurrit. Gracias, Inma, porque has sido mi contacto diario con Tenerife, y mis buenos días a tus buenas tardes. Gracias, Ana, por ser mi amiga Jacinta.

Gracias a toda mi familia en Cádiz, por haberme esperado en todas las ocasiones con tanto amor y haberme premiado con esas deliciosas mariscadas.

Gracias, Frank Hill, por tu paciencia, tu ayuda, tu consideración y buen sentido del humor, dentro y fuera del ámbito profesional. Gracias por tu ayuda a la hora de instalarme en Tucson la primera vez que llegué al Salvaje Oeste. Gracias por llevarme a conocer la maravillosa ciudad de San Francisco (y a la maravillosa cena en "The Stinking Rose"). Gracias, Frank, por enseñarme tanto acerca de heliosismología, convección solar y todos los aspectos científicos en los que hemos estado involucrados juntos. Gracias por haberme hecho un doctor en Astrofísica.

Quiero dar las gracias a Teodoro Roca Cortés, por su entusiasmo y apoyo en todos los pequeños progresos de mi trabajo. Gracias por haber hecho posible todo esto.

Gracias, Pere-Lluis Pallé, por tu colaboración y ayuda junto con Teo en este proyecto. Y gracias a todos los astro- y heliosismólogos del IAC por haberse interesado tanto en mi trabajo.

Gracias, Stuart Jeffereis, Tom Duvall y Jack Harvey, por haberme introducido en el mundo de la heliosismología de alta resolución espacial y darme la oportunidad de trabajar directamente con un instrumento de las características del HLH, experiencia que disfruté mucho.

Gracias, John Leibacher, director del National Solar Observatory durante la mayor parte de mi estancia en Tucson, porque sabes como hacer que la gente disfrute de la ciencia y porque sabes como disfrutar del trabajo y de la vida (gracias por ese maravilloso vuelo en planeador).

Gracias, Ann Barringer, Linda Johnson, Emmerson y todos los miembros de personal del NOAO por ayudarme con todos los problemas burocráticos y, a veces, algunos problemas personales.

Gracias, Jeannette Barnes, Nigel Sharp, Mike Peralta y todos los miembros del centro de cálculo, por ayudarme con los problemas que dia a dia nos causan los ordenadores. Agradezco especialmente a Jeannette por haberme enseñado tantos detalles y trucos acerca de estos tipos siniestros llamados ordenadores.

Gracias, Don Ferris, Warren Bull, Susane y el resto de los técnicos que trabajan en el proyecto GONG, por hacer de mis descansos y paseos por esos pasillos del entresuelo del NOAO, y mis lecciones de inglés en el Big-A, algo mucho más ameno y divertido.

Gracias, Ed Anderson, Dave Armet, Jim Pintar y todo el resto de gente que trabaja en la parte no técnica del proyecto GONG, por haberme ayudado a empezar la toma de contacto con la reducción y análisis de los datos de GONG. Gracias, Dave, por ayudarme a defenderme del ordenador OCTANS. Gracias, OCTANS, de todas formas.

Agradezco a todos los españoles que he conocido en el entorno de la Universidad de Arizona, por haberme hecho pasar tan buenos momentos. Especialmente a Alberto y Miguel, que han sido mis confesores en mi lengua materna.

Gracias, Lourdes, porque me has ayudado muchísimo durante la última etapa de mi trabajo aquí, en la que tantos problemas emocionales he tenido y en la que tan confuso me he sentido. Gracias por tu maravillosa sonrisa y por haberme hecho feliz en los malos momentos. Gracias por haber sido una amiga tan maravillosa.

Gracias, Geoff Verderosa (ojalá que consiga ser el presidente de los EEUU algún dia) y Robert Blackman, por haber sido mis compañeros de piso y haberme podido aguantar durante dos años.

Esta tesis ha sido posible gracias a una beca concedida por el Instituto de Astrofísica de Canarias (Tenerife), junto con un contrato temporal del proyecto SOI (Solar Oscillations Investigation), a través de AURA (Association of Universities for Research in Astronomy), en los últimos meses de mi trabajo. A ello han contribuido tambien el departamento de Astrofísica de la Universidad de La Laguna (Tenerife) y el National Solar Observatory. A este último le agradezco el haberme adoptado como científico visitante durante tres años, facilitándome en todo momento los medios necesarios para desarrollar esta tesis.

Gracias, teclado mío, por haberme proporcionado tantas horas de relajo y haberme ayudado a aprender todo lo que he aprendido acerca de la música.

Contents

ABSTRACT

In the past years the accurate measurements of the amplitudes, widths, and frequencies of the solar oscillations have been reflected in good estimations of the frequency splittings, results that have been inverted to infer the rotation rate as a function of depth. In this work we are going to present a method to infer the distribution of horizontal velocity flows underneath the solar surface as a function of depth and position in the solar disk.

The new techniques are based in a tridimensional power spectrum of the solar oscillations for high spatial resolution images. Information about the two components of the k number of the modes can be obtained in this way, and the tridimensional aspect of the ridges of the p-modes can tell us about horizontal velocity fields.

The data we have used for this purpose are full-disk dopplergrams, obtained with the Magneto-Optical Filter at the Mt. Wilson 60-Foot Tower, with a resolution of about 2.2 arcsec at center of the image, and covering a time period of three days, 3–5 July, 1988.

A classic model of a Lorentzian profile in frequency has been adapted and fitted to this tridimensional view of the oscillations, where the dependence with the two components of the k number are bound to the components of the horizontal velocity field. A distribution of the velocity as a function of frequency for p-modes $n = 0$ to 7, has been inferred, and an inversion process has been developed in order to obtain an estimate of the distribution with depth of these velocities.

Finally, we applied all this analysis to 9 different sectors of the solar disk around the center, being able then to show, as a last result, a tridimensional distribution of the horizontal velocity flows in the upper convection zone.

The results show that the horizontal velocity field appears to execute a spiral as a

funtion of depth. The magnitude of the flows are on the order of 100-200 ms^{-1} in the outer 20 Mm, rising to several hundred ms^{-1} at 50 Mm. The flows present a spatial coherence at almost every position and depth from the surface until about 20 Mm. Below that the spatial coherence dissapears. Three east-west shear layers can be found at almost all longitudes and latitudes, associated in depth with the ionization zones of hidrogen and helium in the outer 20 Mm. Finally, there is an indication of the presence of a toriodal convective roll at about 10° North latitude.

RESUMEN

Los últimos progresos en las medidas de amplitudes, anchuras y frecuencias de las oscilaciones solares se han visto reflejados en unas buenas estimaciones de los desdoblamientos de las frecuencias, datos que han sido invertidos para inferir el ritmo de rotación solar bajo la superficie. En este trabajo vamos a presentar un método para estimar la distribución de flujos de velocidades horizontales en función de la profundidad y la posición en el disco solar.

Estas técnicas se basan en espectros tridimensionales de las oscilaciones para imágenes de alta resolución espacial. Es posible obtener información acerca de las componentes del número de onda, k, y el aspecto tridimensional que los clásicos *ridges* adoptan nos pueden dar idea acerca de los flujos de velocidades horizontales.

Los datos utilizados consisten en imágenes del corrimiento Doppler del disco solar, y se obtuvieron con el filtro magneto-óptico en la torre solar de 60 pies en Mt. Wilson. La resolucioón de las imágenes es de unos 2.2 segundos de arco en el centro de la imagen, y los datos corresponden al periodo del 3 al 5 de Julio de 1988.

Hemos adaptado un modelo de perfil lorentziano para la dependencia con la frecuencia a este espectro tridimensional, donde la dependencia con las componentes del número de onda está ligada a las del campo de velocidades. Como resultado, hemos obtenido la distribución de la velocidad en función de la frecuencia para los modos p de orden $n = 0, 7$ y mediante un proceso de inversión esta distribución se ha transformado en una dependencia con la profundidad.

Finalmente, se ha aplicado todo esto a 9 secciones distintas del disco solar cerca del centro, obteniéndose así un mapa tridimensional del flujo de velocidades horizontal en las capas superiores de la zona de convección.

Los resultados muestran que el campo de velocidades horizontal cambia su orientación en función de la profundidad de forma espiral alrededor de más de 360°. La magnitud de las velocidades es del orden de 100-200 ms^{-1} hasta unos 20 Mm de profundidad, subiendo a valores de varios cientos a 50 Mm. Los flujos presentan una coherencia espacial en casi todas las posiciones y profundidades desde la superficie hasta una profundidad de unos 20 Mm, a partir de la cual la coherencia desaparece. En esta región aparecen tres zonas de valores máximos en las velocidades, aproximadamente a la misma profundidad en la dirección este-oeste para todas las longitudes y latitudes. Estas zonas en profundidad se encuentran muy cerca de las zonas de ionización de hidrógeno y helio. Finalmente se han encontrado indicaciones de la presencia de una celda convectiva toroidal entre el ecuador solar y unos 10° de latitud Norte.

Chapter 1

Introduction

As the closest laboratory that astrophysicists have for their 'experiments', the Sun has proven to be the most efficient tool for studying the physics of the stars. By studying the solar structure and dynamics, more precise and reliable stellar models can be built and many of the questions that remain after the study of the distant stars may be answered.

Basically, the first step after some phenomenon has been observed in the Sun is to describe the most relevant characteristics of the observations. On the background of a relatively quiet solar disk, a variety of very interesting features are present. Starting with the homogeneous granulation and going through the supergranulation, more inhomogeneous and transitory features are found, such as plages, flares, sunspots and active regions. Of special interest is the time evolution of these phenomena, of which the most remarkable feature is probably the solar cycle. The solar magnetic activity is also a very important factor, probably related to most of the features enunciated above.

In order to find answers to the questions about the observed features of the Sun, a good understanding of the regions located immediately below the solar surface, where

solar activity is observed, is necessary. We know that the region under the photosphere is dominated by convection. Therefore, it is essential to study the flows of material and how they evolve in the outer layers of the photosphere.

1.1 Hydrodynamics and magnetism overview

1.1.1 Convection

Besides radiation, convection is the other important way energy is transported in stars. Many stars evolve through some convective stages during their lives. Theories of stellar evolution prove that the Sun, with its mass and luminosity characteristics, should have a convective envelope surrounding a radiative core. What we actually 'see' and measure on the Sun is the surface of this convective envelope. It is reasonable to think that many of the features observed at the solar surface must be directly and indirectly related to convection processes. This emphasizes the importance and necessity of a good understanding of the convection. Reviews about convection can be found in Gilman (1986) and Stix (1991).

Most of the stellar convection theory is based in the mixing-length theory: a buoyant fluid element rising in a superadiabatic layer will move some distance l, called the mixing length, before exchanging its heat and momentum with its surroundings and falling back. This theory is related to the Boussinesq approximation (Spiegel & Veronis 1960) of a nearly incompressible fluid, simplifying considerably the calculations. Nevertheless some nonlinear compressible convection models have been developed (Ogura & Phillips 1962, Gough 1969). For the latest work in convection models see Rast & Toomre (1993), and references thereafter.

The mixing length is related to the local scale height H, thus a fixed ratio l/H, around unity, is chosen. The depth of the convection zone can be estimated from solar

models for temperature and superadiabatic gradient (Gough & Weiss 1976). Standard solar convection models give a depth between 20% and 30% of $R_\odot$. Helioseismology has improved our measurements of the convection zone depth, the lastest results being the determination of the bottom of the convection zone at a depth of 0.287 of $R_\odot$ by Christensen-Dalsgaard *et al.* (1991) from measurements of the sound speed in the solar interior.

Observational evidence of convection

Visual analysis of both Doppler velocity shifts and intensity variations on the Sun suggests a discrete distribution of spatial frequencies, interpreted as a discrete distribution of convective flows or cell sizes. Evidence for this discrete distribution of sizes is provided by the existence of granulation, mesogranulation and supergranulation. Evidence of giant cells will be discussed below. The spatial size of the convective cells is thought to be of the same order as their depths. Thus, by measuring the dimension of a convective cell, an estimate of the bottom of different convective structures can be obtained.

Granulation is the most obvious of the convective cells. Alternating dark and light patterns in intensity measurements are correlated with upward and downward moving material, with velocities on the order of 700 ms^{-1} and 1100 ms^{-1} respectively (most of the numeric values in this section have been extracted from Gilman 1986, and Stix 1991). The average size is 1.4 Mm, and thus so is the estimate of the bottom of the cells in depth. Horizontal flows at the bottom of the granulation of 900 ms^{-1} have been proposed. The observed lifetime of granulation is from 5 to 12 minutes.

Mesogranulation and supergranulation do not show as clear a photometric signature as does the granulation. Sizes of mesogranulation are of the order of 5-10 Mm, showing velocities of 60 ms^{-1}, and lifetimes of 2 hours. An average size for supergranulation is

30 Mm. Upward flows are of 200 ms^{-1}, and of 50 ms^{-1} down into the Sun. Nevertheless, the horizontal flows are estimated to be as high as 300–500 ms^{-1}. Supergranulation can last as long as days, but an average lifetime is of the order of 20 hours.

It is widely suggested (Simon & Leighton 1964, November *et al.* 1981) that the bottom of the convective cells: granulation, mesogranulation and supergranulation, coincides with the ionization zones of H^+, He^+ and He^{++}, located at depths of about 2 Mm, 6 Mm and 20 Mm, respectively. The clearest evidence for this is provided by the granulation: most of the obtained velocity flow profiles in depth for the rotation rate show a maximum around the H^+ ionization zone. The cause of convective driving in these ionization zones is not very clear since it depends on many factors. A possible theoretical explanation is that in each region of partial ionization, the opacity rises, and latent heat of ionization can be released or absorbed in a rising or sinking fluid element; the effects both enhance convective instability. But the contribution to opacity from He ionization is quite small compared to that of H, and no opacity 'bump' generally appears in solar models at the levels of He ionization.

Global circulation

Meridional circulation, differential rotation and giant cells are referred to as global circulation velocity flows. It is important to relate these flows to convective structures, to understand not only the spatial distribution of the flows, but also the changes with depth.

Studies of the variation of the angular rotation rate with depth have been done. Foukal (1972) proposed that, as sunspots are presumably 'anchored' at some depth below the solar photosphere, their faster rotation rate can be interpreted as evidence of an increasing angular velocity with depth, at least for the outermost 10–20 Mm or so. Several results from helioseismology analysis show a peak in the rotation rate very

close to the solar surface (F. Hill *et al.* 1988, Korzennik 1990). A faster rotation rate for the solar interior has been proposed as a mechanism to explain the solar oblateness, as detected by Dicke & Goldenberg (1967), H. Hill *et al.* (1974), and H. Hill & Stebbins (1975), however, this is controversial.

The convection zone may influence the form of the differential rotation seen in the photosphere. Differential rotation could result from the interaction of rotation and convection, through the action of Coriolis forces. Actually, the detection of north-south meridional flows would be very helpful for theories of solar differential rotation, and some evidence for meridional circulation has been obtained (Howard & Gilman 1986).

Finally, there is a controversy about the existence of giant cells, convective structures of sizes of the order of 100 Mm or more. The evidence for such structures is weak (Howard 1979, LaBonte *et al.* 1981, Schröter *et al.* 1978) due to the low amplitudes of the surface velocity flows (about 10 ms^{-1}) compared to other flows, their large scale, and the necessity of long time observations. But several theories predict their existence. As suggested by Simon & Weiss (1968), even when the fluid is compressible and the stratification encloses several density scale heights, convection which extends from the bottom to the top is favored in both linear and non-linear models. As the bottom of the convection zone is at 30% of the solar radius and the horizontal and vertical dimension of the convective cells are thought to be equivalent, patterns of about 200 Mm should be observed in the solar surface. They are weak, but the lifetime is long, which can help their detection. There are models predicting nonaxisymmetric shapes of possible giant cell structures (Durney 1970, Hart *et al.* 1986), or other orientations that may be related to the solar cycle, such as torsional oscillations (Howard & LaBonte 1980, Snodgrass & Howard 1984).

Theoreticians have sought to explain the lack of success in detecting large convective cells. The most plausible is the deflection of the velocity flow from primarily vertical to mostly horizontal (van Ballegooijen 1986), and the observed maximum in the

rotation rate in the layer close to the H^+ zone may be evidence of such a process. Fluctuations in pressure can modify the density fluctuations, and therefore changes in the buoyancy forces can be produced. These fluctuations in pressure and buoyancy forces can decelerate the vertical motions, leading to strong horizontal shearing motions. It is possible that these fluctuations happen in the unstable H and He ionization zones (Latour *et al.* 1983).

1.1.2 The solar cycle and dynamo problem

The idea of a dynamo process in the Sun is motivated by the necessity of the maintenance of the solar magnetic field: the movement of conducting fluid across the magnetic field lines could prevent the magnetic field dissipation. Therefore, global-scale motions in the Sun are likely to be related to the dynamo process, such as giant-cell convection.

Solar activity is the most distinctive feature of the solar magnetic field and the solar activity cycle (bands of magnetic features moving from the Pole to the equator in both hemispheres in periods of 22 years) is one of the observed features of the solar dynamo. The relation between the solar dynamo and the convection is probably reflected in the activity patterns and the solar cycle. Basically, two mechanisms have been found to be the immediate cause of activity: advection of magnetic flux tubes upward by the convection; or magnetic buoyancy: an isolated flux tube in lateral total pressure and thermal equilibrium with its surroundings will be less dense and, therefore, buoyant (E. Parker 1955a).

A very interesting dynamical problem is introduced by the competition between buoyancy effects and the Lorentz force in interaction with magnetic fields. This problem is based on the different rate of diffusion of dynamical components like buoyancy

forces, magnetic pressure, magnetic tension, etc., producing the so-called magnetoconvection problem (Cattaneo 1993, private communications). Magnetoconvection provides a theoretical foundation for most of the photospheric and subphotospheric magnetic phenomena from a dynamical point of view.

Activity shows patterns of sizes that match the giant cells; but we still have no evidence of the existence of giant cells. One of the strongest links between global circulation and activity is the correlation between the torsional oscillations detected by Howard & LaBonte (1980) and the solar cycle. Torsional oscillations consist of alternating east-west oriented bands of moving material, parallel and quasi-symmetric with respect to the equator. These bands originate at high latitudes and move towards the equator over a period of about 22 years. The average velocities are 3 ms^{-1}. Solar activity is very much correlated with the shape of these bands, and is mostly located in the poleward boundary of the fast zones (bands moving faster than rotation).

1.1.3 Questions and answers

Of all the questions about convection and dynamo processes in the Sun, the distribution of velocity flows in the convection zone is very important. It could be useful to clarify many unclear aspects of convection and dynamo theories such as:

1. Where is the bottom of the convective cells?

2. Do giant cells exist?

3. What is the shape and structure of the global circulation?

4. What is the rotation rate in the solar envelope?

5. How do the convective flows evolve over the solar cycle?

Reliable determinations of the depth dependence of the rotation rate could address questions 1 and 4. Bumps seen in the radial profile of the rotation rate may be due to instabilities that drive the convective cells, such as the one found close to the H^+ zone.

Local studies of large scale velocity flows near the solar surface, along with their depth dependence, are necessary to clarify questions 2 and 3. Measurements of the surface distribution of velocity flows have been made (Howard & LaBonte 1980, Howard & Gilman 1986), as well as the depth dependence of the rotation rate (Deubner *et al.* 1979). But in previous studies, the horizontal dependence of the flows is lost as we go deeper under the photosphere.

Finally, temporal variations of these flows may be correlated to the solar cycle (question 5). This correlation may be used eventually to predict the solar activity.

As presented in the next section, helioseismology gives us the tools for the determination of the distribution of the velocity flows, not only with depth, but also with spatial horizontal resolution. Thus a tridimensional map of the horizontal velocity flows can be obtained.

1.2 Helioseismology overview

Helioseismology has proven to be a very useful tool to provide information about the solar interior. While the neutrino problem is not yet solved and is the source of some controversy between the nuclear and particles physics and the solar models (Gough & Toomre 1991), new techniques in seismic investigation of the sun and stars have been developed. They continue to evolve, obtaining more accurate measurements of frequencies, amplitudes, widths and rotational splittings of the acoustic modes of the oscillations.

Since the first detection of the 5-minute oscillations of the Sun by Leighton *et al.* in 1960 (Leighton *et al.* 1962), the physics of the helioseismology has been incorporated into stellar physics, and oscillations have become one of the many phenomena that describe the stars. Ten years after Leighton's work, Ulrich (1970) and Leibacher & Stein (1971) suggested the existence of resonant acoustic cavities under the solar surface; this was observationally-demonstrated later by Deubner (1975), Rhodes *et al.* (1977), and others. The observations of Claverie *et al.* (1979) provided the first confirmation of the global character of the modes. Undoubtedly, by studying the seismology of the Sun we can obtain a lot of information and answer many questions about the physics of the stars that would be difficult to otherwise get. Of special importance is the development of models of stellar interiors (Christensen-Dalsgaard 1988), for which more direct information is necessary.

The sun oscillates, in 10^7 modes. Modes of oscillation with different spatial patterns and temporal frequencies are visible at the solar surface. A Dopplergram of the solar disk, from which other line-of-sight relative velocities (i.e., solar rotation, earth rotation and translation, etc.) have been removed, shows the oscillations: an apparently random pattern of material moving in the radial direction. A spatial and temporal Fourier analysis of this pattern shows thousands of peaks in the frequency domain, corresponding to the modes of oscillation.

Small instabilities in pressure and density are the cause of the oscillations. When instabilities occur, distinct forces try to restore the equilibrium state. Under specific conditions, the restoring force drives a periodic movement of material resulting in an oscillation. When the restoring forces are dominated by pressure, the mode is an acoustic mode, or p-mode; when the restoring forces are dominated by gravity (i.e. buoyancy), the mode is a gravity mode, or g mode. Several attempts have been made to detect the g modes, but with little success so far, due to their small amplitude and low frequency. The 160-minute oscillation may be a g mode, but this is unlikely since it is an isolated peak (Severny *et al.* 1976, Brookes *et al.* 1976, Brown *et al.* 1978). From now on, all

references to modes of oscillation in this dissertation refer to acoustic modes only.

A single mode is characterized by its spatial distribution, given by a global pattern of the moving material in a volume of the Sun. A frozen picture of a mode appears as nodal lines of resting material with sectors of material moving back and forth in the radial direction. Nodal lines are distributed in the three spatial directions: two horizontal directions in the surface, and the depth in the solar globe. Different modes have different number of nodal lines. Each mode is defined by three 'quantum' numbers: the radial order n, that is the number of nodal lines in the radial direction; the degree l, that is the total number of horizontal nodal lines on the solar surface; and the azimuthal order m, the number of nodal lines in a chosen azimuthal direction typically perpendicular to the rotation axis. Oscillations are present in the Sun in all directions, thus horizontal nodal lines appear at each orientation on the solar disk. If the Sun were to be spherically symmetric, there would be a degeneracy in the azimuthal number m: the frequency value corresponding to the solution of the eigenvalue problem (enunciated below) is not a function of m. However, the sun is not spherically symmetric, the most important asymmetry being the rotation. Rotation breaks the azimuthal degeneracy, thus we choose the rotation axis as the azimuthal direction. This non-degeneracy allows us to infer the rotation rate as a function of depth $\Omega(r)$. The rotation rate has a direct influence in the splitting of the frequencies due to the dependence on m: horizontal flows, like rotation, produce advection of the wave pattern, with a subsequent Doppler shift of the frequencies for every m. By measuring these splittings, we can infer $\Omega(r)$, or other horizontal flows in any orientation, by means of inversion techniques (see Chapter 4).

In physical and mathematical formulations of the oscillations (see Unno *et al.* 1989 and Brown *et al.* 1986 for instance), the numbers n , l and m are discrete (and integer) values of an eigenvalue problem. An eigenfunction of the problem is characterized by a set of n , l and m numbers that, at the same time, correspond to a discrete frequency value ν . Valid solutions to this problem result in constraints on these numbers:

$-\infty < n < +\infty$, $l \geq 0$, $|m| \leq l$. Modes of positive n are defined to be p modes, and modes of negative order n are defined as g modes; the $n = 0$ mode is called the f mode, or fundamental mode. The boundary conditions limit the radial extension of the modes to the so called resonant cavity, delimited by two turning points. Outside this cavity, modes decay. The outer turning point is virtually the same for all modes and is located at the solar surface. The decay of the modes into the solar atmosphere makes them detectable. The inner turning point is different for every l, n pair. This is very fortunate for us: by studying modes of different degree and order we are studying properties of the sun at different depths. Modes of lower degree and higher order travel deeper into the Sun.

A wave, generated at some moment somewhere in the sun, begins the travel in any direction but, due to the stratification of density and the temperature gradient, the wave front will be refracted as it travels. There will be two reflections (the two turning points referred above): one at the surface, due to the rapid variation of the scale height near the solar surface, and another at a certain depth depending on the mode[1], where the refraction makes the wave travel horizontally and reflect backup towards the surface (Figure 1.1 is an schematic plot of this picture). Only modes that resonate between these two turning points survive a destructive interference, and this only happens when there is an integral number of vertical wavelenghts fitting in the cavity defined by these two points:

$$\int_{r_0}^{r_1} K_v(r)dr = n\pi + \varepsilon,$$

where r_0 and r_1 are the turning points, $K_v(r)$ the vertical wave number and ε is a correction factor. This expression defines a relationship between degree (through $K_v(r)$) and frequency called the dispersion relation. The order n of the mode defines this integral relation and determines the discrete frequency values for every given horizontal

[1] Except for the mode $l = 0$ that has no lower turning point: the wave front is parallel to the stratification of density and no refraction of the wave front is produced. The result is that the wave travels through the center of the sun and reaches the surface at the other side.

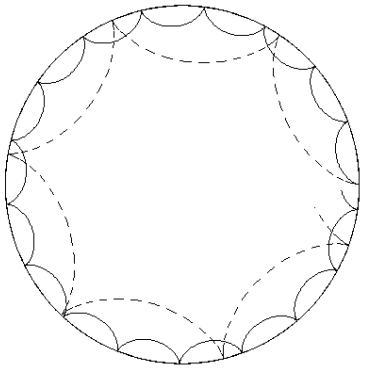

Figure 1.1: Schematic picture of the rays of the oscillations. The reflecting inner point of the higher degree mode (dashed line) is deeper than that of the lower degree (solid line).

wave number, or degree l. Based on this relation, a diagram of frequencies as a function of degree can be plotted, and ridges appear for every order n. Figure 1.2 shows the experimental proof of this relation for a 8-day set of data obtained with the GONG[2] instrument (Harvey 1988) in November 1-8, 1992. The ridges correspond to orders $n = 3$ (at the lower-right corner) and consecutive increasing n.

It is customary to discuss the power spectrum of the oscillations, a distribution of power in frequency and wavenumber with amplitudes changing from mode to mode due to several causes: finite lifetimes of the modes, instrumental and solar background level, aliasing and leakage of the modes (F. Hill *et al.* 1991a, Patrón 1992). It can be seen in Figure 1.2 that the power of the oscillations is concentrated in the ridges following the dispersion relation. Most of the power is found around 3000 μHz, or a period of 5 minutes.

By fitting the peaks as a function of frequency in the power spectrum, an estimate of the frequency of a given mode can be obtained. Theory tells us that this distribution of frequencies is a valuable tool that can be used to infer, by means of inversion techniques (Chapter 4), the radial distribution of physical quantities such as sound speed, opacity

[2]Global Oscillation Network Group

and dynamical information in general (Harvey 1985).

Observationally, modes of low degree ($l = 0, \ldots, 3$), are detected as variations in the line-of-sight velocities or in intensity of integrated light of the solar disk. But, in order to measure modes of intermediate and high-degree, we must work with images of relatively high spatial resolution: we need to differentiate the pattern of one mode from another. Both techniques provide precise measurements of the frequencies of the

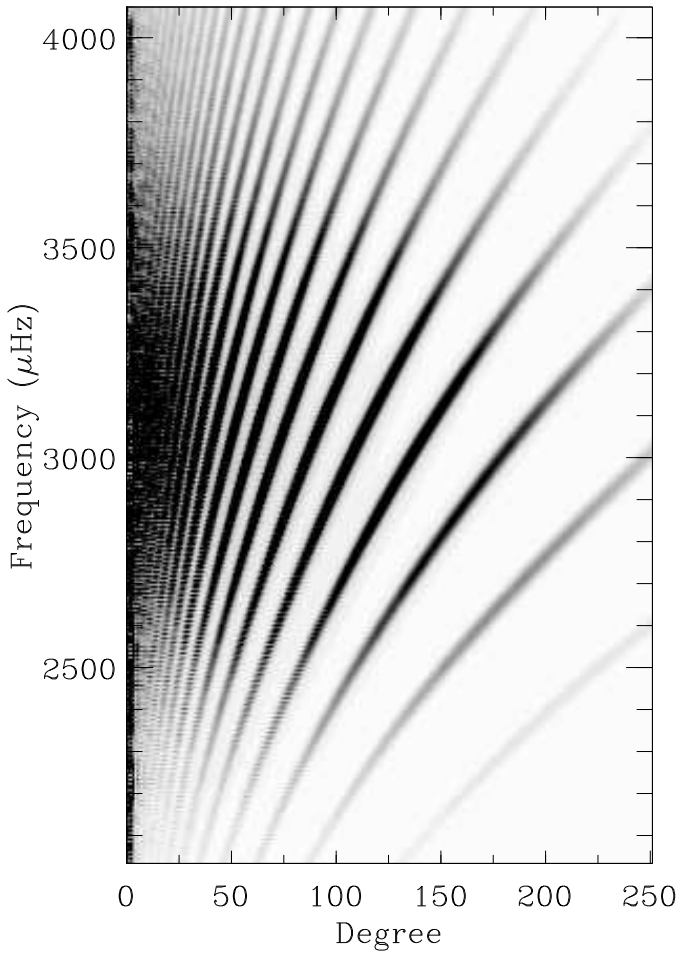

Figure 1.2: Power spectrum of the p-mode oscillations showing the dispersion relation between the frequencies and the degree of the modes for several radial orders n. $n = 3$ for the ridge at the lower-right corner, and increases up and to the left. (Adapted from GONG project data; spectrum obtained for November 1-8, 1992).

modes and, even though the high-resolution techniques give information about a wider range of modes, the accuracy is currently better for results obtained with non-imaging techniques. This is due to the longer time spans of data available in the latter, and, it is also easier to design instruments with high stability and precision for non-imaging observations (a good review about the comparison between these different observational techniques can be found in F. Hill *et al.* 1991a).

1.3 About this work

In this dissertation we introduce one of the newest high-resolution techniques for analysis of solar oscillations. It is based in the construction of a tridimensional power spectrum of the oscillations and its interpretation, first suggested by Frank Hill (1988).

The standard way of analyzing high-resolution images for helioseismic purposes has been the spatial decomposition of the image into spherical harmonic coefficients. The functional solutions of the oscillation problem are proportional to the spherical harmonics, and the final measured amplitudes (i.e. velocity or intensity at the surface) are proportional to a linear combination of these functions, with the corresponding coefficients. Spherical harmonic functions are characterized by a set of l and m values, equivalent to saying that a spherical harmonic function corresponds to a mode of the same l and m values. In order to distinguish one mode from another, a spherical harmonic decomposition is performed. First, a Fourier transform is applied in the direction parallel to the solar equator, followed by a Legendre transform in sine of the latitude. The result is the value of the coefficients of the spherical harmonics, i.e. the coefficients of the modes. Doing this for all the images in the temporal series produces a temporal series of coefficients, and a subsequent Fourier transform in time leads to the power spectrum of the oscillations.

A tridimensional spectrum can be obtained in a similar way. The major difference

is that three Fourier transforms are performed, two in the spatial directions corresponding to the solar longitude and latitude, and one in time. The result of the first two transforms is an image in the spatial transform domain, with axes that are the two orthogonal components of the wave number, **k** (denoted by k_x and k_y), in the directions of solar latitude and longitude. The third Fourier transform in time gives the final power spectrum: the amplitude of the oscillations in frequency for every pair of values (k_x, k_y). The aspect of this tridimensional power spectrum is similar to the result of turning the $k-\omega$ diagram (as in Figure 1.2) around the $k = 0$ line as a revolution body. In fact, the 3–D spectrum is a more complete representation of the spectrum, and the two-dimensional diagram is more properly the result of an azimuthal average, at constant k number, of the tridimensional one. Ridges of constant radial order become surfaces with a shape reminiscent of trumpets.

The most interesting feature of this kind of diagram [3] is that we retain spatial information in the horizontal plane k_x-k_y . As we will see later in Chapter 3, the asymmetries of these tridimensional surfaces from the axis $k_x = k_y = 0$ can be interpreted as the advection effect of the wave front of the oscillations by horizontal velocity flows under the solar surface (Gough & Toomre 1983). An estimation of the values of these velocities may be obtained by measuring these asymmetries (F. Hill 1988), and the use of inversion techniques can let us infer the distribution in depth of these flows. Another difference between this tridimensional analysis and the two-dimensional one is that in the former, we can perform a local analysis of the data, taking relatively small sections of the total image; in the standard power spectra all the available data are used in the same transformation process to get a single power spectrum that averages all the local effects in a global analysis. It is important to keep in mind the local or global character of the modes. But we will come back to this point in the last section of Chapter 4, where we discuss the solar model used in the inversions.

[3] In chapters 2 and 3 we will describe the data, the reduction procedure and the way to get such tridimensional spectra.

The final goal is to apply this technique to different positions on the solar surface and make a map of the horizontal velocity flows as a function of position and depth, thus, we get local information rather than global. Variations of the horizontal velocities both with position and depth provide valuable information about the dynamics of the regions under the solar surface, the convection, and the dynamo and solar cycle problems. The study of correlations between the distribution of the magnetic structures on the surface of the Sun and the distribution of the velocity fields below this surface, should shed light on the causes of active regions and sunspots. Of special interest would be the detection of horizontal velocity flows as a confirmation of the existence of the giant cells.

The data used for this purpose are a time series of 1024×1024-pixel dopplergrams, processed after the two filtergrams in the wings of the Na D lines, covering a time period of three days (3-5 July, 1988). The images were obtained with the Magneto-Optical Filter at the 60-Foot Tower at Mt. Wilson Observatory, with a cadence of 60s and a resolution at disk center of 2.2 arcsec.

Chapter 2

Data acquisition and reduction

It seems ironic, but the term 'reduction' is not the most appropriate for a definition of the process of getting the final physical results from the initial raw data. As a matter of fact, we don't 'reduce' anything, but 'increase' at least the amount of information several times. But this is not a semantic dissertation and this question will remain for the linguists. And, in fact, a comparison of the last data results and the raw data shows that the amount of information was reduced in the sense of 'size', if we forget the intermediate results, that can fill the biggest disk of any computer.

The size of the data images is large enough to prevent the automatic execution of the processing steps, and force the storage of intermediate results periodically before ending one single step. This reduction process has been tedious, as everyone could have expected of such a task.

The reduction process described in this chapter will not go all the way through to the last physical results of this dissertation, but will end with the construction of the tridimensional power spectrum. Thus, almost no physics is used in these steps of the reduction, which are mostly geometrical considerations, except for some applications of

a theoretical formulation for the solar rotation rate.

The first section of this chapter is an abstract of the data acquisition process and calibration, leading to the raw velocity images of the solar disk. Since this work has not

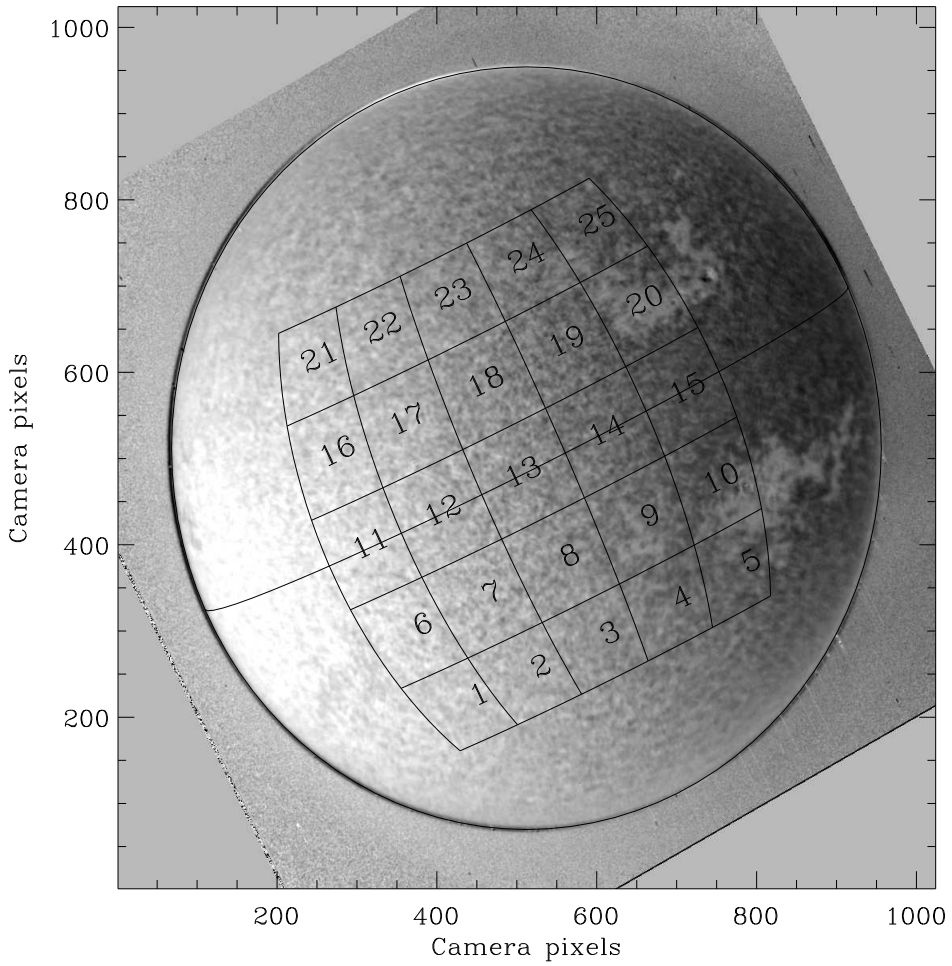

Figure 2.1: Calibrated image of the solar disk showing the solar equator and the limits of the sections under study in this work. It corresponds to 1628 UT of 7/4/88.

been performed by us, we limit the comments to a very summarized description (a whole description of the process can be found in chapter 2 of Korzennik's PhD. dissertation).

These images were taken and calibrated by Edward J. Rhodes, Sylvain G. Korzennik and Alessandro Cacciani, and the final velocity images were kindly provided to us for our analysis.

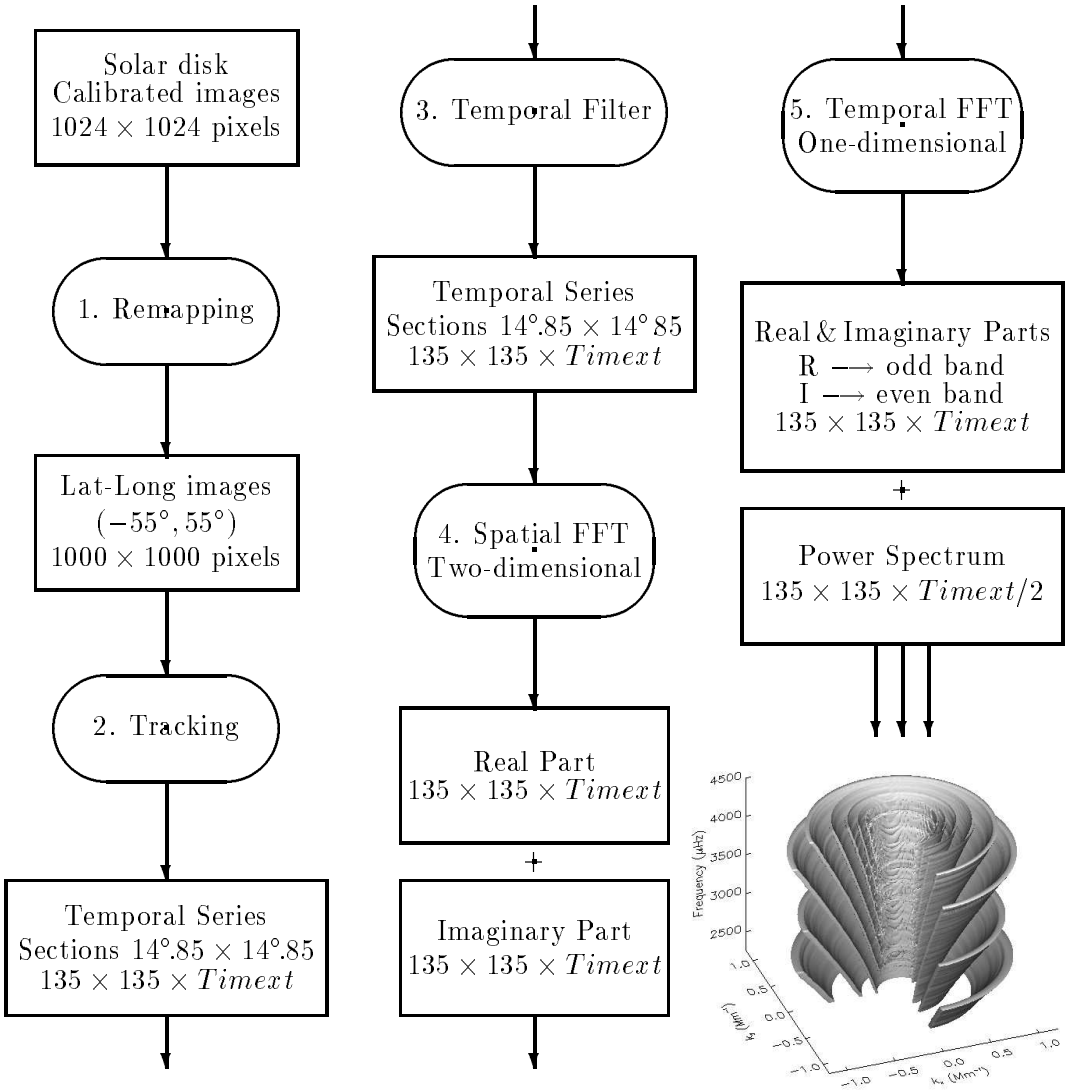

Figure 2.2: The reduction process. The steps appear in ovals and the results inside the rectangles showing the dimension of the images. *Timext* is the temporal span of the data in minutes. A section of a tridimensional power spectrum is showed at the end.

A calibrated Doppler velocity image is shown in Figure 2.1 as an example. It was

taken at 1628 UT of 7/4/88. An overlay shows the solar equator and the limits of the sections considered in this work.

The following sections describe the remainder of the reduction, and a diagram of the process, step by step, appears in Figure 2.2 . The inputs to steps number 1 and 2 are a set of two-dimensional images of the solar disk, up to a number equal to $Timext$ (3456 minutes in our data set if we add the observation time span plus the night time gaps). The remaining results are tridimensional images or sections of the solar disk, up to 9 sections in this study. The following summarizes the different steps in the process with the initial input objects being the calibrated images described in the next section:

1. Remapping of the solar disk images onto a latitude-longitude grid.
2. Tracking of the images to remove the solar rotation.
3. Temporal filtering to remove low frequency fluctuations.
4. Spatial Fourier Transform.
5. Temporal Fourier Transform.

2.1 Data acquisition and calibration

The Mount Wilson 60-Foot Solar Telescope consists in a coelostat system at the top of the tower that directs the beam of light through a focusing doublet objective lens and the field lens. Once in the observing room, a magneto-optical filter (MOF) is used as an imaging Doppler analyzer, consisting in a pre-filter unit, a filter unit, and a wing selector. The pre-filter unit isolates a narrow band around the absorption line (sodium D lines). As the filter unit creates two narrow band transmission peaks in each wing of this line, the wing selector unit absorbs one or the other. First, the two wings of the incoming light are, respectively, right and left circularly polarized, and then, using

a quarter-wave plate, a 90° rotation of the plate selects the red and blue components. Finally, a 1024×1024 pixel CCD camera takes, alternately (5 seconds apart), a red and a blue image of the solar disk, at a sampling rate of one pair of images per minute.

As a first step in the calibration, a 'dark frame' is subtracted from each frame, and a 'despiking' procedure is performed to remove bad pixels. In order to make a geometrically correct calibration, the geometry of the solar disk in the images has to be defined. The center of the disk is calculated by fitting a whole parameterized ellipse (center, dimensions and orientation) to the solar limb, defined to be the maximum of the first derivative of the radial cross-section in intensity at every orientation. The ellipse was fitted to this distribution of points by a non-linear least-squares procedure. Then, the disk is translated to center it on the frame, and rotated in order to bring the principal axis of the fitted ellipse in alignment with the x and y axis of the frame, using a bi-cubic interpolation technique.

A flat field correction was not implemented. If the detector response is linear, the normalization of the Doppler ratio makes the response of the detector insensitive to its gain. Even if the response is not linear the errors introduced by neglecting the non-linear terms are of the order of the ones introduced by the intrinsic non-linearity of the MOF. But, since there is also an interpolation process to center the solar disk in the frame, the averaging effect of the 16-pixel interpolation kernel can be used to estimate the spatial non-uniformity of the detector's response. The levels calculated (Korzennik 1990), are close enough to the seeing noise so that the gain can be neglected.

Next, the Doppler signal of the images is evaluated. A Dopplergram image is calculated as:

$$I_d(i,j) = \frac{I_{red}(i,j) - I_{blue}(i,j)}{I_{red}(i,j) + I_{blue}(i,j)}, \tag{2.1}$$

where I_{red}, I_{blue}, and I_d are the intensities in the red and blue wings, and the final

Doppler ratio, respectively, evaluated for every pixel denoted by the pair (i, j).

In order to obtain the velocity values of the images, a known velocity signal is compared to the Dopplergram images. Three methods have been tested. The first one considers the line-of-sight velocity due to the solar rotation as a reference. A simple linear law can approximate the known values of this velocity at the solar equator as $V = S_0 + K_s I_d$, and a fitting to the measured values I_d along the solar equator gives the coefficients S_0 and K_s.

Another approach is to use the contribution of the earth rotation and translation velocities to the line-of-sight velocity. As the previous case, a linear law can be applied, $V = K_0 + K_t I_d$, where V is, this time, the ephemeris sun-to-earth velocity and the fitting is made in time (actually I_d will be an average over the solar disk).

Finally, non-linear approximations have been tested as well, with expressions like:

$$V = K_0(1 + K_r(r/R)^2)(1 + K_d(I_d)^2)I_d, \tag{2.2}$$

where r is the radius at the current pixel, R the size of the image, and K_0, K_r and K_d the calibration coefficients.

As the non-linearities of the MOF are not very great, the second method was chosen for this data set. The fitting was performed for the three days of the span, and the results are showed in Table 2.1. In Korzennik's work a running mean is applied

date	$K_0(m/s)$	$K_t(m/s)$
7/ 3/88	-765.910	-.295265
7/ 4/88	-747.561	-.302720
7/ 5/88	-732.575	-.302491

Table 2.1: Offset and scale factors of the calibrations.

before the calibration, thus the offset term is removed when the running mean value is

subtracted from the data. In our case, the running mean is applied after the remapping and tracking (explained in the next two sections), and the data we obtained from Rhodes *et al.* were calibrated with this offset term.

2.2 Remapping

The initial raw images are a projection of the solar disk onto a plane. This means that the spatial dimensions on the solar surface depend on the position in the solar image. We cannot use these spatially-dependent pixel resolution images directly, but we must 'remap' them onto another grid. Usually, to obtain the two-dimensional $k-\omega$ diagram, a decomposition into spherical harmonics is performed. But the spatial distribution of these patterns is defined on a solar longitude–sine-of-latitude grid. This grid provides an equally-spaced distribution of data for the Fourier transform in longitude and for the Legendre transform in sine-of-latitude performed in a spherical harmonic decomposition.

Here we do not perform a spherical harmonic decomposition. Asymptotic expansions of these functions show that harmonics of relatively high degree ($l > 10$), can be described as plane waves propagating along great circles. Plane waves are just sine and cosine functions, and a simple Fourier transform is the appropriate tool we need to decompose the data. The following expression represents the distribution of a plane wave on the solar surface for a given mode (if we plot it for $k_x = k_y$ we get something very close to a chess board pattern):

$$f(S_x, S_y) = A\, cos(2\pi k_x\, S_x)\, cos(2\pi k_y\, S_y), \tag{2.3}$$

where f describes the amplitude of the signal at a position (S_x, S_y), A is the amplitude of the oscillations at a given time, and k_x and k_y are the two horizontal components of the spatial wave number k of the mode (here we consider only the real part of the

oscillatory function, a complex exponential). Approximate relationships between k_x, k_y, l and m are $k_x \approx m/R_\odot$ and $k_y \approx (l^2 - m^2)^{1/2}/R_\odot$, where $R_\odot$ is the solar radius (F. Hill *et al.* 1991a).

Equation (2.3) suggests we define the horizontal coordinates S_x and S_y to be the latitude and longitude in a heliographic coordinate system. Remapping our flat disk image onto this coordinate system will give us an equally-spaced distribution of data.

We use the parameters defining the solar limb and center of the disk (described in the previous section) to perform the geometrical transformations. Besides this geometrical information concerning our images, we need to know the orientation of the rotation axis of the Sun, P, the heliographic latitude of the center of the solar disk, B_0, and the apparent radius of the Sun in arcseconds as a consequence of the sun-earth distance projection effect. These parameters were obtained from the Nautical Almanac tables and formulas for the beginning of the time span of every day, and kept unchanged during each span. To keep these values unchanged during a single day time span introduces an artificial drift of the images that has been calculated and represents an extra velocity flow of about 3 ms^{-1}, that is between the error limits of the measured velocities. Table 2.2 shows the values for the three days of data, plus the semiminor

date	P_{eff} (degrees)	B_0 (degrees)	*Radius* (arcsec)	*Xax* (camera	*Yax* pixels)
7/ 3/88	24.22	3.21	943.87	443.91	442.08
7/ 4/88	25.03	3.32	943.87	443.93	442.20
7/ 5/88	25.17	3.44	943.87	443.83	442.03

Table 2.2: Geometric parameters of the Sun and the solar disk image.

and semimajor axis (*Xax* and *Yax* respectively in the table) of the ellipse fitted to the solar disk. The image had already been translated and rotated to align the minor axis of the ellipse with the vertical direction of the frame, and to set the center of the disk to the center of the frame (pixel values 512 and 512). We thus did not vary the ellipse

center and orientation. In Table 2.2 we display not the P angle, but the final addition of this angle and the rotation applied to the image, and call it P_{eff}.

The actual remapping of the data onto an equally-spaced grid in latitude and longitude was achieved by a cubic convolution interpolation algorithm, using a 4 by 4 pixel interpolation kernel. The equations for the geometrical transformations are based on those found in Smart (1971), with some modifications eliminating any approximation. The final lat-long images are 1000×1000 pixels, covering a total interval of $110°$, from $-55°$ to $55°$ in both latitude and longitude and resulting in an angular resolution of $0.11°$. Note that, since the values of B_0 and P_{eff} are not zero, the center of the remapped images at latitude $B = 0°$ and longitude $L = 0°$ does not correspond to the center of the disk. The resolution in the lat-long grid results from matching one pixel at disk center to one pixel in the lat-long grid. As we move towards the solar limb, a pixel in the solar disk image samples larger areas with a subsequent loss of resolution in the angular coordinates L and B. The result is a foreshortening of the data, and the interpolation process fails as we approach the solar limb.

2.3 Tracking

Our goal is to obtain local information at several positions on the solar surface. Then, a local analysis of the data should be performed at different positions for subsections of the total image, which we call subrasters. The next step is to choose these positions and to work independently with every one, i.e. to build a temporal series of data for every subraster. The sections are chosen to subtend $14°.85 \times 14°.85$, or 135×135 pixels in the remapped images. Since the sun is rotating, we need to track every subraster at an appropriate rate. The initial goal was a mosaic of 5×5 subrasters. Due to the foreshortening, we decided to work with 9 subrasters in a mosaic of 3×3 . The position of these subrasters was chosen so that the center of the whole mosaic matched

the center of the total image at a time $Timext/2 = 1728$ minutes, half of the total temporal span. In this way, the subrasters are symmetric around the central meridian of the image, reducing the foreshortening effect.

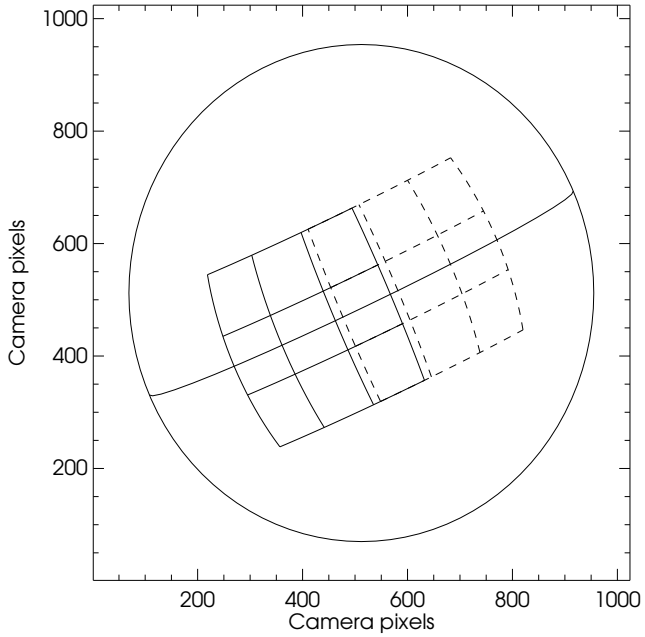

Figure 2.3: Positions of the 9 subrasters selected on the solar surface at the beginning, (solid lines, 1506 UT, 7/3/88), and the end (dashed lines, 0041 UT, 7/6/88) of the time span of the observations. The sides of the squares are 14°.85 in heliographic coordinates.

In Figure 2.3 the positions of the selected subrasters are shown for the initial and final times of the total span. The latitudinal position is centered around the solar equator, and the range in latitude is from $-22°.275$ to $22°.275$. The longitudinal positions were calculated from the beginning and ending time ephemeris values of the heliographic Carrington longitude of disk center: $345°.43$ at 1506 UT, 7/3/88, and $313°.68$ at 0041 UT, 7/6/88, a total angular translation of $31°.75$. Given the size of the mosaic, $14°.85 \times 3 = 44°.55$, and the constraint of centering the mosaic in the center of the total image at half of the time span, we find that the Carrington longitude range of the mosaic is $307°.28$ to $351°.83$. In the lat-long grid the range will be $-38°.15$ to $6°.4$ at

the beginning, and $-6°.4$ to $38°.15$ at the end.

The actual tracking procedure uses a rotation rate expansion in powers of the cosine of the colatitude, $\mu = cos(90° - B)$, from Snodgrass (1984). It gives the total angular rotation as a function of latitude and time span since the beginning of the data run. This amount is added to the initial Carrington longitude for every image taken every minute. The expansion is as follows:

$$dlng(\mu, dt) = C(w_1 - w_2 \cdot \mu^2 - w_4 \cdot \mu^4 - sw)dt, \tag{2.4}$$

where $dlng$ is the rotation rate in degrees, $C = 360 \cdot 10^{-9}$ is a constant of proportionality, dt is the elapsed time since the beginning, $w_1 = 452n$Hz, $w_2 = 49n$Hz, $w_4 = 84n$Hz are the coefficients, and $sw = 31.7n$Hz is the sidereal to synodic correction. Instead of calculating this value for every latitude, we use a unique value evaluated at the center of every subraster for the total range of latitudes in each subraster.

Once the position in latitude and longitude corresponding to the time the image was taken is found for every subraster, we assemble the temporal series of subrasters, again using a cubic convolution interpolation process. The result is a set of images of dimensions $135 \times 135 \times Timext$. Two practical issues need to be solved with these tridimensional images. First, bad data images due to errors, bad seeing conditions, clouds, night time, etc., were rejected and the corresponding band in the tridimensional image was filled with zeroes. Second, the size of the images was quite large. The number of bands in our data, $Timext$, is 3456[1], and the data are 8-bit real pixel values, or 4 bytes per pixel. Thus, the total size of one temporal series is $135 \times 135 \times 3456 \times 4 \approx 252\ Mbytes$. In order to work with the 9 subrasters at the same time, we split the final results into 3 sections, containing only the day time portions of the three days of data. This reduced

[1] This number doesn't correspond to the total number of images plus night time, which is 3408, but is the result of an aspect of the Fast Fourier Transform routine that we will explain later on the temporal FFT section.

the size of the individual images to about 50 *Mbytes*. We then saved the results of every day before removing them from the disk and starting with the next one.

2.4 Temporal filtering

Before starting the tridimensional Fourier Transform process, only one step remained: the correction for low-frequency fluctuations. Oscillations are not the only velocity features present in the Sun. Besides the line-of-sight velocities introduced by

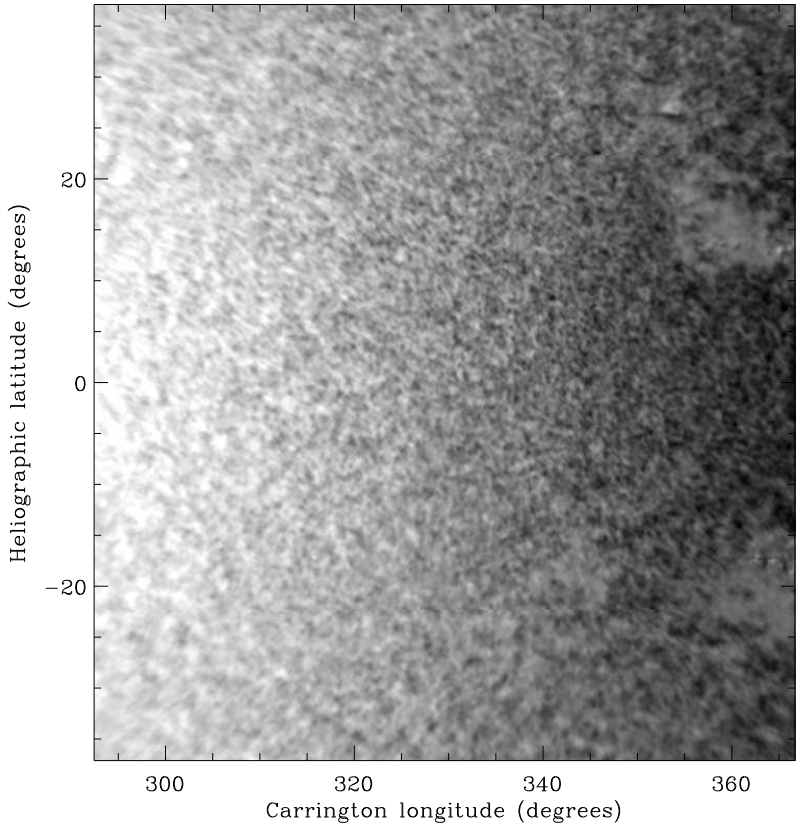

Figure 2.4: Remapped and tracked section before the temporal filtering. It corresponds to the 1628 UT of 7/4/88.

the solar rotation and the earth rotation and translation, local features due to activity and convection structures add their effect to the total Doppler velocity measurements.

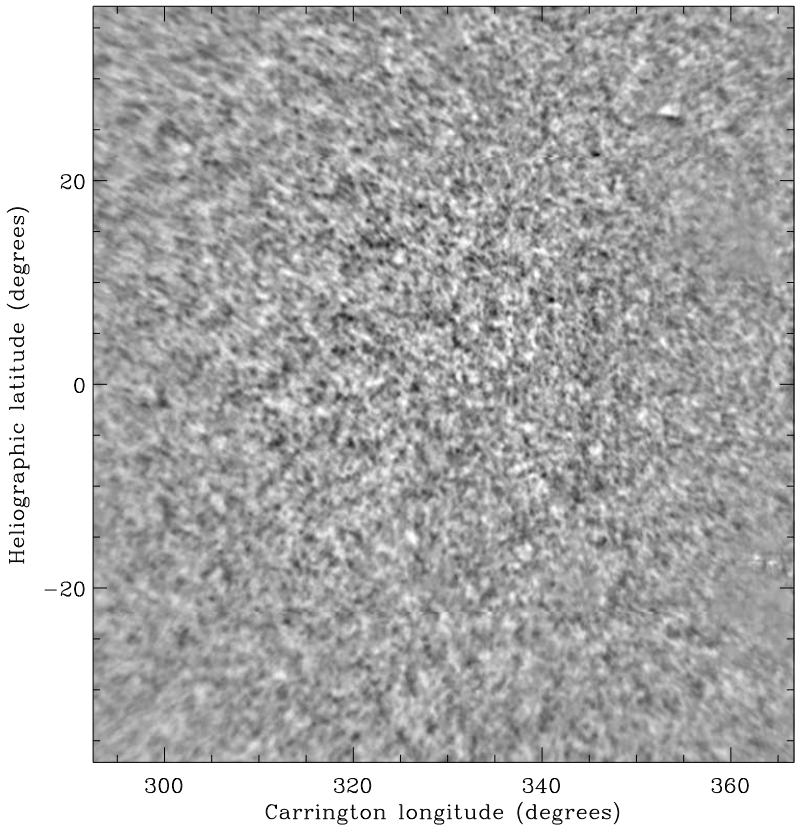

Figure 2.5: The same section as the previous figure after the temporal filtering.

In general, these phenomena are of low frequency in comparison with the oscillations. So, a simple running-mean of the data in time removed from every band of the image will remove the effect of these slowly-evolving features. In our case we used a 21-point running-mean, taking 11 points before and after the pixel in consideration, calculating the mean value of the total 21 points and subtracting this value from the central one, pixel by pixel in the whole tridimensional image. Zero bands were not taken

into consideration. In Figures 2.4 and 2.5 we show a section of the lat-long grid, corresponding to the 25 selected subrasters, before and after the temporal filtering. Bright patterns are material moving outward in the radial direction while dark patterns show material going inward. The residuals that appear in Figure 2.5 are the signature of the oscillations on the solar surface. The contrast of Figure 2.5 has been enhanced to show a clearer view of the material going in and out.

As we can see, the solar rotation is mostly removed, along with most of the activity patterns. Still, some of the very strong activity features remain as dark spots at the right side of the picture. This image was generated after tracking 25 different subrasters in a 5×5 mosaic separately, and then putting everything together and building the total image again. As a consequence of both the approximate tracking formula used and the interpolation process, the different subrasters don't match very well in the horizontal edges for higher latitudes (it is difficult to see here, but it is easily seen in the computer screen). Finally, notice how the image is degraded as we go closer to the corners due to the foreshortening.

2.5 Spatial Fourier Transform

In this section we consider only the two spatial dimensions. In the remapping section we introduced the motivation for performing a plane wave decomposition instead of a spherical harmonic decomposition of the data. Here, we present the equations of the decomposition in a more formal and detailed way.

In a plane wave description, the oscillations can be considered as local waves, and ignoring the spherical solar shape these waves can be approximated by plane waves. In this representation, the radial displacement, or the eigenfunction correspondent to the

radial component of the contribution of all the modes is (F. Hill *et al.* 1991a)

$$\delta r = \Re \left\{ \sum_{n,l,m} K_{ln}(r)\, e^{\,i(\omega\, t - \mathbf{k}_h \cdot \mathbf{x})} \right\}, \tag{2.5}$$

where $\Re$ is taking the real part, $K_{ln}(r)$ is the radial dependence of the eigenfunction associated to the mode, which is vibrating at a frequency $\nu_{n,l,m} = \omega/2\pi$, $\mathbf{k}_h$ is the horizontal wavenumber vector, and $\mathbf{x}$ is the displacement vector in a horizontal coordinate system on the solar surface. The magnitude of $\mathbf{k}_h$ is related to the degree of the modes by

$$k_h = \sqrt{l(l+1)}/R_\odot, \tag{2.6}$$

with $R_\odot$ being the solar radius. The radial velocity field V_r associated with the oscillations, measured at the solar surface, can be written as a superposition of the normal modes:

$$V_r(t, S_x, S_y) = \Re \left\{ \sum_{n,l,m} A_{n,l,m}\, e^{\,i(\omega\, t + \varphi_{n,l,m} - \mathbf{k}_h \cdot \mathbf{x})} \right\}. \tag{2.7}$$

Here, S_x and S_y are the two components of the $\mathbf{x}$, $A_{n,l,m}$ is the mode amplitude, and $\varphi_{n,l,m}$ the phase. To isolate the spatial dependence at a given time t_0 , we can group the amplitude and the temporal dependence as follows:

$$V_r(t_0, S_x, S_y) = \Re \left\{ \sum_{l,m} \left[\sum_{n} A_{n,l,m}\, e^{\,i(\omega\, t_0 + \varphi_{n,l,m})} \right] \, e^{\,-i\, \mathbf{k}_h \cdot \mathbf{x}} \right\}, \tag{2.8}$$

$$V_r(t_0, S_x, S_y) = \Re \left\{ \sum_{l,m} C_{l,m}(t_0)\, e^{\,-i(k_x S_x + k_y S_y)} \right\}, \tag{2.9}$$

where k_x and k_y are the two components of $\mathbf{k}_h$, and $C_{l,m}(t_0)$ will be the spatial coefficients at a time t_0. Now it is clear how to use the Fourier Transform (FFT, since

the actual process will be a Fast Fourier Transform algorithm): a FFT in the S_x direction, followed by a FFT in the S_y direction, will give directly (save some known normalization factor) the values of the coefficients $C_{l,m}$ for every pair (k_x, k_y). In our case we chose (S_x, S_y) to be the lat-long grid; then we applied the FFT row by row in the longitude direction, obtained a new image of the same dimensions, applied the FFT column by column in the latitude direction, and obtained the matrix of coefficients of the modes. The resulting image is a map of the oscillations in the two-dimensional Fourier Transform space, as a function of the components of the wavenumber vector.

These images have the same dimension as the input images, 135×135, and the reference axis $k_x = k_y = 0$ is placed at the center of the image. The resolution of the pixels in these images, as given by the FFT procedure, is $\Delta k = 2\pi/(N\Delta x)$, where N is the number of data in every run of the FFT and Δx is the data resolution. In our case, $N = 135$ and $\Delta x = 0°.11$; but these values will give an angular value for Δk. In stead, we consider Δx in spatial units, $\Delta x = 0.11\,(2\pi/360)\,R_\odot = 1.33673\,Mm$, so the resolution in k number has the appropriate units: $\Delta k = 3.4818 \cdot 10^{-2} Mm^{-1}$. Therefore the images in the $k_x - k_y$ space sample the range $-2.3328\,Mm^{-1}$ to $2.3328\,Mm^{-1}$ in both axes (this value corresponds to $(N/2)\,\Delta k$). We can estimate the corresponding l value for this range using Equation (2.6), and find L_{N_y}, the Nyquist value of $L \equiv \sqrt{l(l+1)}$, which is about 1624 for our images. However, if we look at the final power spectrum (Figure 2.8), we do not see any power for these l values; due to seeing, leakage, foreshortening and other errors in the observations, we see the power of the oscillations only up to $k_h \approx 33\Delta k = 1.149\,Mm^{-1}$, or $l \sim 800$.

Note that we introduce some errors by using a lat-long grid: the value $\Delta x = 1.33673\,Mm$ is constant along meridians, but it is only correct at the equator along lines of constant latitude. As we go to higher latitudes B, this value is multiplied by a factor $\cos B$. In our resulting images in the $k_x - k_y$ plane, the resolution in k_y is given by the value above, but the resolution in the k_x is multiplied by $1/\cos B$, varying from $3.4818 \cdot 10^{-2} Mm^{-1}$ at $B = 0$ to $3.7626 \cdot 10^{-2} Mm^{-1}$ at $B = 22°.275$. This is

acceptable, since it represents a maximum error of 8%, far from our pixel resolution limitation.

As a practical consideration, our data are split into three sections corresponding to the three days of the observations, with two images per section, due to the Real and Imaginary parts of the FFT. Prior to the temporal FFT, the total time span series of data is constructed from the three sections plus empty sections corresponding to night time.

2.6 Temporal Fourier Transform

To complete the tridimensional Fourier Transform of our images, a final FFT is applied in the temporal direction, pixel by pixel in the spatial frame, over the entire temporal span of the data. Considering the starting and ending date and time of the data available (from 1506 UT, 7/3/88 to 0041 UT, 7/6/88), the total time span is 3408 minutes, with night gaps filled with zeroes. The FFT routine is much faster if the number of data points has a maximum prime factor as small as possible, preferably 2 or 3. It is thus worthwhile to adjust the time span of data to fulfill this condition. In our case, the number $3456 = 2^7 \cdot 3^3$ is the closest favorable number to the actual time span of 3408. We pad the data with 48 extra zero points to get this number, used for the temporal FFT. With this value the resolution in frequency will be: $\Delta\nu = 1/(3456\Delta t) = 4.8225\,\mu$Hz, with $\Delta t = 60s$.

The input to the temporal FFT is two images of $135 \times 135 \times 3456$ pixels, corresponding to the Real and Imaginary parts (R and I), and the output is one image of $135 \times 135 \times 3456$ pixels with alternating R and I parts in every band for the positive frequency values. One image of $135 \times 135 \times 1728$ pixels contains the final power spectrum calculated as $\sqrt{R^2 + I^2}$. Some examples of the resulting power spectra are showed in Figures 2.6 and 2.7. Figure 2.6 is a cut for $k_y = 0$, showing the ridges of the

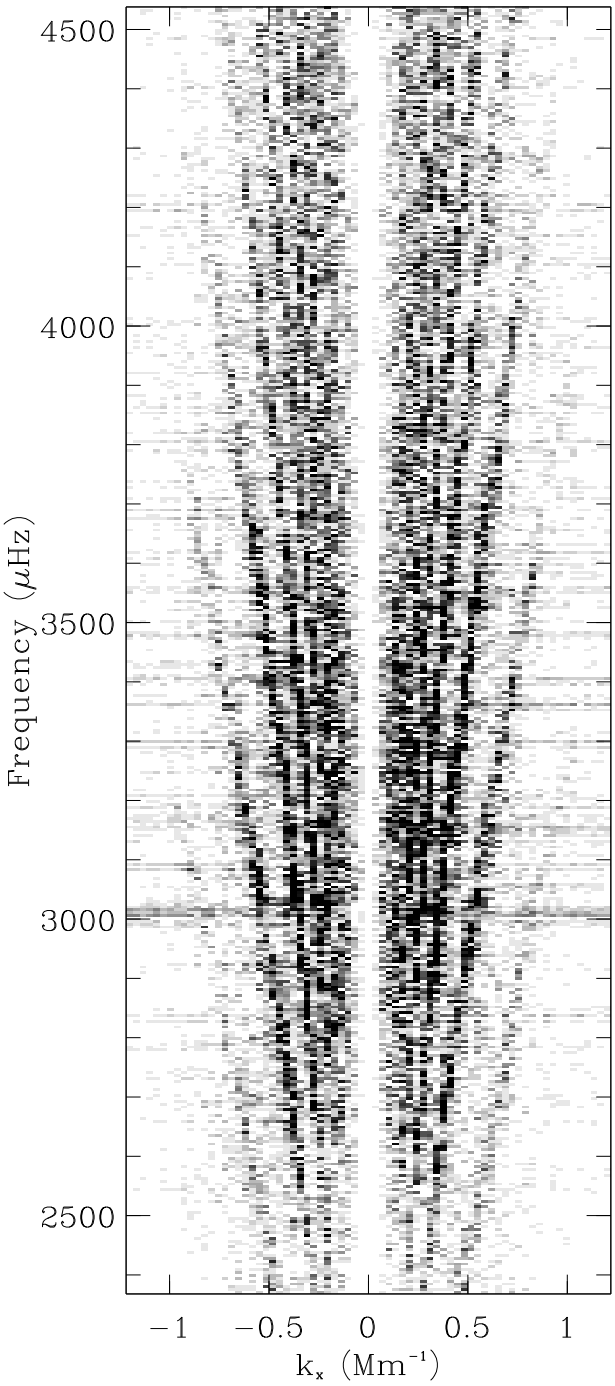

Figure 2.6: A cut of a section of the power spectrum for the central subraster at $k_y = 0$.

modes. Figure 2.7 are the resulting ring diagrams from constant frequency cuts; they

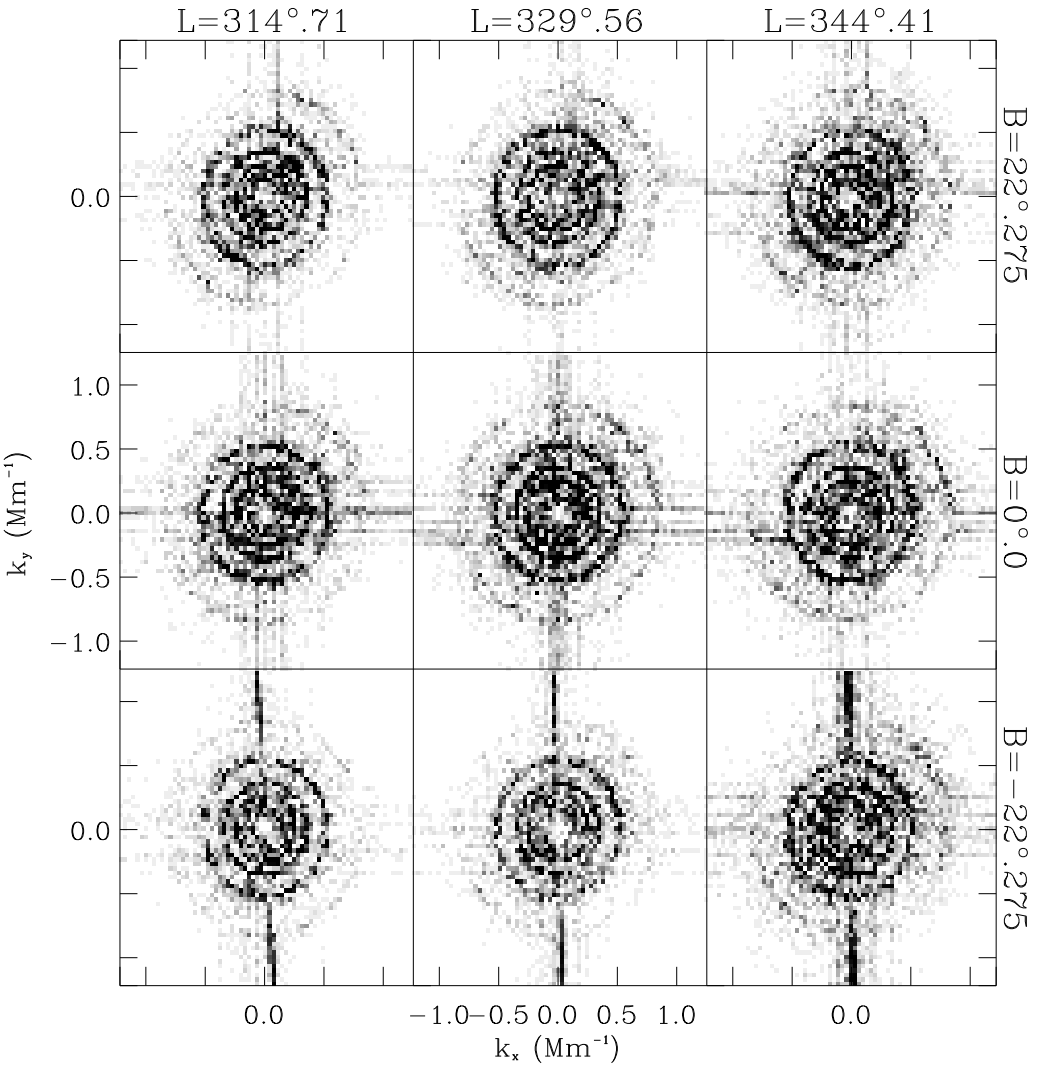

Figure 2.7: Ring diagrams for the 9 central subrasters of the solar disk. They correspond to a cut of the tridimensional power spectrum at $\nu \simeq 3000\,\mu$Hz. The labels at the right and upper sides show the position in the solar disk, with B the heliographic latitude and L the Carrington longitude.

were selected at $\nu \simeq 3000\,\mu$Hz for the 9 subrasters. The position in the solar disk is identified by the Carrington longitude L and the heliographic latitude B at the upper

and right sides of the picture. Rings for n = 1,2,3,4, and perhaps 5, can be identified in the diagrams.

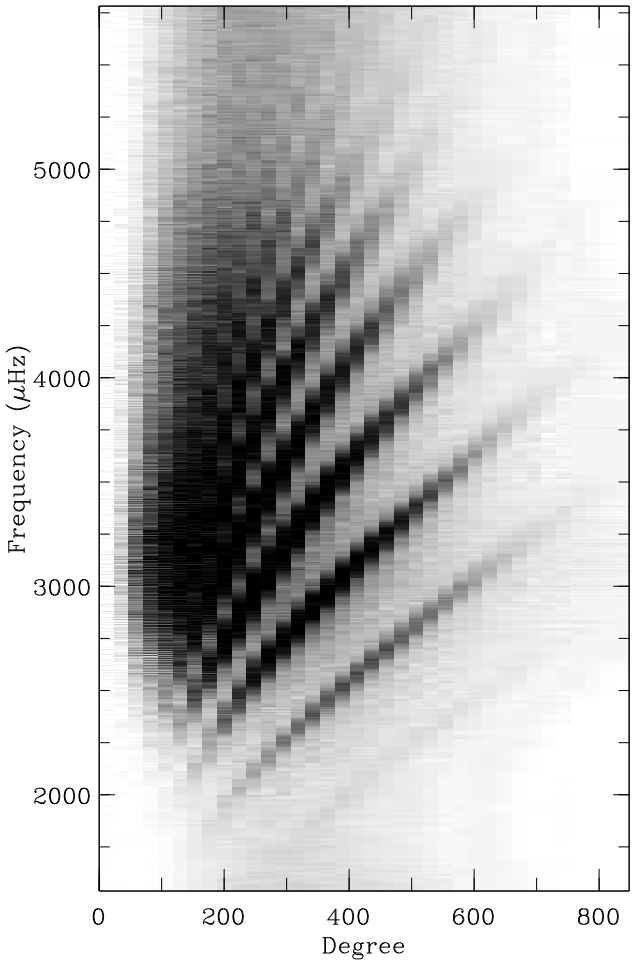

Figure 2.8: Final $l - \nu$ diagram obtained after performing an azimuthal average to the tridimensional power spectrum. The power was enhanced multiplying by k^2, as the previous plots.

Finally, Figure 2.8 shows a $l - \nu$ diagram obtained after an azimuthal average of the tridimensional power spectrum at constant k. Ridges of modes with orders $n = 0$ to $n = 8$ can be seen at higher frequencies. All of figures were obtained for the central subraster (number 13 in Figure 2.1).

The spectrum of the oscillations shows a high background at low l, with an amplitude greater than the peak of the frequencies. In these plots we have removed the background to enhance the contrast at low degree. This is done by multiplying the power spectrum by k^2. At the same time the power of the high l modes have been enhanced in the same way.

Chapter 3

Tridimensional model of the power spectra

The usual way of analyzing the power spectra of the solar oscillations is to determine the frequency of the modes for every l, m and n. This is accomplished by finding the peaks in frequency of the distribution of power resulting from the final temporal FFT in the reduction process. In our case, we focus not in the determination of the positions of the peaks, but instead how the positions are altered by the presence of horizontal velocity flows. Flows will deform the tridimensional distribution of power, and our goal is to measure this deformation.

In this three-dimensional power spectra (k_x, k_y, and ω) we can detect the presence of horizontal velocity flows beneath the solar surface. If no flows are present, the distribution of power around the origin $k_x = k_y = 0$ is axially symmetric, and the maxima of power appear as perfect circles, or rings, centered at the origin. When a velocity flow field $\mathbf{U}$ is present underneath the solar surface, the wave front is advected by it (Gough & Toomre 1983) and there is an apparent Doppler shift in the frequency of the mode

$\Delta\omega$, given by

$$\Delta\omega = \mathbf{k} \cdot \mathbf{U} = k_x U_x + k_y U_y, \tag{3.1}$$

where $\mathbf{k}$ is the vector horizontal wavenumber, and U_x and U_y are the components of $\mathbf{U}$ in an arbitrary coordinate system such as latitude and longitude. Depending on the direction and amplitude of this horizontal flow, the apparent k_x and k_y numbers will be altered, the ring will no longer be centered at $k_x = k_y = 0$ and the shape will not be circularly symmetric. Thus, if we can measure the position and shape of these rings, we can estimate U_x and U_y. In addition, once we have calculated the horizontal flows as a function of frequency, $U_x(\omega)$ and $U_y(\omega)$, we can use an inversion procedure to determine $U_x(r)$ and $U_y(r)$, where r is a certain depth in the photosphere. Finally, by performing this analysis at several heliographic positions, we can estimate the variation of the horizontal velocity field not only with depth but also with horizontal position in the Sun.

In previous approaches to the fitting of the tridimensional distribution of power (F. Hill 1988, F. Hill 1990, F. Hill *et al.* 1991b) an ellipse profile at constant frequency for the centroid of power in the rings is assumed, and a least-squares minimization is applied. But the results of preliminary tests to this approach applied to the present data, proved to be both unstable and to produce very high values for the velocities (see Patrón et al. 1992). This approach also does not adequately incorporate the statistics of the problem. A least-squares minimization procedure assumes that the underlying statistics of the data are Gaussian. However, as discussed in Duvall & Harvey (1986) and Anderson et al. (1990), this is not true in the case of the solar oscillations, which are more accurately described as randomly forced damped harmonic oscillations. Consequently, the statistical distribution of power of the solar oscillations is χ^2 with 2 degrees of freedom, and the probability density is given by Equation (3.4), in the next section. Thus a maximum-likelihood procedure is a more appropriate tool to derive the parameters of the fitting model.

3.1 Trumpets: the maximum likelihood approach

The model that has been fitted to the tridimensional power spectrum is based on a one-dimensional line profile for the peaks in the spectrum derived by Anderson *et al.* (1990). In this work, the profile of the peaks of a mode as a function of ω is modeled as a Lorentzian. In our case the profile must be a function not only of ω, but also of k_x and k_y. The dependence on k_x and k_y is given by the effective Doppler shift of the unperturbed frequency (Equation (3.1)); the resulting shifted frequency will be the position of the maximum of the Lorentzian. The model for the fit at a point of the tridimensional power spectrum given by the coordinates ν [1], k_x, and k_y is:

$$P(\nu, k_x, k_y) = \frac{A^2}{\left[\nu - \left(ck^{1/2} + \frac{U_x k_x + U_y k_y}{2\pi}\right)\right]^2 + \Gamma^2} + b_1 k^{-3} + b_2 k^{-4}. \tag{3.2}$$

The unperturbed frequency is approximated by the quantity $ck^{1/2}$, describing the dispersion relation as a power law (the constant c, another parameter in the fit, will provide information on the thermodynamics of the material below the photosphere). The term $(U_x k_x + U_y k_y)/(2\pi)$ is the Doppler shift of the frequency in μHz, with velocities in ms^{-1} and k numbers in Mm^{-1}. The amplitude and halfwidth at half maximum of the Lorentzian are given by A and Γ, respectively. The background is parameterized as a function of k only by b_1 and b_2. There is no dependence on the frequency since we assume a slow variation of the background with ν, and the fitting is made over a small enough interval in frequency that this approximation is valid. The functional form $b_1 k^{-3} + b_2 k^{-4}$ has been obtained after removing the peaks of the $k-\nu$ diagram shown in Figure 2.8, and fitting several exponential profiles to the remaining background in the k direction.

This formula represents one single peak in frequency, i.e., one single order n for

[1] From now on, frequency will be referred as ν, in μHz, with $\nu = \omega/2\pi$.

a given mode. The actual power spectrum will be the sum over all orders n of the oscillations, so that we will have a set of parameters, A_j, c_j, U_x^j, U_y^j, and Γ_j for every order j. The final model will be then:

$$P(\nu, k_x, k_y) = \sum_{j=1}^{N} \frac{A_j^2}{\left[\nu - \left(c_j k^{1/2} + \frac{U_x^j k_x + U_y^j k_y}{2\pi}\right)\right]^2 + \Gamma_j^2} + b_1 k^{-3} + b_2 k^{-4}, \tag{3.3}$$

where N is the number of modes taken into account in the fitting interval.

We define M_i to be the value of the model P in a point given by the coordinates ν , k_x , and k_y , and O_i the observed power in the data for the same point. The idea is to fit the model P to the observations. The maximum likelihood method seeks the maximum probability. The probability density for a power spectrum of solar oscillations for a single point is given by (Duvall & Harvey 1986):

$$\frac{1}{M_i} exp\left(\frac{-O_i}{M_i}\right). \tag{3.4}$$

The joint probability density, or likelihood function, L , is given by the product of the individual probabilities over the entire set of data (index i):

$$L = \prod_i \left\{ \frac{1}{M_i} exp\left(\frac{-O_i}{M_i}\right) \right\}. \tag{3.5}$$

Taking the logarithm we obtain:

$$-\, ln(L) = \sum_i \left(ln[M_i] + \frac{O_i}{M_i} \right) \equiv S. \tag{3.6}$$

Then we must search for the maximum value of L , or the minimum of the function S for the total set of parameters of the model.

In order to find the minimum of S, we used an algorithm based on the downhill simplex method (DS) for nonlinear, multidimensional functions (Press *et al.* 1986). This method is simple to apply since it only requires function evaluations. However, the initial estimations of the parameters must be very close to the values for the minimum of the function, and the method is slow. We have also tested a conjugate gradient method (CG), a minimization procedure that uses analytic derivative information, but it proved to be even more sensitive to the initial guess, and the DS method gave better results than the CG method. The CG method agrees with the minimum found in the DS method, but it is not able to find this minimum if the guess is not extremely close to it.

A last comment about this model: Equation (3.3) is the model of the power spectrum of a continuous time series. Since we have some gaps in our data, due both to bad data and night time, this continuity is broken and the effect is the product of the original series of data with some temporal window. The final result in the power distribution will be the convolution of the Fourier transform of the window function and the original power espectrum. In our work we ignore the effect of this convolution and fit directly the model in Equation (3.3). This simplifies the error estimates because the calculation requires the evaluation of derivatives of the model (see next section), and in this way it can be done analytically.

3.2 The fitting procedure

The fitting of the data can be approached in several ways. Our goal is to estimate the horizontal components of the velocity flows as a function of ν. Thus, the strategy is to choose ν, fit the model, and assign the results to this particular frequency. This last sentence must be understood very carefully. The fitting procedure will fit the model to a volume of points of the power spectrum around a given frequency, thus the velocity

obtained and associated to this frequency will be the result of the averaged effect of the velocity flows over the whole region in frequency being considered.

Figure 3.1 shows the advection effect of the horizontal flows on the distribution of power of the spectrum, constructed after plotting the position of the peaks in frequency

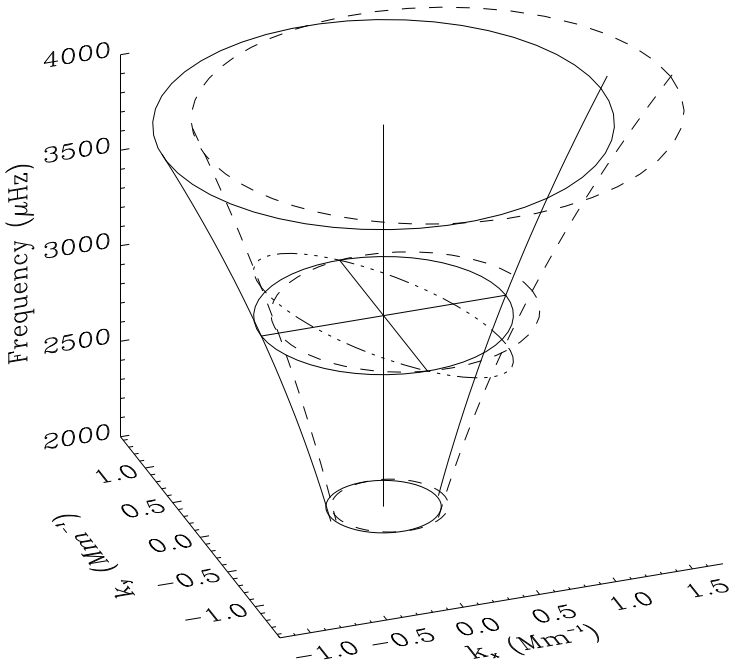

Figure 3.1: Advection effect of the horizontal velocity flows in the distribution of power. Solid lines correspond to the unperturbed state. Dashed lines represent the power distribution under an eastward flow of 2000 ms^{-1} . The dash-dot-dot-dot line represents the shifting in frequency of the solid line at 3000 μHz.

for the model in Equation (3.2). The solid lines represent the dispersion relation of the unperturbed state, with no velocity flows. The dashed lines represent the advection effect of an eastward velocity flow of 2000 ms^{-1} for all the frequencies. The dash-dot-dot-dot line shows the actual Doppler shift in frequency of the peaks. Compare this line

with the solid line at 3000 μHz, the unperturbed state. Both lines have been plotted as the frequencies corresponding to a constant k number of 0.8 Mm^{-1}. Notice how the shift in ν is different as a function of the orientation: for a $k_y = 0$ the shift is maximum, and there is no shift for $k_x = 0$.

Since we wish to fit the distribution of the power in both k and ν, we need to define a region in the $k_x - k_y - \nu$ volume in which to evaluate the function for the fit. Most generally, we should include all of the available rings ranging from the f mode ($n = 0$) to the p_7 mode ($n = 7$). In a practical point of view, the number of parameters to fit is an important factor: including all the modes raises the number of parameters to fit to $8 \times 5 + 2 = 42$ (40 parameters for the Lorentzian profiles and 2 for the background). For this many parameters, the DS method is very slow. In order to reduce the number of parameters, we reduce the number of rings considered. Fortunately, over much of the spectrum, the contribution of the wings of the Lorentzian profile to adjacent modes is very small and can be ignored. It becomes important, however, at very small k, where the rings converge, but here we stop the fitting because of the high levels of noise and background. After testing the fitting procedure taking different numbers of rings in consideration, we decided that the inclusion of two rings was the best compromise between speed and accuracy. In this case, the number of fitted parameters is $5 \times 2 + 2 = 12$.

Once we have chosen the two adjacent modes to fit, a given ν determines the limiting region for the fit in k. We must not include other rings in the region since they are not taken into account in the fit. At the same time we need to include as much of the Lorentzians (in the frequency direction) of the two chosen rings as we can. In order to decide where these limits are, we need to estimate the position of the ridges of the modes. We thus first compute a radial average in k of the tridimensional power spectrum, resulting in a $k - \nu$ diagram displaying the ridges in Figure 2.8. The resulting average approximates the unperturbed state, or the dispersion relation. The position of the ridges are then measured from the computer screen, and stored as a

data base for the first guess of the position of the peaks of the Lorentzian profiles. This method only works when the rings are not too far from a symmetric distribution around the axis $k_x = k_y = 0$, and thus is valid only when the velocity flows are less than several hundred ms^{-1}. Flows of the order of 1000 ms^{-1} make the distribution of power very asymmetric, and the estimate must be obtained by other methods. A plot of the estimated position of the ridges is showed in Figure 3.2. The stair steps in the

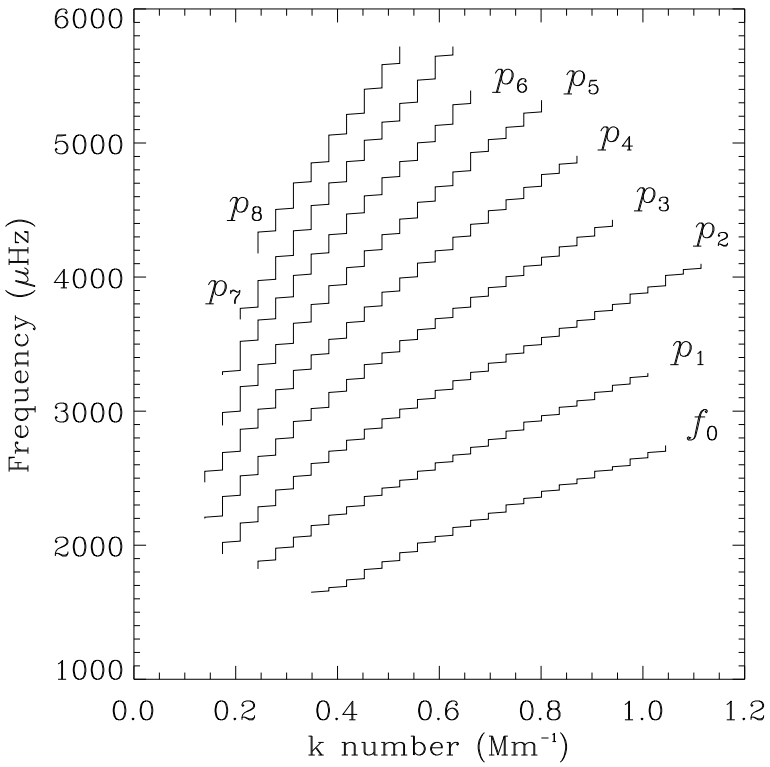

Figure 3.2: Estimated positions of the ridges in a $k-\nu$ diagram obtained by averaging the 3-dimensional power spectrum around constant k. This figure shows the full range available in ν and k.

plot are a consequence of the poor resolution in k in comparison with the resolution in ν: in the plot there are only 35 points in k for about 1000 in ν. Figure 3.3 shows the plot with full resolution in both axes for a small region around 3000 μHz in ν and k = 0.5 Mm^{-1}.

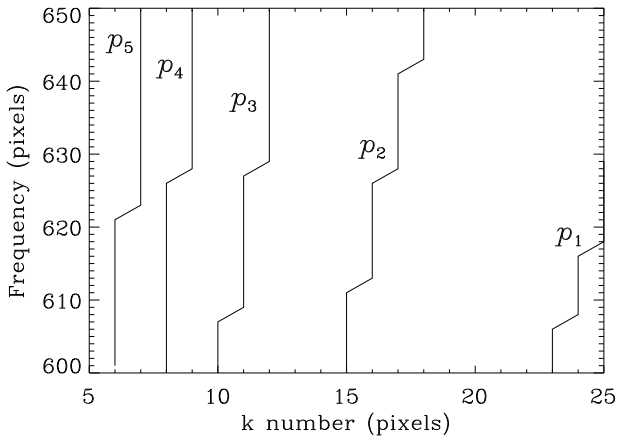

Figure 3.3: A full-resolution plot of the region around $\nu = 3000$ μHz and $k = 0.5$ Mm^{-1}, showing some of the ridges of the previous figure.

Using these estimates, we choose the limits in k. As an example, assume we want to fit the p_2 and p_3 rings. The profile of the ridges extends in the k direction as much as one or two pixels from the maximum. Figure 3.3 shows that, on the low-k side of ridge p_3, two pixels will include contributions from p_4. In this case we choose one pixel to lower k and 2 pixels to higher k, where the ridge of p_2 is further from the peak of mode p_1. These numbers differ depending on the region where we are working, being small at low k and larger at higher k. They also depend on ν.

The problem is then how many pixels around the chosen ν to include. To determine the range in ν, we performed the fitting for several frequencies, varying the frequency range in pixels around the chosen ν from 5, 7, 9,..., up to 31. The results are shown in Figures 3.4 and 3.5. In Figure 3.4 we show the results for the longitudinal component of the velocity for p_2 as a function of ν for 6 ranges of ν included in the fitting (7, 11, 15,..., to 27 points in ν). In Figure 3.5 we plot the results for both latitudinal and longitudinal velocities for p_2 and p_3 as a function of the frequency range and for the result of the average of 10 different frequencies; the vertical bars show the r.m.s. of the averaging process.

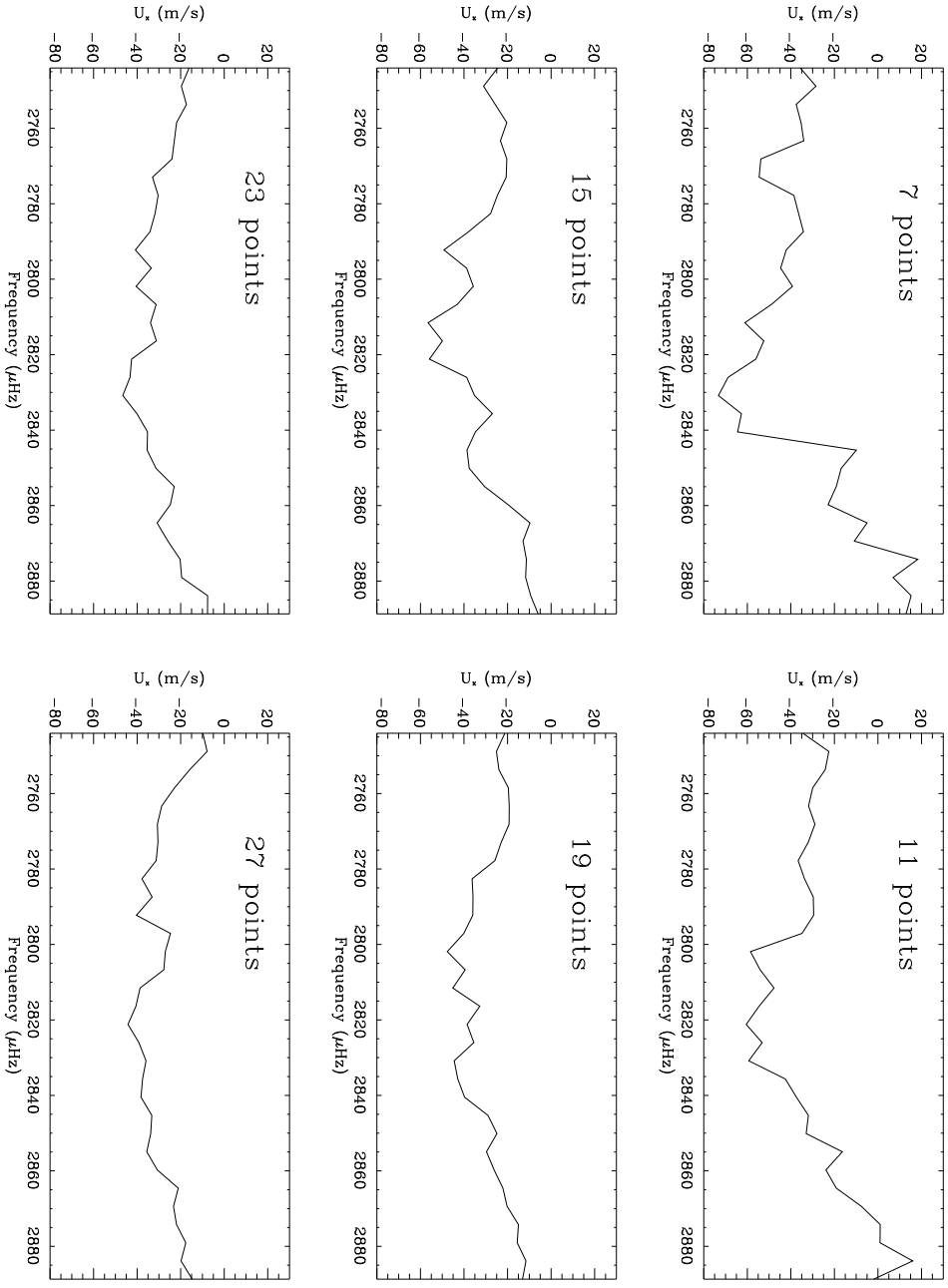

Figure 3.4: Results of the fitting for the longitudinal velocity U_x for the p_2 ring as a function of ν . Each plot is made for a different width in ν in the region considered in the fitting. For example, for 11 points and a given frequency, the fitting region includes the central frequency and 5 pixels above and below it for a total of 11 levels.

Figure 3.4 shows that, when a small number of levels in the frequency range are included, the results vary rapidly from frequency point to frequency point. As more levels are included, the inferred velocity is smoothed as a function of ν since we are averaging over more and more levels in frequency, and thus a greater range in depth. Since we wish to both minimize the noise in the inferred velocities, and maximize the depth resolution on corresponding ν resolution, a range between 11 and 21 frequency levels was chosen for the fitting.

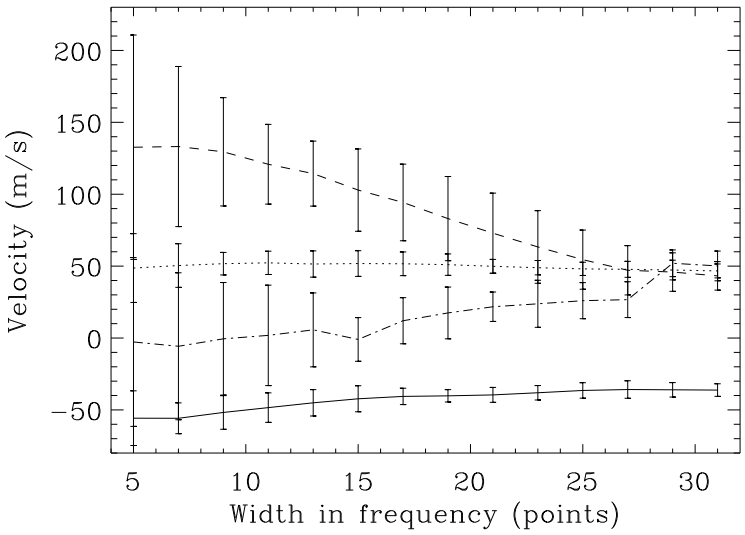

Figure 3.5: Results of fitting U_x and U_y for two rings, p_2 and p_3, as a function of the number of levels included in the frequency range. Results are displayed for the average of 10 independent frequency points to show the general behavior of the fit. U_x velocities are: solid, for p_2, and dashed, for p_3 ; U_y velocities are: dotted, for p_2, and dash dot, for p_3.

Figure 3.5 shows the smoothing and averaging effect of increasing the ν-range: the velocities tend to constant values that are not too high. By including many levels in frequency we are averaging over the distribution of velocities in depth, which tends to alternate between negative and positive values as a function of ν, and gives lower values for the averaged velocity (notice how the r.m.s. bars are shorter for larger widths in

frequency). It is not obvious what to choose as a lower limit to the number of ν levels, but 17 levels appears to be an acceptable upper limit. Thus, we narrowed the range to between 11 and 17. Since 11 levels reduces the number of points to fit, and fewer levels increases the resolution in frequency and in depth, we finally chose 11 levels for the fitting.

We can then search for the minimum of S, where the sum in Equation (3.6) is over the selected region for 2 rings and one ν. (This region, limited by a range in ν and k, has the shape of a cylindrical annulus centered at $k = 0$). Depending on the rings and ν, the number of points included in the region varies, ranging about 2000 to 20000 points due to the quasi-parabolic behavior of the dispersion relation. This affects the error estimation, which is lower for a larger number of points in the region.

The computational aspect of the fitting is considerable. Since the starting estimate of the parameters has to be very close to the values for the minimum, care must be taken for the guess of the first fitting. Subsequently, the resulting output values for the parameters are used as inputs for the next point in ν, and so on. Problems arise at low k and at both low and high ν, where the noise increases. In these regions, the fitted parameters, U_x, U_y and Γ, can either become enormous or go to zero. When this happens the process must be restarted, with new initial guesses.

As a recipe, an initial guess is made for every pair of modes (0-1, 1-2, 2-3,...) and for a frequency located approximately in the center of the interval in ν including both rings. We then vary the fitting region both up and down in ν. Ideally, two runs of the program should be enough. But, due to the problem discussed above, the program must be run 6 or 8 times, each including a different number of points in k and new initial guesses. Most of the work was performed on a SUN Sparc-10/41 workstation, where the total elapsed time was about 2813 hours of clock running time of the programs for the fitting of the rings of 8 subrasters. In addition, we used the CRAY supercomputer at Jet Propulsion Laboratory in Pasadena, California for two of the subrasters for a total

of 105 hours of clock running time. With this computer we increased the speed of the process by a factor of 10 to 30.

3.2.1 Error estimations

The determination of errors is always a very difficult task. In every process of scientific data analysis there are two aspects to consider: the propagation of measurement and reduction errors, and the error introduced by the fitting procedure.

In our case, the first source of errors originates in the signal-to-noise ratio of the raw data, introduced during the detection. This error will propagate all the way through the data reduction: calibration to obtain the velocity values, with errors introduced by the ephemeris values of the relative velocity between sun and observing-site; two interpolation processes during the geometrical transformations; the running mean for the temporal filtering, and, finally, the Fourier transforms in three dimensions. All this leads to a power spectrum of data with a certain error in it, due only to the reduction process.

Next we fit a model to the data. At this point, the physics of the problem must be considered. Besides the detection and reduction errors, the determination of the frequencies and the parameters describing the distribution of power of the oscillations has two basic sources of errors: the background sources of power and the stochastic nature of the modes. It is not clear whether the uncertainties are limited by one source or the other. While it is widely thought that the stochastic nature of the modes is the limiting process, with current observations this is not completely clear (Duvall & Harvey 1986). In any case, for our purposes, we limit our considerations to the second source of errors, because we introduce explicitly the background source of power in our fit.

An estimate of the uncertainties of the fitted parameters can be easily calculated in

the case of a normal multiple regression for the fit. If the likelihood function is equivalent to a probability density function for the parameters, then the same calculation can be used. This is so if the likelihood function is approximately Gaussian for variations of the fitting parameters. Duvall & Harvey (1986) have found, in their simulations of the power spectrum of the oscillations, that if the likelihood function is expressed in terms of the logarithms of the parameters, then the distribution is approximately Gaussian. Using the assumption that our model is equivalent to a normal multiple regression, the estimate of the uncertainties can be obtained from the inverse of the Hessian matrix (α) of the function S, with elements given by:

$$\alpha_{k,l} \equiv \frac{\delta^2 S}{\delta a_k \delta a_l}, \tag{3.7}$$

where a_k and a_l are the fitting parameters, and $(1 \leq k, l \leq \rho)$, with ρ the number of parameters in the fit.

The final error estimation should include both detection and reduction errors plus the fitting procedure errors. But the propagation of the errors from the reduction process into the fitting procedure is difficult. On the other hand, the uncertainties given by the fitting procedure itself are a good estimate of the total errors. For these reasons we used the final errors for the fitted parameters to be the ones introduced by the fitting procedure, and they have been calculated using Equation (3.7).

3.3 Results

Figures 3.6 and 3.7 show the results obtained from fitting the $n = 2$ ring determined in the central subraster of the solar disk for the two components of the horizontal velocity flows as a function of ν. The magnitude of the velocity rises rapidly to higher absolute values at low ν. This is not unexpected, since the low frequency regions are at low k, where the background signal and noise are high, and the rings converge. At

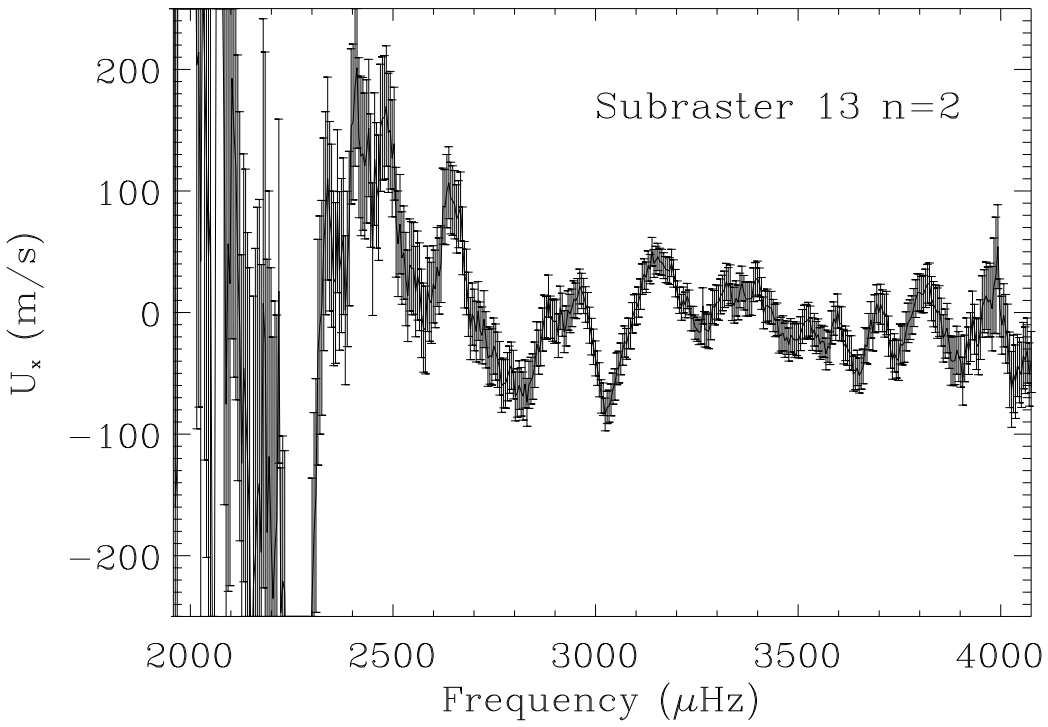

Figure 3.6: Fitted longitudinal velocity U_x as a function of ν for the $n = 2$ ring determined in the central subraster of the solar disk. Notice how the error bars are larger as we go closer to the lower and upper limits in ν.

higher ν, the inferred values of the velocity appear to be both stable and not very high, around a region of a few tens of ms^{-1}, below and above zero.

The results of the fitting of the latitudinal velocity, U_y, at subraster 13, are shown in Figure 3.8 for all the modes in consideration, p_0 to p_7. Figure 3.9 shows the results for the longitudinal velocity, U_x, for mode p_4 at the 9 subrasters. The error bars are not showed here, but they are of the same magnitude as shown in Figures 3.6 and 3.7.

In order to test the fitting procedure, we have fitted a simulation of the distribution of power from the model given by Equation (3.3), using the inferred parameters and

adding a random error in the artificial data as follows (Anderson et al. 1990):

$$M_i^{sim} = -M_i\, ln(r_i), \tag{3.8}$$

where M_i^{sim} is the simulated data, M_i is the model, and r_i a random number in the interval [0,1], for a single point (i) in the power espectra. Comparisons between the results obtained from the real data and those obtained from the models are shown in Figures 3.11, 3.12, 3.13 and 3.14. These are the results for subraster 13 at disk center for modes p_2 and p_3 (in these plots we do not show the entire range in frequency to avoid the noisy results at low frequencies, as shown in Figures 3.6 and 3.7). The general

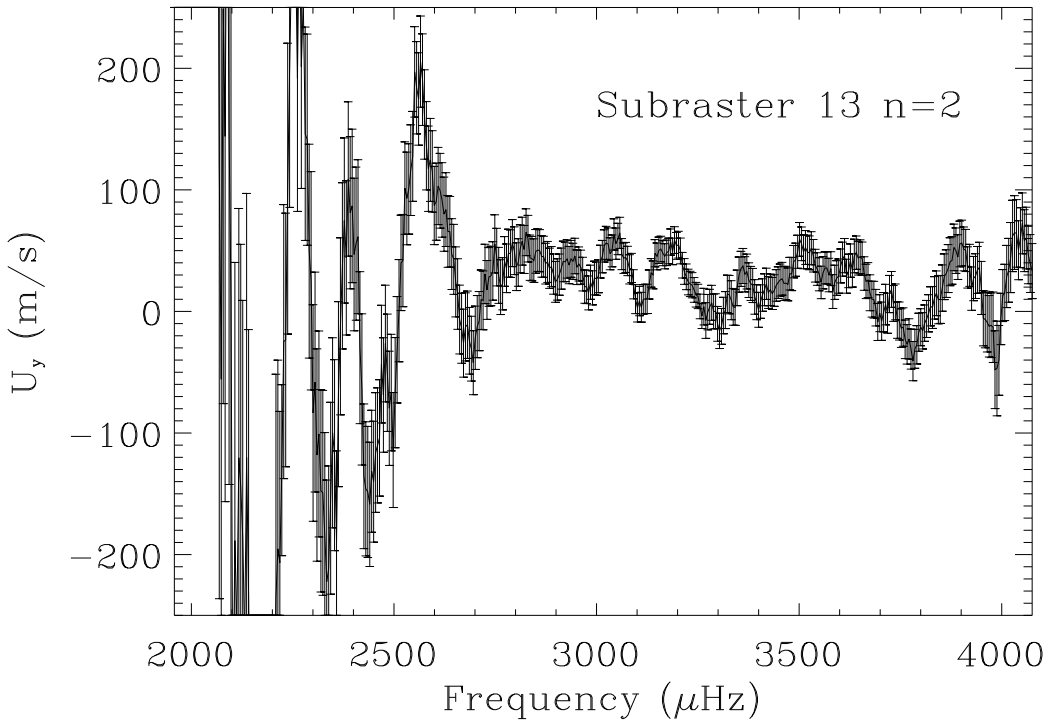

Figure 3.7: Fitted latitudinal velocity U_y as a function of ν for the $n = 2$ ring determined in the central subraster of the solar disk.

behavior of the fitted parameters is basically similar, but there can be large differences

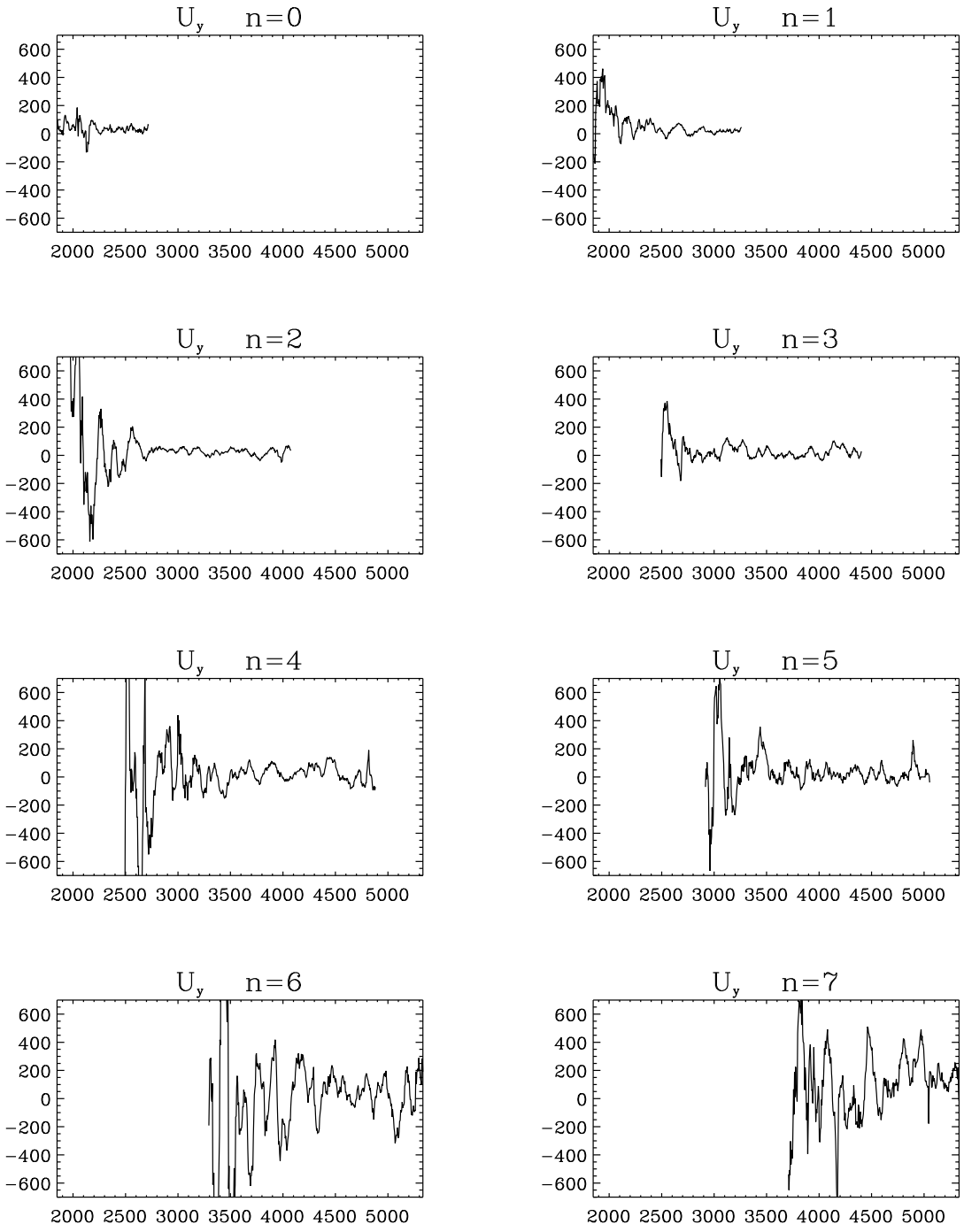

Figure 3.8: Latitudinal velocity (U_y) as a function of ν, obtained in the fit of subraster 13 for modes p_0 to p_7 . Units in vertical axis are ms^{-1} , and μHz in the horizontal axis.

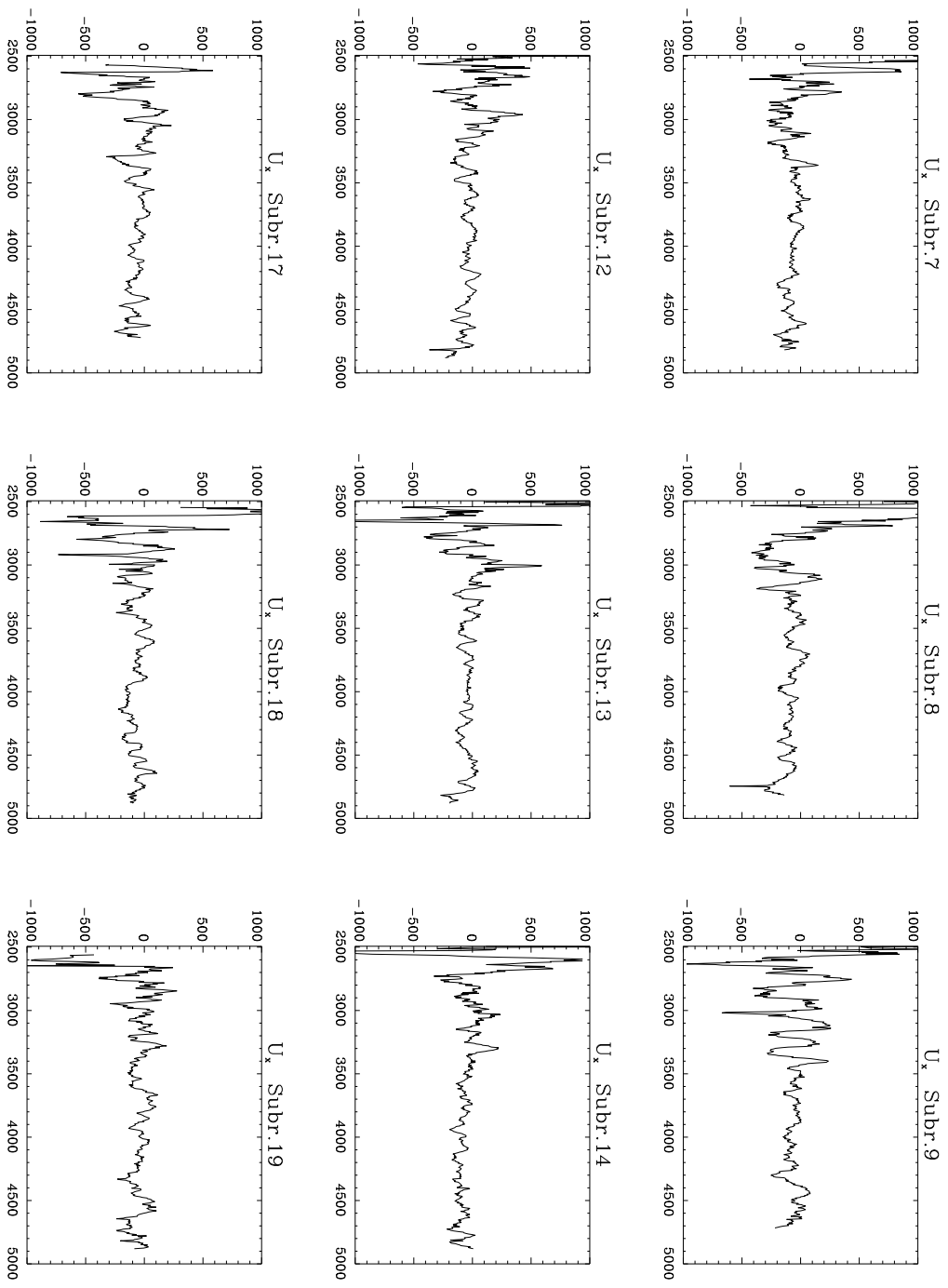

Figure 3.9: Longitudinal velocity (U_x) as a function of ν, obtained for mode p_4 in the fit of the 9 subrasters. Units in vertical axis are ms^{-1} , and μHz in the horizontal axis.

at individual frequency points. We conclude that the rapid variations of the values of the inferred parameters with frequency is a result of the fitting procedure. The procedure is sensitive to the chosen range in k due to the poor resolution available, and as ν varies, the width of the range in k changes due to the dispersion relation.

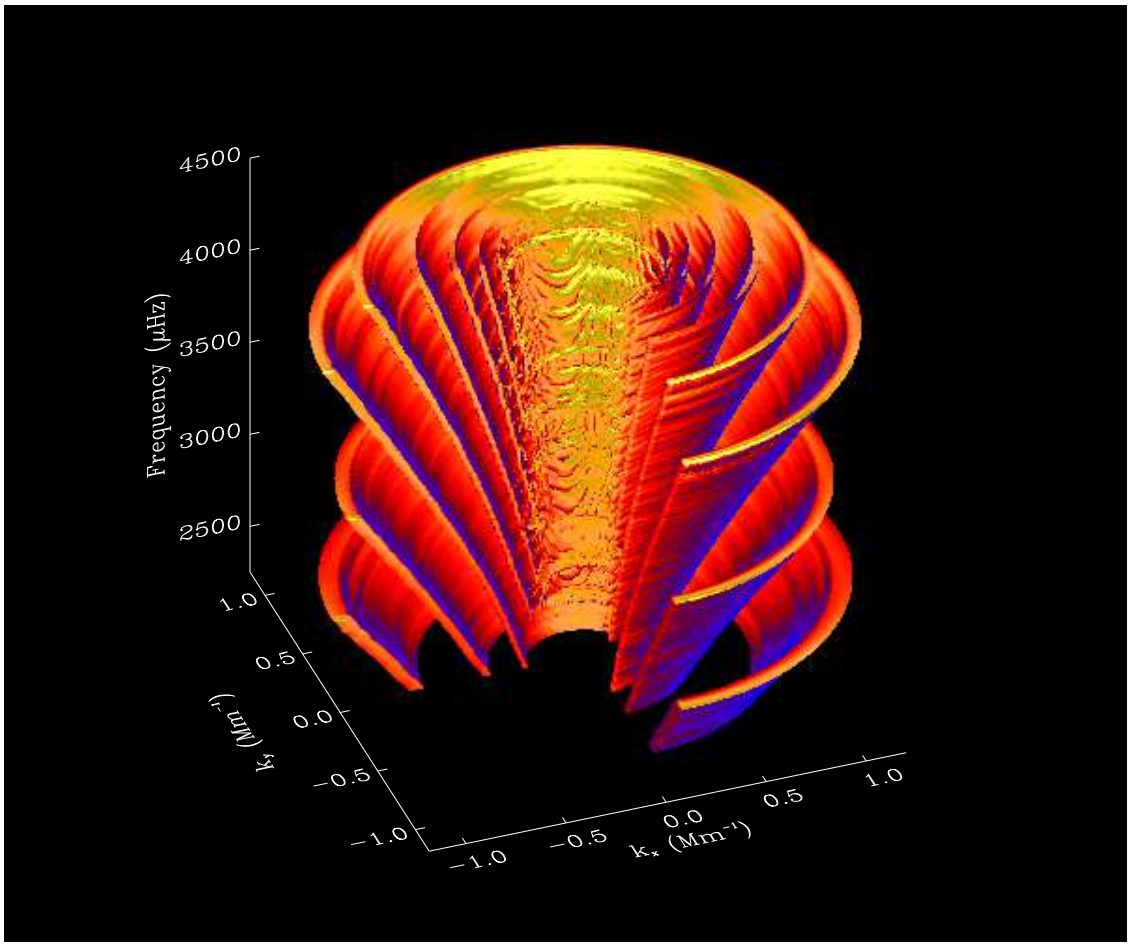

Figure 3.10: View of the model of the tridimensional power spectrum of the oscillations after the fitted parameters. To improve the contrast between different orders n the background has been removed and the amplitude and width of the Lorentzians are the same for all the modes.

Figure 3.10 shows a tridimensional view of the 'trumpets' for the 8 rings $n = 0, \ldots, 7$. It has been produced by using the model in Equation (3.3) but changing the

widths and the amplitudes of the Lorentzians to get a good contrast between different trumpets.

The biggest discrepancies between the real data and the model results are in the amplitude of both the background and the Lorentzian peaks. The model used for the background is an empirical power law. As a consequence, both the amplitude and the width of the fitted peaks are probably not very accurate, and the fitted values of A , Γ , b_1, and b_2 are closely correlated (Figures 3.13 and 3.14). However, this should not affect our estimate of the position of the peaks, that is the main quantity we are interested on, since it is this term what includes the effect of the horizontal velocity field. We find that the estimated parameters c, U_x, and U_y, reproduce the position of the peaks and agree well with the real data.

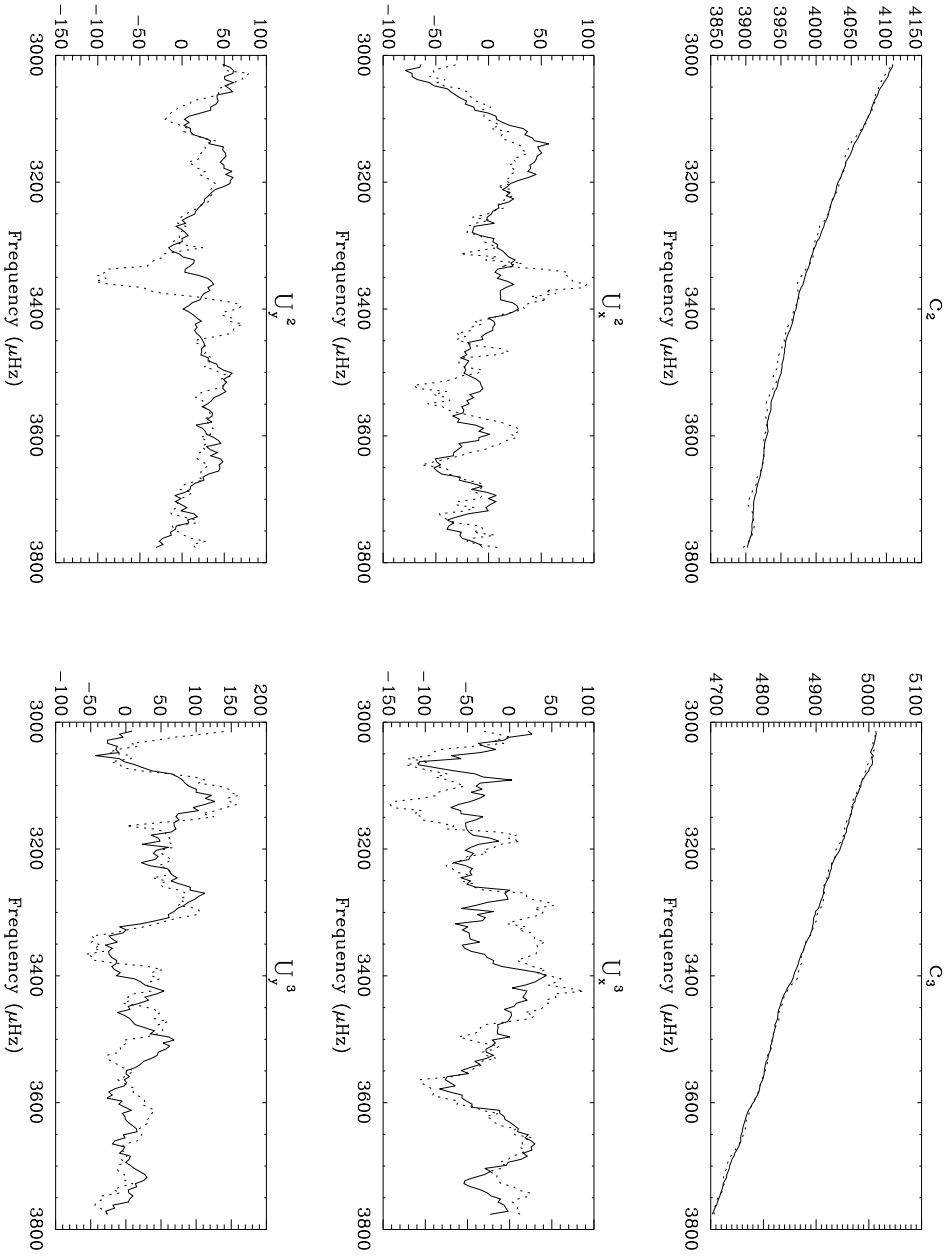

Figure 3.11: Fitted parameters, c, U_x, and U_y, as a function of ν for modes p_2 and p_3 at disk center, subraster 13. Solid lines correspond to the fit of the real data. Dotted lines correspond to the artificial model. The superscript in the velocity labels denote the order of the modes.

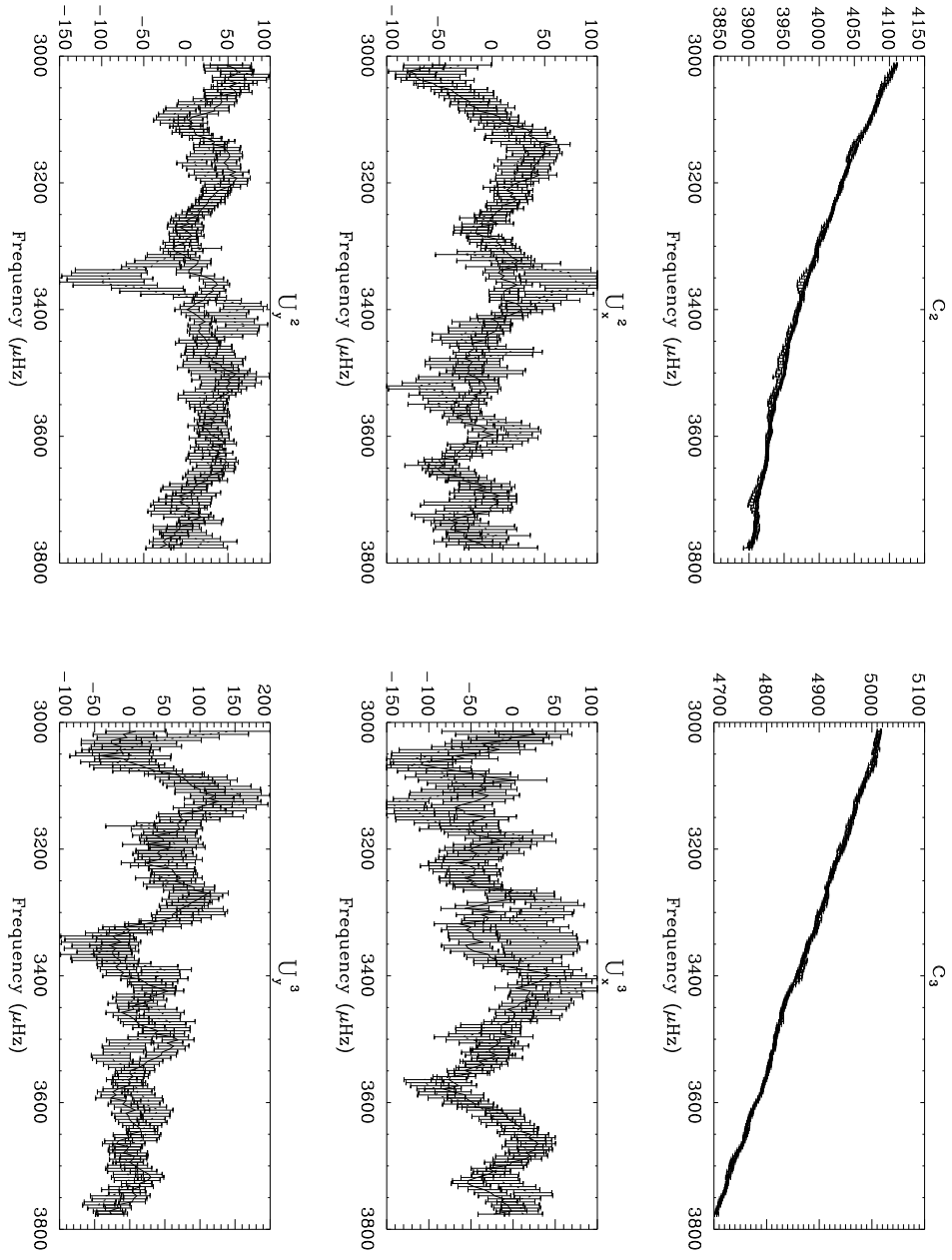

Figure 3.12: The same plot as previous figure but showing the error bars.

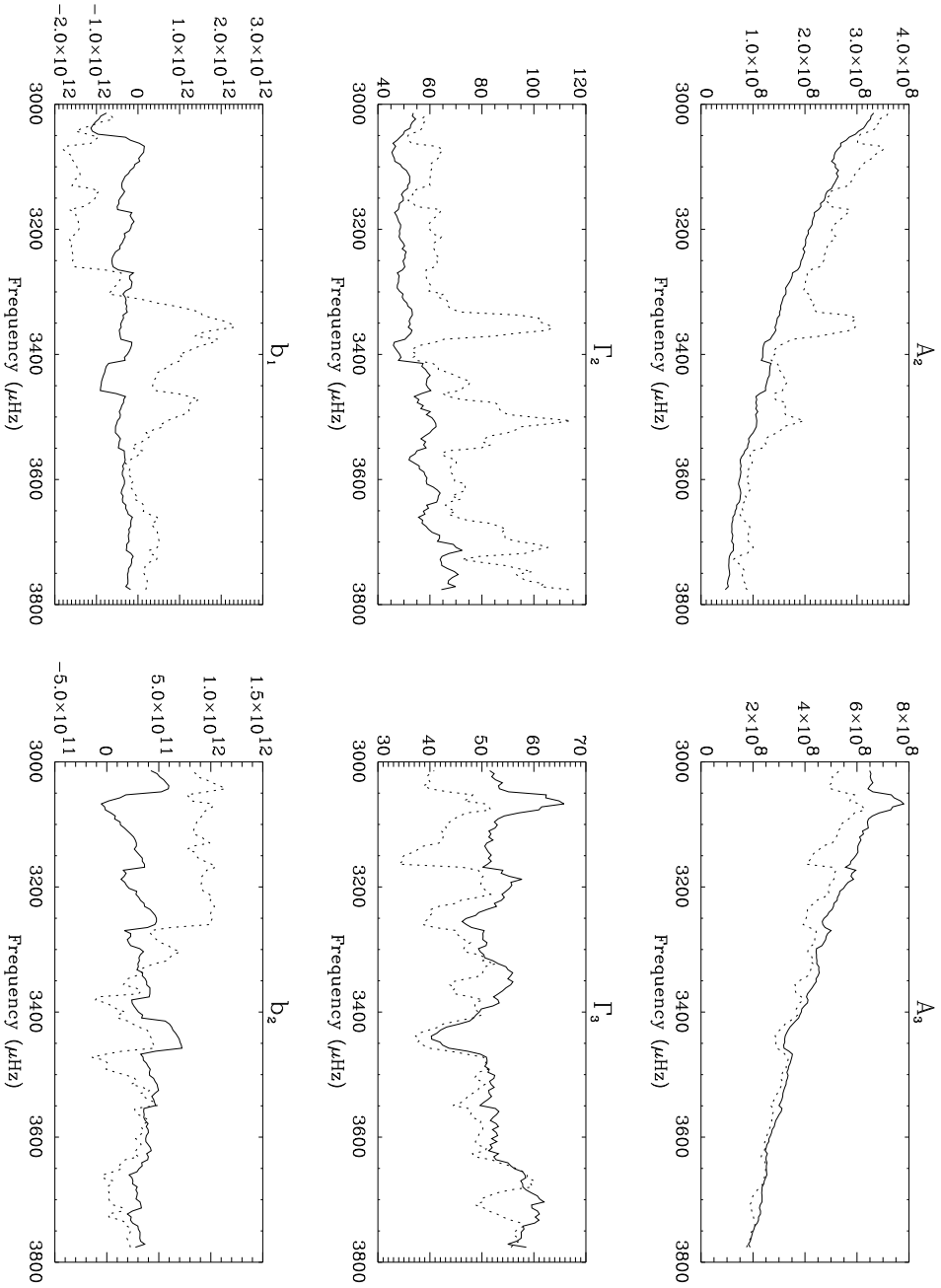

Figure 3.13: Fitted parameters, A, Γ, b_1 and b_2, as a function of ν for modes p_2 and p_3 at disk center, subraster 13. Solid lines correspond to the fit of the real data. Dotted lines correspond to the artificial model.

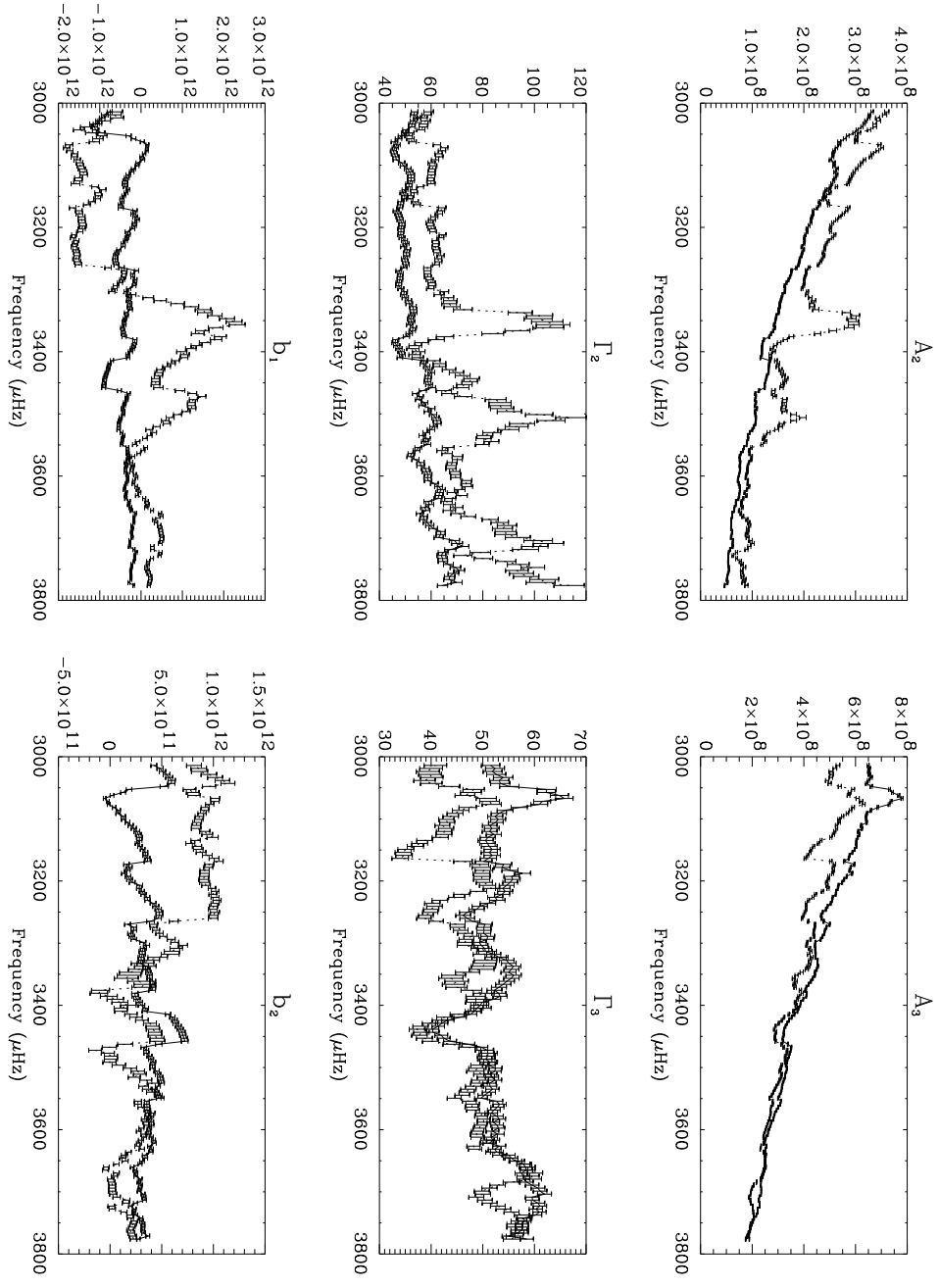

Figure 3.14: The same plot as previous figure but showing the error bars.

Chapter 4

Depth dependence of the velocity flows

The most interesting aspect of helioseismology is the ability to infer conditions in the solar interior. The basic information we obtain as the first result of the reduction of oscillation data is the frequencies of the modes and the dependence of certain derived quantities with these frequencies. To then determine the depth dependence of physical solar quantities is not a trivial task. Inferring a spatial distribution of these quantities will give an image of the structure of the sun. The theory of solar oscillations tells us that, in the so-called forward problem, the observable parameters of the modes are a result of the depth dependence of both the internal solar conditions and the eigenfunctions of the modes (see one of the several helioseismology reviews, like Unno *et al.* 1989, Brown *et al.* 1986, etc.). In the forward problem the observed oscillation parameters are calculated once we know the depth dependence of the physical quantities.

The observational results obtained in solar helioseismology depend on frequency, and the depth dependence of the physical quantities is the unknown of the problem. This directly confronts us with an inverse problem. Eventually, any analysis of oscillation

data must deal with an inversion problem. This will be the next and final step in our analysis.

In this chapter we give a description of general inversion techniques, their application to helioseismology and, in particular, to the data of this work, showing the final results as the distribution with depth of the horizontal velocity field.

4.1 Inversions

In the case of solar oscillations the forward problem can be described like this: the measured frequencies of the modes, and every observable related to them, are dependent on weighted averages of the properties of the Sun. The weights, or kernels, are functions, specific for every mode, that describe the sensitivity of the mode to these physical properties. Kernels are specific integrals of mode eigenfuntions weighted by solar model quantities (like density). An illustrative example of the forward (and inversion) problem is the rotational splitting of the frequencies of the modes. In a spherically symmetric non-rotating star, the frequencies of the modes are a function of n and l but not of m, the azimuthal order. The solar rotation breaks the degeneracy of ω and a peak appears in frequency for every m, instead of a single peak for a given l and n pair (Gough 1981). If $\omega_{l,n,0}$ is the frequency for l, n and $m = 0$ (a zonal mode), the split frequencies $\omega_{l,n,m}$ are given by:

$$\omega_{l,n,m} = \omega_{l,n,0} + m\,\omega^s_{l,n}, \tag{4.1}$$

where $\omega^s_{l,n} = (\omega_{l,n,m} - \omega_{l,n,0})/m$ is a measurement of the splitting, and can be expressed as:

$$\omega^s_{l,n} = \int_0^R K_{l,n}(r)\Omega(r)dr, \tag{4.2}$$

where $\Omega(r)$ and $K_{l,n}(r)$ are the solar rotation rate and a weighting function or kernel, respectively, with R the solar radius.

Equation (4.2) is a representation of the forward problem: an observable quantity, $\omega^s_{l,n}$, dependent on frequency (represented by the numbers l and n), is the weighted average of a property of the sun in depth, the solar rotation $\Omega(r)$. The theory of solar oscillations provides us with the functions $K_{l,n}(r)$, or kernels, and by knowing the solar rotation rate we can predict the rotational splittings $\omega^s_{l,n}$. In practice, we do not know $\Omega(r)$, but we can estimate $\omega^s_{l,n}$. Then, the problem is to determine $\Omega(r)$ in the integral, the so-called inverse problem.

4.1.1 Fundamental ideas and methods

Several inversion techniques have been applied to geophysical (R. Parker 1977) and helioseismic data (Gough 1985; Christensen-Dalsgaard *et al.* 1990). Here we discuss some basic aspects that are common to every method. First, rewrite Equation (4.2) in a more general form:

$$V_i = \int_0^R K_i(r)\mathcal{V}(r)dr, \quad i \in \mathcal{D}\,. \tag{4.3}$$

This is the form of a Fredholm Equation of the first kind, a general definition of the inversion problem. Here, a set of integral equations, with some weighting functions $K_i(r)$, relates the unknown function $\mathcal{V}(r)$ to a set of observables V_i, where the index i runs for all the available data points in $\mathcal{D}$.

We introduce the concept of averaging kernels, or resolution kernels. The averaging kernels are functions defined for a given value r_0 as a linear combination of the kernels

$K_i(r)$, with coefficients $c_i(r_0)$:

$$\mathcal{K}(r;r_0) \equiv \sum_{i\in\mathcal{D}} c_i(r_0)K_i(r). \tag{4.4}$$

This definition is such that $\mathcal{K}(r;r_0)$ is small everywhere except around $r = r_0$ and also its modulus is unity:

$$\int_0^R \mathcal{K}(r;r_0)dr = 1.$$

In this case, a function $\bar{\mathcal{V}}(r)$ can be defined for r_0 such that:

$$\bar{\mathcal{V}}(r_0) \equiv \sum_{i\in\mathcal{D}} c_i(r_0)V_i = \int_0^R \mathcal{K}(r;r_0)\mathcal{V}(r)dr. \tag{4.5}$$

This defines the averaging kernel: $\bar{\mathcal{V}}(r_0)$ is a weighted average of the real function $\mathcal{V}(r)$ around the value r_0, with weights $\mathcal{K}(r;r_0)$. The shape of the averaging kernels determines how well the functions $\bar{\mathcal{V}}(r_0)$ are localized around position r_0. If $\mathcal{K}(r;r_0)$ closely resembles a Kronecker delta function $\delta(r-r_0)$, then $\bar{\mathcal{V}}(r_0)$ provides an average of $\mathcal{V}(r)$ over a small range in r. Equation (4.5) also shows that $\bar{\mathcal{V}}(r)$ is a linear combination of the data V_i.

Closely related to the averaging kernels is the concept of a trade-off between resolution and error magnification. If the averaging kernels were precisely δ-functions, and the data V_i were error-free, we could exactly identify $\bar{\mathcal{V}}(r_0)$ with $\mathcal{V}(r_0)$. But in fact, the magnification of errors in the data in this situation dominates the estimate $\bar{\mathcal{V}}(r_0)$. There is a trade-off between the resolution of the averaging kernels and the error magnification in the results that is controlled by an adjustable parameter (or parameters) in the inversion method. Depending on our goal and our estimate of the errors in the input data, this parameter is adjusted.

Inversion methods

A description of different inversion techniques is given in Gough (1985) and Christensen-Dalsgaard *et al.* (1990). Here we summarize them and in the next section describe in detail the method used in this work.

The goal is to find the linear combination in Equation (4.5) that results in the best estimate $\bar{\mathcal{V}}(r_0)$ of the real function $\mathcal{V}(r_0)$. All methods comprise both a minimization procedure and a constraint. The details of these 2 components is what distinguishes the methods, which take into account the trade-off between resolution and error magnification. Four methods have been used for helioseismic inversion purposes: optimally localized averages, least-squares with second derivative smoothing, spectral expansion and asymptotics.

The method of optimally localized averages was developed by Backus & Gilbert (1968). In it, a trade-off parameter determines the importance of two terms in the minimization: a function that measures the resolution kernel width, and the error magnification.

In the least-squares method, the error magnification is expressed as a smoothness of the estimated function, while the resolution is represented by the best fit to the data. It will be explained in detail in the next section.

A good description of the spectral expansion method can be found in Gough (1985). It is related to a least-squares method, but with no smoothness constraint, and it is based on an expansion of $\bar{\mathcal{V}}$ in terms of the averaging kernels. The constraints lie in the rejection of certain kernels that can produce singularities in the calculation.

Asymptotic inversions are applicable only to high-order p modes, so it is specific for solar oscillations and has been developed for the rotational splitting of the frequencies. It exploits asymptotic approximations in the oscillation theory to infer the rotation rate

$\Omega(r)$. The result is the expression of $\Omega(r)$ as a function of the rotational splittings, leading to an equation like Equation (4.5).

4.1.2 Least squares with second-derivative smoothing

A least-squares piecewise constant fit, subject to minimization of the second derivative of the velocity distribution, has been applied to the fit parameters discussed in the last chapter. In this method we discretize the estimation function $\bar{\mathcal{V}}$ as a piecewise constant approximation, or a dissection of the solar radius

$$0 = r_0 < r_1 < \ldots < r_N = R;$$

so that the estimation defined as

$$\bar{\mathcal{V}}(r) \equiv \sum_{j=1}^{N} \bar{\mathcal{V}}_j \phi_j(r), \tag{4.6}$$

is a histogram-like function, with $\bar{\mathcal{V}}_j$ a set of coefficients, and the $\phi_j(r)$ functions defined by:

$$\phi_j(r) \equiv \begin{cases} 1 & r_{j-1} < r < r_j \\ 0 & \text{elsewhere} \end{cases} \qquad (j = 1, \ldots, N). \tag{4.7}$$

The method seeks the best fit to the data V_i. It assumes that the errors in the data are independent, with standard deviations σ_i. Using Equation (4.3) this is performed by minimizing the χ^2 of the fit in a least-squares sense:

$$\chi^2 = \sum_{i \in \mathcal{D}} \sigma_i^{-2} \left(V_i - \int_0^R K_i(r) \bar{\mathcal{V}}(r) dr \right)^2. \tag{4.8}$$

To make the equations more compact, define the matrix $\mathbf{B}$:

$$\mathbf{B}_{ij} \equiv \sigma^{-1} \int_0^R K_i(r)\phi_j(r)dr.$$

Taking the derivative of Equation (4.8) with respect to each $\bar{\mathcal{V}}_j$ and equating it to zero and using Equation (4.6) we get:

$$\sum_{i\in\mathcal{D}} \left(\sum_{k=1}^{N} \mathbf{B}_{ik}\bar{\mathcal{V}}_k - V_i/\sigma_i \right) \mathbf{B}_{ij} = 0\,, \tag{4.9}$$

or:

$$\sum_{k=1}^{N} (\mathbf{B}^T\mathbf{B})_{jk}\bar{\mathcal{V}}_k = \sum_{i\in\mathcal{D}} (\mathbf{B}^T)_{ji}(V_i/\sigma_i) \qquad j = 1,\ldots,N\,, \tag{4.10}$$

where T denotes the matrix transpose.

This is a system of linear equations. In order to find the solution, the inverse of the square matrix $(\mathbf{B}^T\mathbf{B})$ must exist; but, in most of the practical cases involving a large number of equations, this problem is ill-conditioned. Here we introduce a smoothness constraint. If we constrain the function $\bar{\mathcal{V}}(r)$ to be smooth, then the problem can be rendered numerically stable, and hence solvable. The smoothing is performed by adding to the function that must be minimized in Equation (4.8) a term proportional to the second derivative of $\bar{\mathcal{V}}(r)$. We use a discrete approximation to this derivative, and the final function is:

$$F(\bar{\mathcal{V}}) = \frac{1}{2}R^3 \sum_{j=2}^{N-1} (\bar{r}_{j+1} - \bar{r}_{j-1}) \left(\frac{2\bar{\mathcal{V}}_{j-1}}{(\bar{r}_j - \bar{r}_{j-1})(\bar{r}_{j+1} - \bar{r}_{j-1})} - \frac{2\bar{\mathcal{V}}_j}{(\bar{r}_j - \bar{r}_{j-1})(\bar{r}_{j+1} - \bar{r}_j)} + \frac{2\bar{\mathcal{V}}_{j+1}}{(\bar{r}_{j+1} - \bar{r}_j)(\bar{r}_{j+1} - \bar{r}_{j-1})} \right)^2, \tag{4.11}$$

where $\bar{r}_j$ are the center of mass of each $\bar{\mathcal{V}}_j$, defined by:

$$\bar{r}_j = (r_{j-1} + r_j)/2.$$

The new function to minimize is now:

$$\sum_{i \in \mathcal{D}} \left(V_i/\sigma_i - \sum_{k=1}^{N} \mathbf{B}_{ik} \bar{\mathcal{V}}_k \right)^2 + \lambda \sum_{k=1}^{N} \left(\sum_{j=1}^{N} \mathbf{G}_{kj} \bar{\mathcal{V}}_j \right)^2 , \tag{4.12}$$

where the matrix $\mathbf{G}$ is defined in such a way that

$$F(\bar{\mathcal{V}}) = \sum_{k=1}^{N} \left(\sum_{j=1}^{N} \mathbf{G}_{kj} \bar{\mathcal{V}}_j \right)^2 .$$

The parameter λ is a free parameter that controls the 'amount' of smoothness as opposed to a direct minimization of Equation (4.8). Again, differentiating with respect to $\bar{\mathcal{V}}_j$ and equating to zero we get the equivalent of Equation (4.10):

$$\sum_{k=1}^{N} \mathbf{M}_{jk} \bar{\mathcal{V}}_k = \sum_{i \in \mathcal{D}} (\mathbf{B}^T)_{ji} (V_i/\sigma_i) \qquad j = 1, \ldots, N , \tag{4.13}$$

where

$$\mathbf{M} = \mathbf{B}^T \mathbf{B} + \lambda \mathbf{G}^T \mathbf{G} . \tag{4.14}$$

The solution to this system of linear equations for $\bar{\mathcal{V}}_k$ is:

$$\bar{\mathcal{V}}_k = \sum_{j=1}^{N} (\mathbf{M}^{-1})_{kj} \sum_{i \in \mathcal{D}} (\mathbf{B}^T)_{ji} (V_i/\sigma_i) . \tag{4.15}$$

The substitution of these results in Equation (4.6) at r_0 gives

$$\bar{\mathcal{V}}(r_0) = \sum_{i\in\mathcal{D}} \left(\sigma_i^{-1} \sum_{k,j=1}^{N} \phi_k(r_0)(\mathbf{M}^{-1})_{kj}(\mathbf{B}^T)_{ji} \right) V_i \equiv \sum_{i\in\mathcal{D}} c_i(r_0) V_i \,, \tag{4.16}$$

an explicit form of Equation (4.5). The averaging kernels can then be calculated with Equation (4.4).

The parameter λ not only controls the smoothness constraint, but also the trade-off between resolution and error magnification. On one hand, if $\lambda = 0$, the equation to minimize is Equation (4.8), and the result will be the best fit of the data. In this case, the coefficients $c_i(r_o)$ will be chosen such that the averaging kernels are as close as possible to δ-functions. There will be almost no averaging effect, but the error magnification will be very high. On the other hand, for higher values of λ, the width of the averaging kernels increases due to the dependence of the coefficients $c_i(r_o)$ on λ from Equation (4.16), and the averaging and smoothing effects produce more stable results, with lower errors. At the same time we lose resolution by averaging with wider resolution kernels.

4.2 Tridimensional velocity flows

This last inversion technique has been applied to our data. The first step before the calculations is to get the set of kernels $K_i(r)$ given by the theory of solar oscillations. Kernels have been calculated in the theory for the radial distribution of the horizontal velocity flows; in this case a set of kernels obtained for a standard solar model by Bahcall & Ulrich (1988) has been used. This set of kernels has been modified for use in this study. Since the ring analysis is a local rather than global analysis, it uses waves that are not spatially coherent over the entire sun. While these waves must still satisfy the resonance condition for their vertical wavenumber, their horizontal wavenumbers

can assume any value unlike the global modes which are constrained to wavenumbers corresponding to integer values of spherical harmonic degree l. In effect the local waves can have fractional l values, e.g. 482.645. The kernels obtained from solar models are necessarily for global modes with integer l values. We must construct kernels for waves with fractional l values by linear interpolation between kernels with integer l values. In addition, since the rings are actually offset from $k_x = k_y = 0$ and are not precisely circles, the total horizontal wavenumber varies as a function of azimuthal angle around the ring. We thus use the azimuthal average total horizontal wavenumber around a ring to specify the fractional l value for that ring. The interpolation is entirely equivalent to solving the acoustic-gravity wave equation in the stratified medium of the solar convection zone and, in fact, provides identical eigenfunctions (Gough 1993, private communication). Figure 4.1 shows a sample of the kernels used in the inversions. Once we have the kernels, we calculate the estimated values for the velocities $\bar{\mathcal{V}}(r)$ from Equation (4.16), for a given λ.

Several tests with different values for the smoothness parameter ranging $0.1 \leq \lambda \leq 5.0$ have been performed. Average trade-off curves, computed by averaging the 18 trade-off curves for the 9 subrasters and the 2 velocity components, are plotted in Figures 4.2 and 4.3, this last showing a sample with $1-\sigma$ error bars in it. Every curve in Figure 4.2 corresponds to a given target radius $r_0/R_\odot$ and is plotted for the 10 values chosen for λ. The lowest error magnification and greatest half-width in every curve corresponds to the highest smoothness parameter, $\lambda = 5.0$. The half-width parameter is defined as the distance between the 25^{th} and 75^{th} percentile points of the area under the averaging kernel. Notice how the same range of values of λ samples different regions in these plots for different target depths. This makes the choice of λ difficult: a good trade-off between averaging effect and error magnification that is acceptable for a given target depth may be not as good at another depth. In general, the value $\lambda = 5.0$ is a good choice in our case because, even though the half-width is high for the deepest depths, we are more interested in the results closer to the solar surface, where the half-width is

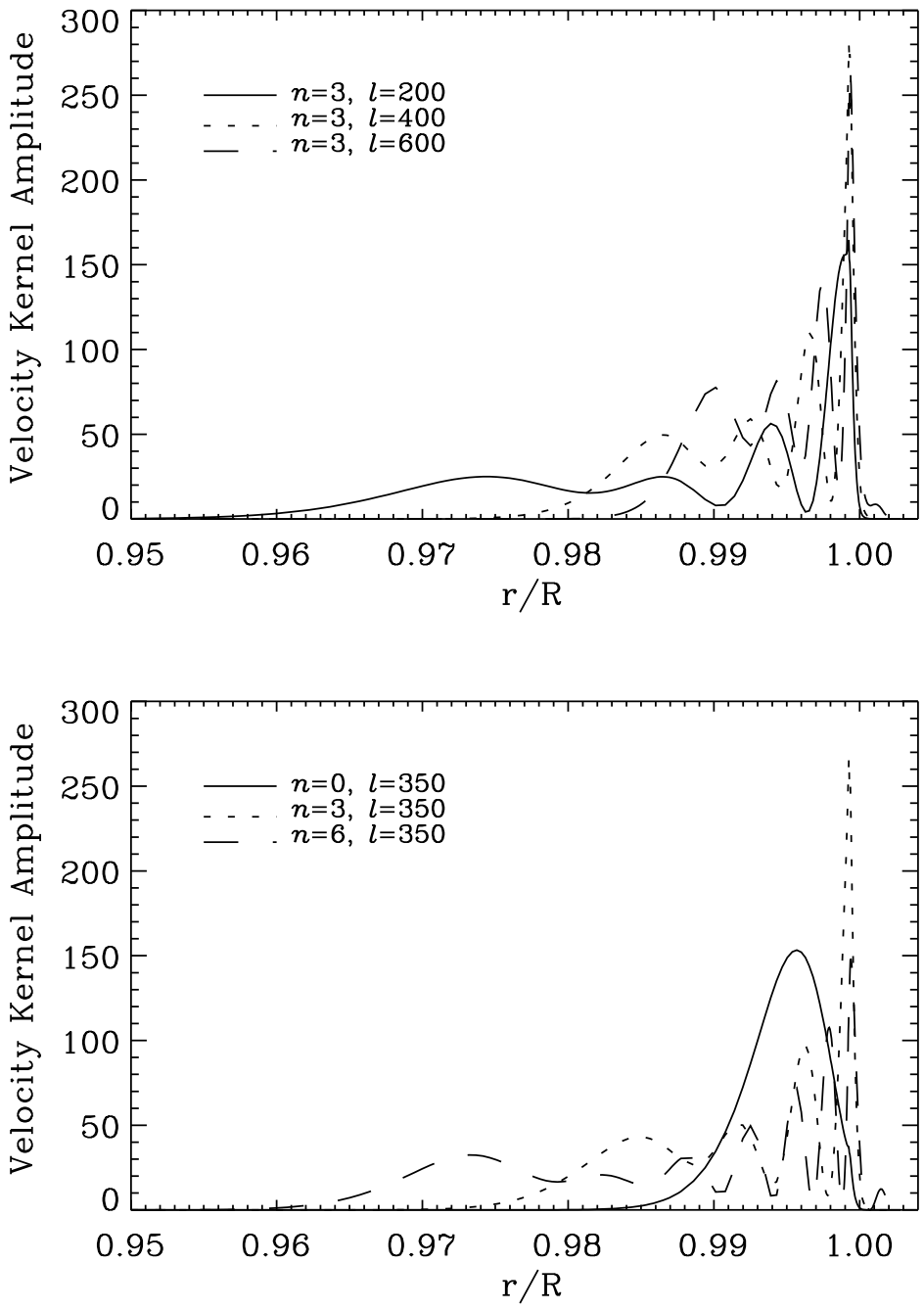

Figure 4.1: Sample of velocity kernels for several modes.

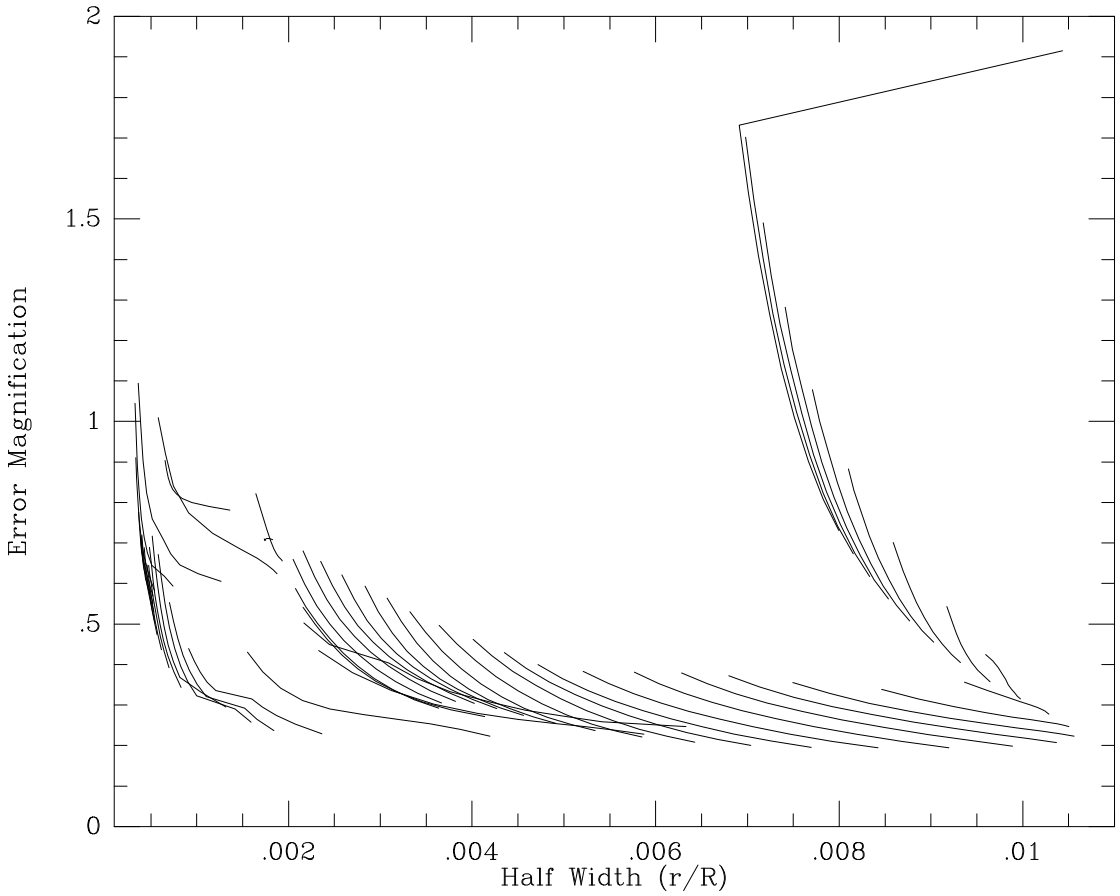

Figure 4.2: Trade-off curve for the 51 target radius chosen in the inversions. In a single line λ grows down and to the right. From left to right, depth is increasing from the solar surface to 0.905 $R_\odot$.

smaller. On the other hand, the information that we obtain at the deeper depths comes from the modes of low l, where the plane wave approximation that we have assumed start to break down. Finally, a sample of the results for the averaging kernels obtained for $\lambda = 5.0$ and several target radius $r_0/R_\odot$ is showed in Figure 4.4 .

The inversion is performed for every one of the nine subrasters and for both latitudinal and longitudinal velocities. Approximately 1700 modes, with $0 \leq n \leq 7$, and

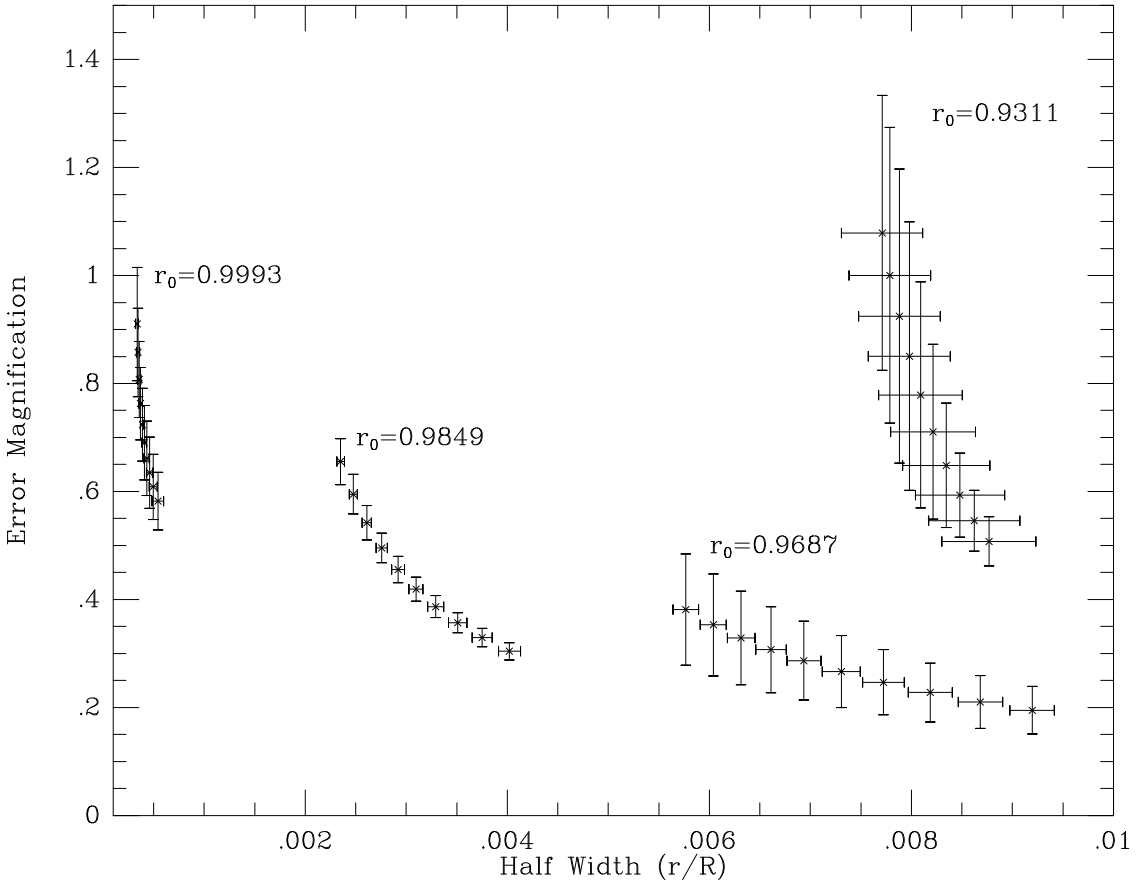

Figure 4.3: A sample of the error bars for several of the tarde-off curves.

$175 \leq l \leq 800$ have been used in every inversion. The discretization of the problem has been performed by taking a total of 51 dissections covering the depth range $0.9 \leq r/R_{\odot} \leq 1.0$. The final results presented in this work were obtained for $\lambda = 5.0$, the smoothest solutions with the lowest errors, but the worst depth resolution. The results of the inversions are shown in Figures 4.5 and 4.6, where U_x and U_y appear as a function of depth for the 9 subrasters. Positive values are eastward for U_x and southward for U_y. For reference, the depths of the three hydrogen and helium ionization zones are indicated.

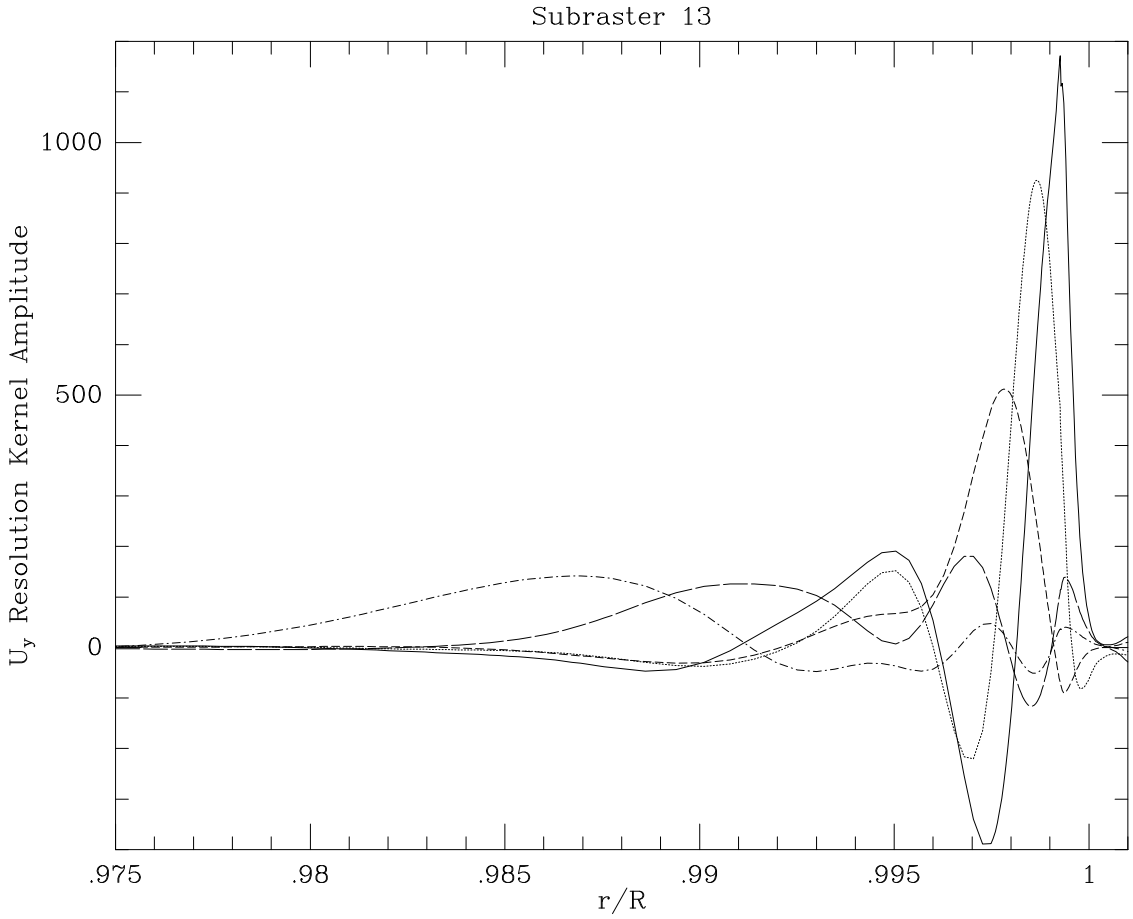

Figure 4.4: Sample of averaging kernels obtained for $\lambda = 5.0$ at 5 different target radius $r_0/R_\odot$: 0.9993 (solid), 0.9987 (dotted), 0.9978 (dashed), 0.9924 (long dashes) and 0.9849 (dash-dot).

The magnitudes of the flows are substantial: 100–200 ms^{-1} in the outer convection zone, rising to 500 ms^{-1} at the deeper depths (not shown in the figures). There are striking similarities between the velocity curves at different positions. Specifically, most of the curves show a sharp maximum immediately below the surface and a broad maximum between the two helium ionization zones.

In order to visualize the actual velocity flow field Figure 4.7 shows the vector velocities at target depths ranging from $r/R = 1.0014$ to $r/R = 0.92537$ for the 9

subrasters, as the results for $\lambda = 5.0$. To enhance the orientation of the vectors, the colors are different for every orientation, going clockwise from 12 o'clock: blue, magenta, red, yellow, green and cyan. For an overview of the variation on the orientation of the velocity flows with depth, the color curves in Figure 4.9 represent the evolution of the arrow-head of the velocity vectors with depth (color code); the white dot shows the starting point at the solar surface. The crossings of the vertical and horizontal lines mark both the position of the subrasters and the origin of the vectors.

The most striking feature is the coherent organized rotation of the velocity vectors for some of the subrasters through about 360°. The vector velocity field thus appears to perform a spiral in depth, as can also be seen in the pseudo-perspective view of the vectors in Figure 4.8. Here the solid lines are drawn parallel to constant depth planes and represent the magnitude of the horizontal velocity flows (a segment correspondent to 200 ms^{-1} is showed). Every spiral is shown at a point representing the position on the solar disk by latitude and longitude; the words 'East' and 'North' and the letters 'S' (South) and 'W' (West) show the orientation of the view. The extent in depth shown here is only about 10 Mm into the sun, in order to have a good view of the upper convection zone. At deeper depths, the flows grow bigger and, at about 30 Mm, the spatial coherence nature of the flow field disappears and the flows become chaotic as can be seen in Figure 4.7. A spiral nature of the flow field has been seen also in numerical convection models (Brummell *et al.* 1992). In Figure 4.9 it can also be noticed also that from 20 Mm to 60 Mm, there are no big changes in the orientation of the vectors with depth.

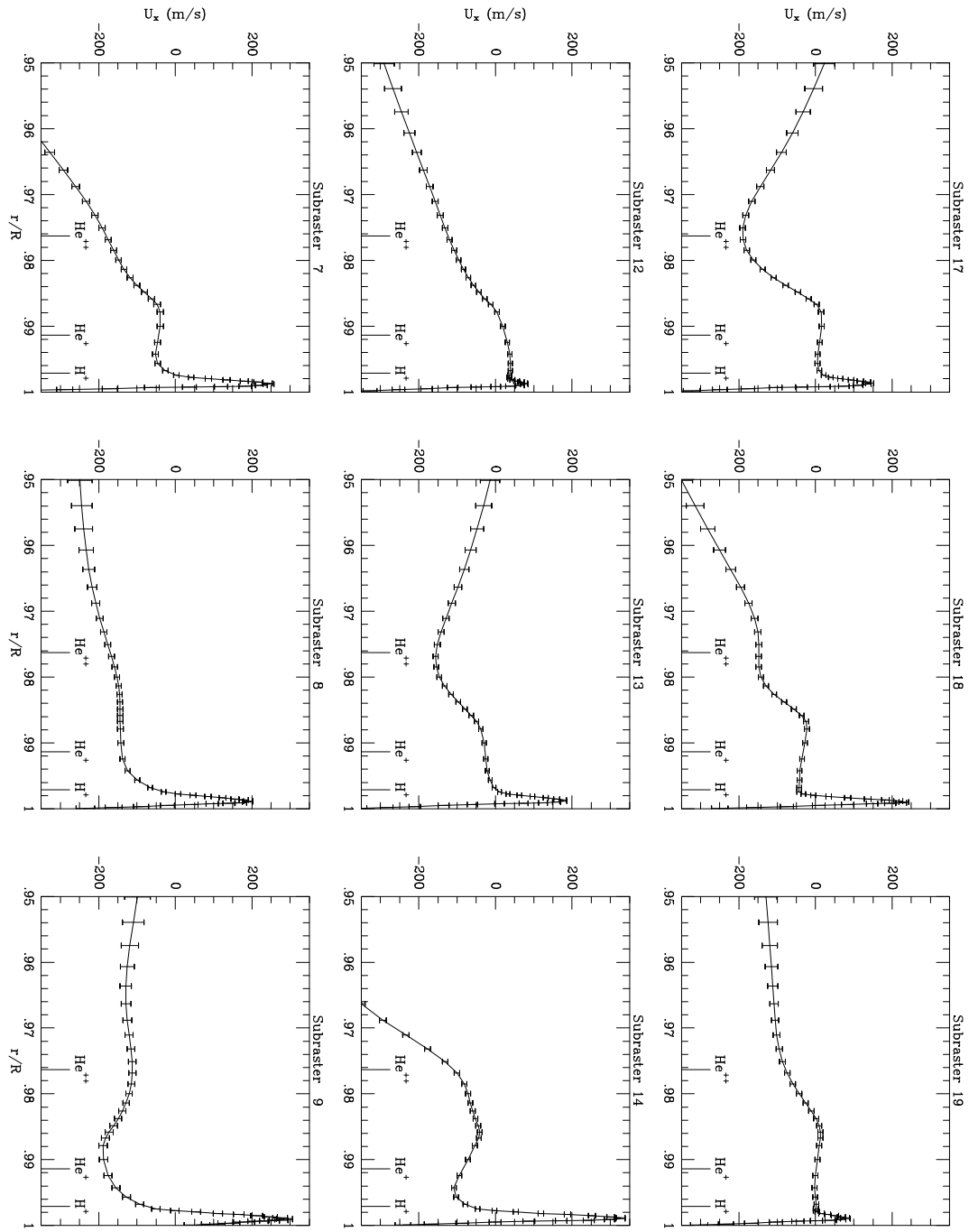

Figure 4.5: U_x velocity flows as a function of depth for the 9 subrasters. The sign convention is that $U_x > 0$ is eastward (faster than surface rotation).

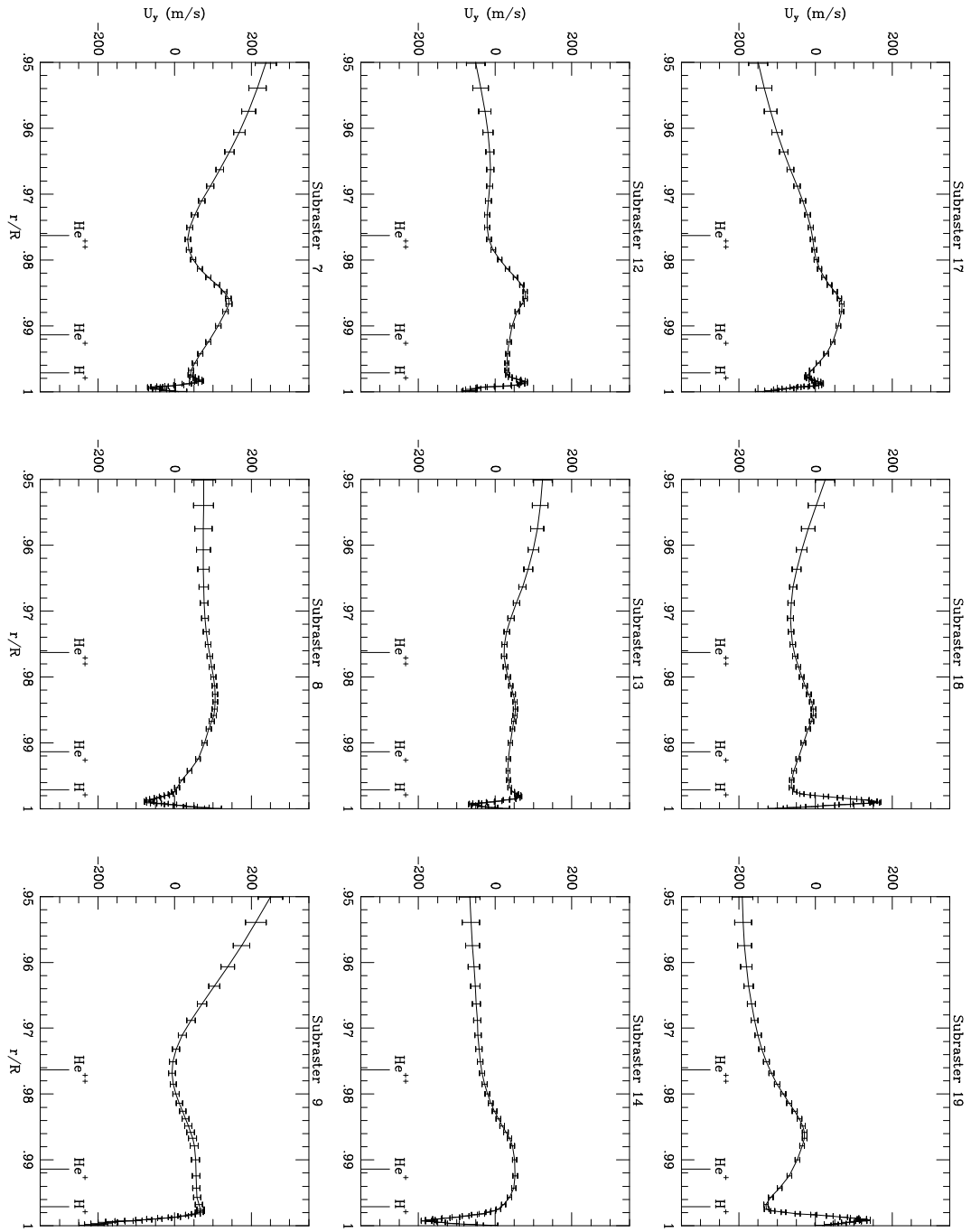

Figure 4.6: U_y velocity flows as a function of depth for the 9 subrasters. The sign convention is that $U_y > 0$ is southward.

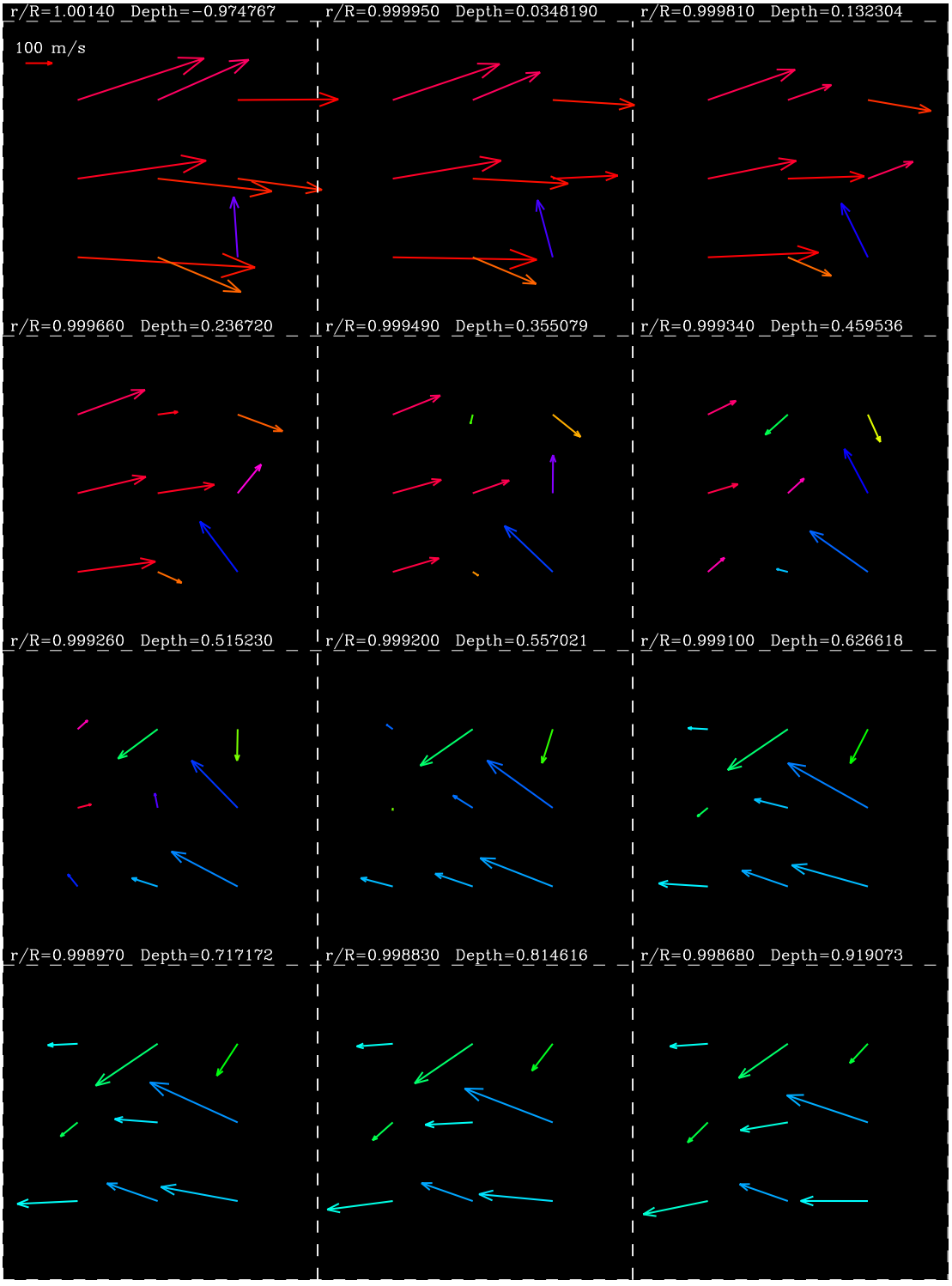

Figure 4.7: Vector velocities for the 9 subrasters (the 9 vectors in every dashed region) at target radius ranging from $r/R = 1.0014$ to $r/R = 0.99868$. Results are showed for $\lambda = 5.0$. Orientations are indicated by color also; going clockwise from 12 o'clock: blue, magenta, red, yellow, green, cyan. The units of depth are Mm.

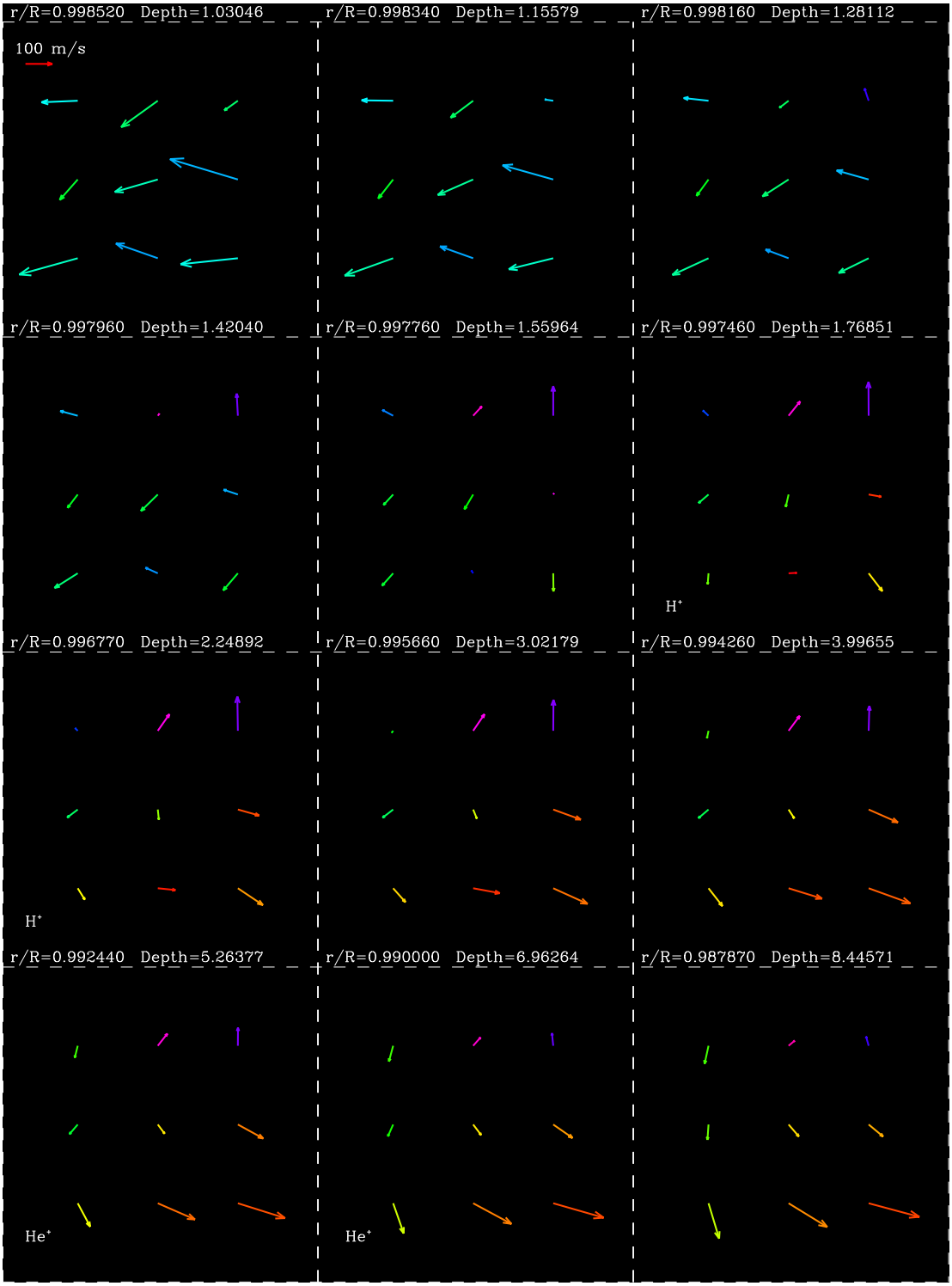

Figure 4.7: Continued. Target radius ranging from $r/R = 0.99852$ to $r/R = 0.98787$. Estimated depth of the ionization of H and He are showed by H^+ and He^+ .

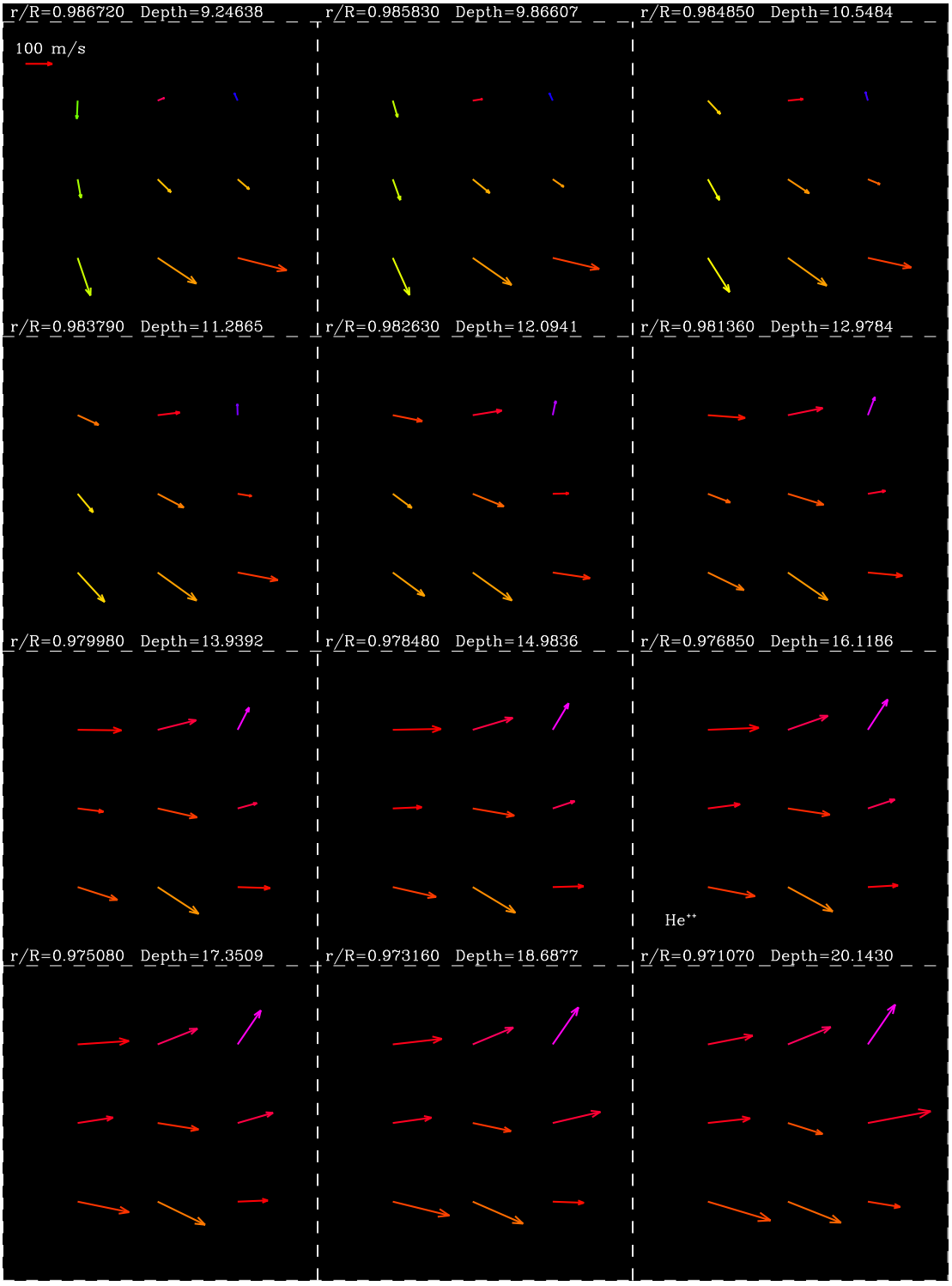

Figure 4.7: Continued. Target radius ranging from $r/R = 0.98672$ to $r/R = 0.97107$. Estimated depth of the second ionization of He is showed by He^{++} .

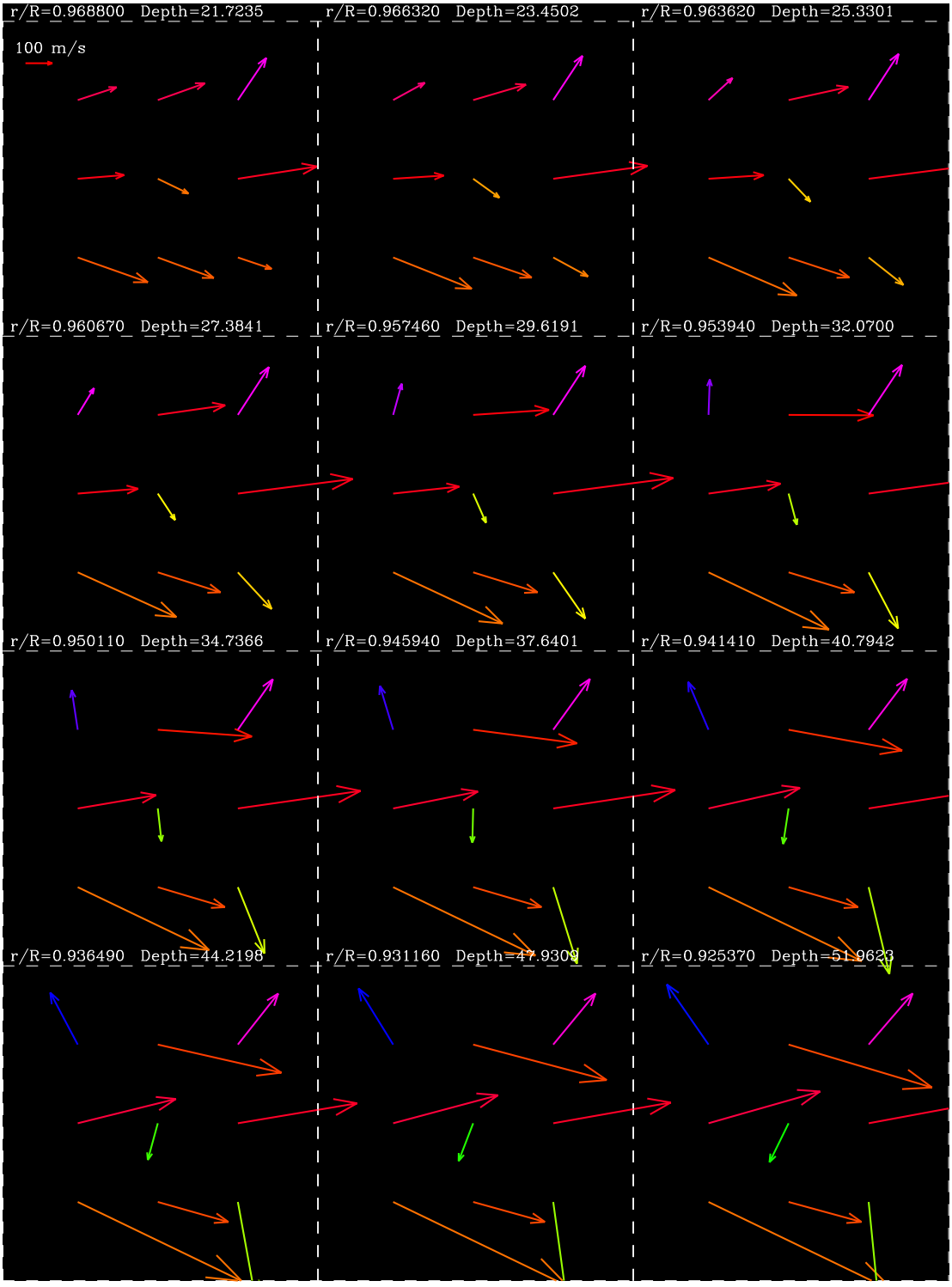

Figure 4.7: Continued. Target radius ranging from $r/R = 0.9688$ to $r/R = 0.92537$.

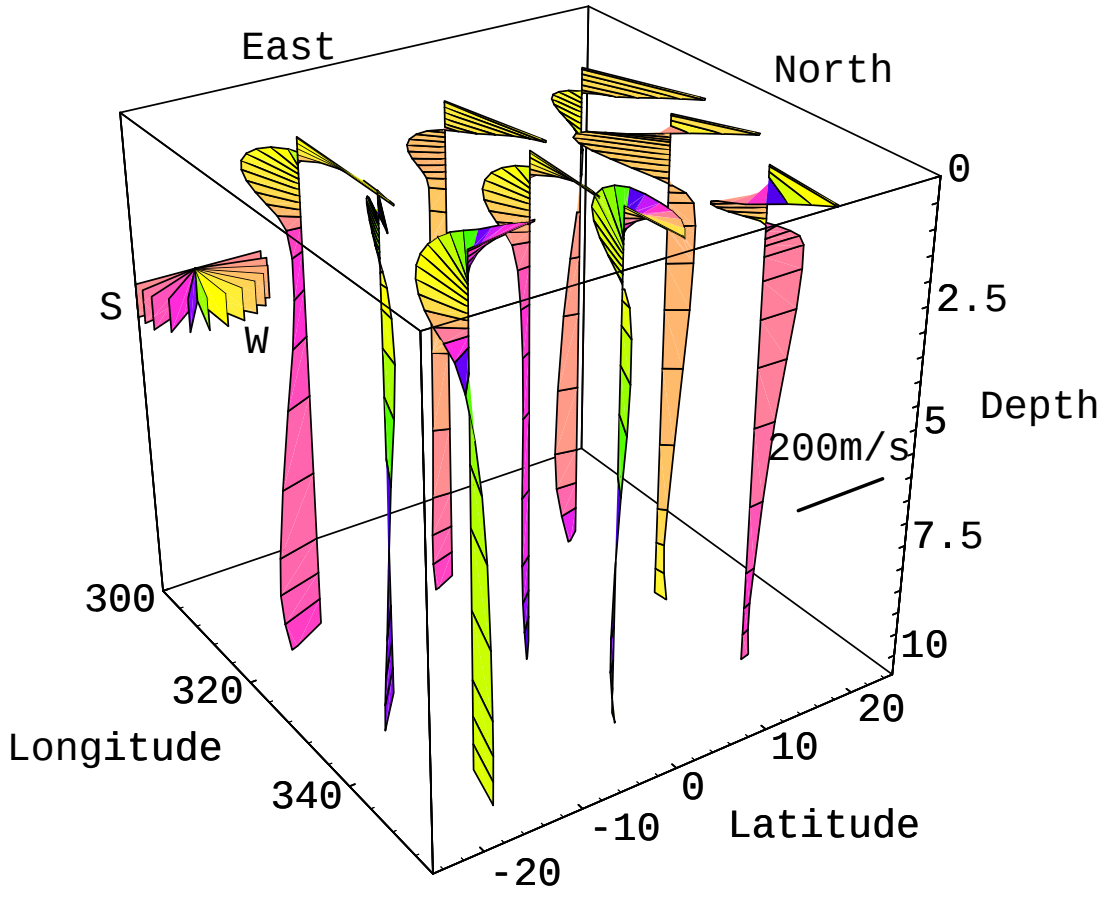

Figure 4.8: Tridimensional aspect of the velocity flows for the nine subrasters for a section in depth of about 10 Mm into the solar surface. Parallel lines to the lat-long plane are proportional to the velocity vectors. The colors help to appreciate the orientation of the flows. Numbers in the lat-long plane are degrees, and the units in depth are in Mm.

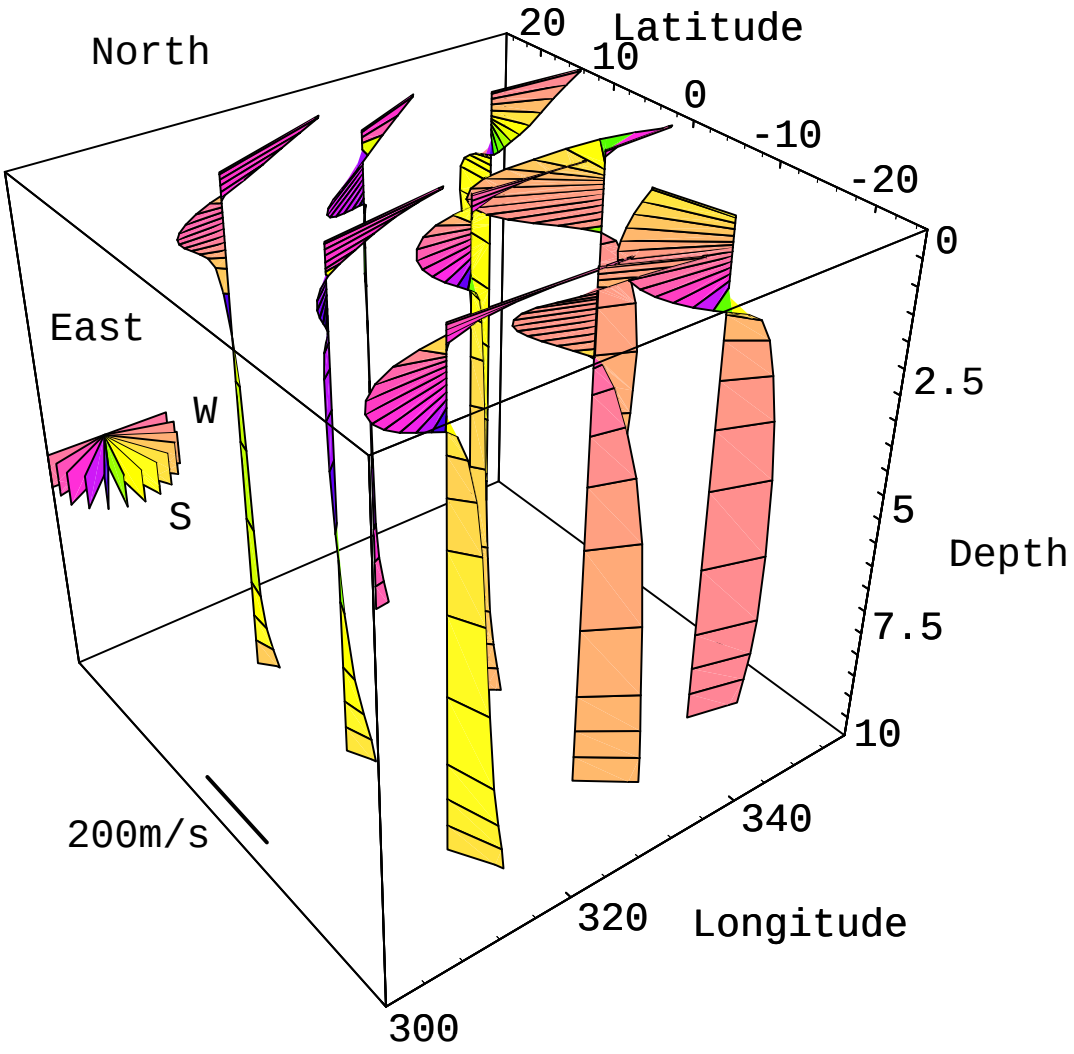

Figure 4.8: Continued. Another view of the same plot as before.

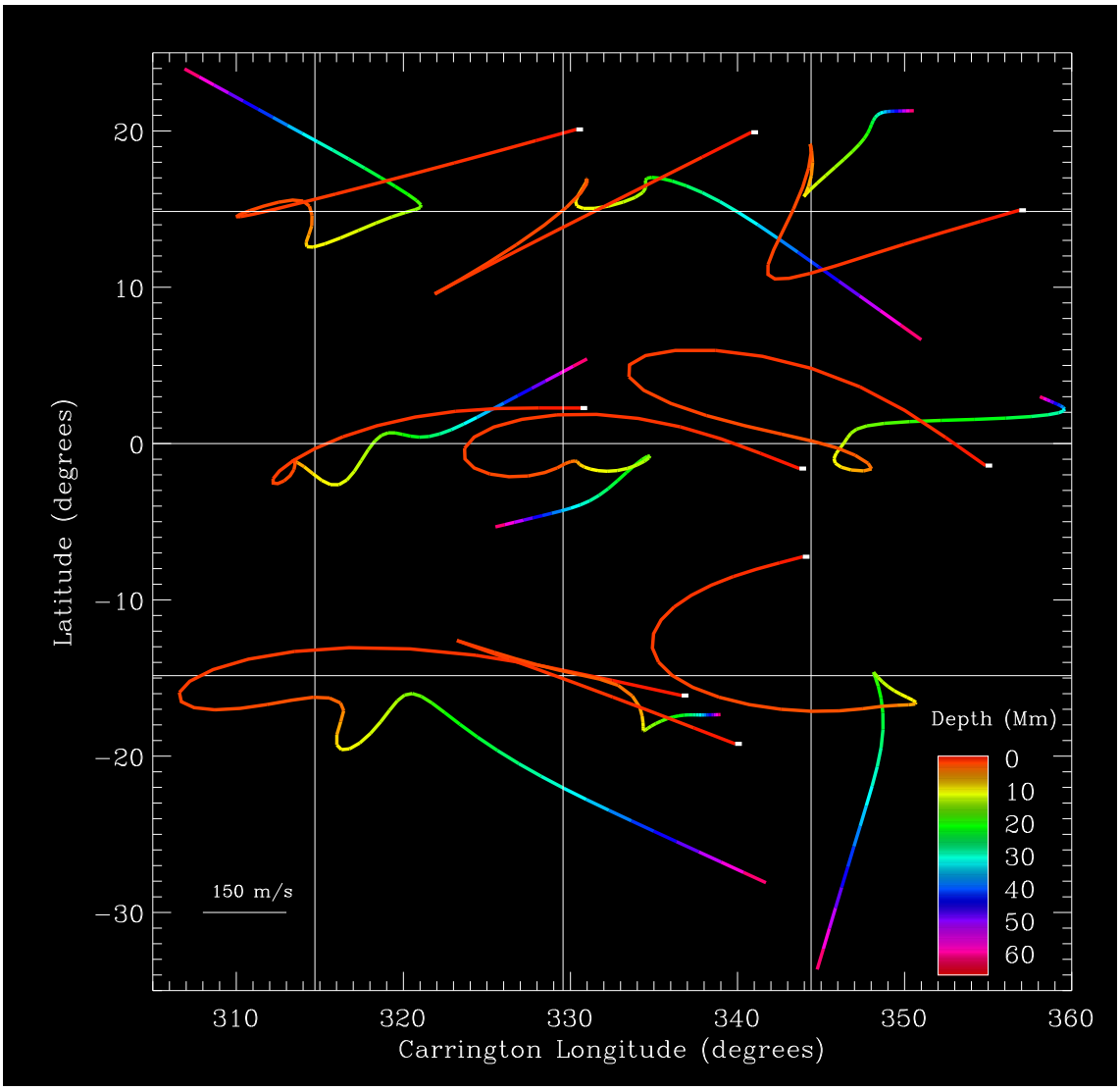

Figure 4.9: A view of the evolution of the orientation of the vector velocities with depth for the 9 subrasters. The curves follow the arrow-head of the vectors and the color code gives the depth information. The intersection of the white lines mark both the positions of the 9 subrasters and the origin of the vectors. White dots show the starting position at the solar surface.

Chapter 5

Conclusions

In this chapter, we put aside the question of the reliability of the results obtained in this work, and assume that the results reflect what is really happening in the sun. We have obtained the horizontal velocity flow field as sampled at 9 different positions over the solar disk, and 51 points in depth: layers of fluid material moving in different horizontal directions and rates, at different depths, ranging from the solar surface down to about 60 Mm deep inside. This is just an estimate of the fluid-dynamics state of the upper convection zone of the sun.

As was pointed out in the introduction, heliosismology can provide us with information about the fluid dynamics of the solar interior. But, before going further, it is necessary to give an interpretation of the estimated velocity flows and compare these results with theory.

In the last section of this chapter further work, tests and improvements of the techniques developed along this work are presented for the future.

5.1 Convective cells, magneto and hydrodynamics

Convective cells are structures of fluid moving from deeper depths to the upper layers, and back to the bottom. Thus the vertical flow of the material must change direction towards a horizontal flow at two positions: the bottom and top of the convective cell. In a depth distribution of the velocity flow, these turning points may be represented by peaks in the velocity profile. In Figure 5.1 the modulus of the velocity vectors of the 9 subrasters as a function of depth is shown. Notice the non-linear scaling in depth as a consequence of the disections selected in the inversion process. Several general features, obtained for most of the subrasters, and similar to the ones found in Figures 4.5 and 4.6, can be pointed out:

- The velocity is at a maximum at the surface, drops to a minimum and then rises back to a peak, immediately above the hydrogen ionization zone at a depth of about 1 Mm. Looking at Figure 4.7 the vectors in most of the subrasters are pointing west for the solar surface and east for this other depth in two strong shear layers in opposite directions. Both of these strong shear layers may be the source of instabilities that could cause the granulation, which has a spatial scale of 1 to 2 Mm. In addition, this shear layer may be the mechanism that causes the excitation of the acoustic modes. This source has been estimated to be found close to the solar surface at a depth of 150Km, by Kumar (1992), or even closer at 60Km, by Duvall *et al.* (1993).

  The presence of a peak close to the solar surface in the depth profile of the horizontal velocity flows and rotation rate has been found in other works (Hill *et al.* 1988, Hill 1990, Korzennik 1990). Note that the amplitudes and positions of these peaks vary among different works. However, since the analysis has been performed on data sets taken at different periods of time, it may indicate the time evolution of this phenomenon.

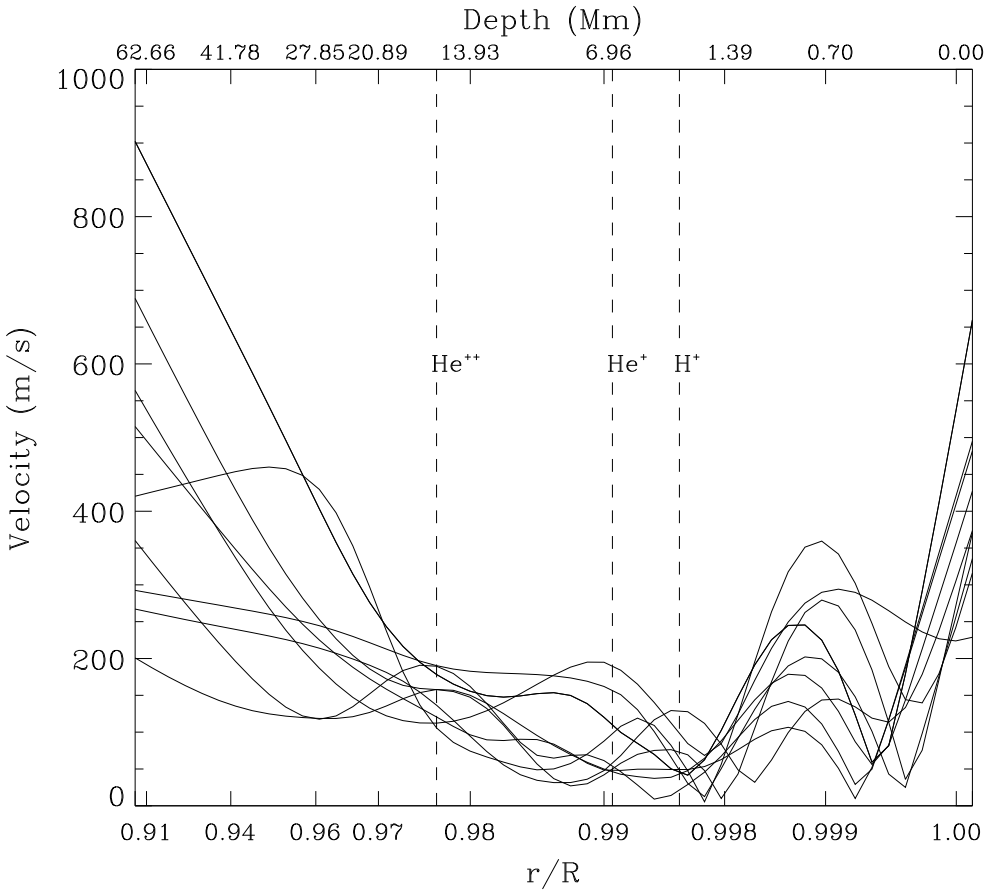

Figure 5.1: Modulus of the velocity vectors as a function of depth for the 9 subrasters. Notice the non-linear depth scale.

- Below the He^{++} zone, at 18 Mm, the curves raise smoothly from values of 200 ms^{-1} to values of 500 ms^{-1} at 60 Mm. Looking at Figure 4.7 , after 30 Mm, we see that the spatial coherence of the orientation of the flow field disappears and the flows become chaotic.

- There are several broad maxima between the ionization zones of hydrogen and helium at depth of 2 to 16 Mm. This zone seems to be a transition between the rapidly changing zone above 2 Mm (two sharp peaks in 2 Mm), and the smoothly changing zone under 18 Mm (no clear peaks in about 40 Mm).

Looking again at Figure 4.7 , we see another shear layer oriented westward at about 16 Mm, near the depth of the He^{++} zone. There is thus a relativily close association in depth between the two prevalent east-west shear layers with the H^{+} and He^{++} ionization zones in the outer 20 Mm. This is in agreement with anelastic compressible convective models, which predict that giant cell vertical flows would be deflected into strong horizontal flows in the vicinity of the ionization zones (Latour *et al.* 1983).

Another interesting aspect of the flows obtained in this work are the spirals that the vector velocities perform as a function of depth. It could be a source of the helicity of the solar magnetic field. It is clear that magnetic field lines anchored to the plasma that is moving and performing spirals would show the same structures. In the other hand, this spiral movement of the fluid can produce cyclonic flows that have been postulated as the origin of the helicity of the magnetic fields and the dynamo process in the sun (E. Parker 1955b; DeLuca 1991). From a fluid-dynamics point of view, theoretical models for turbulent convection in a compressible and rotating fluid (Brummel *et al.* 1993) predicts mean horizontal velocity flows that performe spirals with depth, suggesting that this phenomenon is a consequence of the vorticity of the flows induced by the rotation.

The coherent nature of the flow field at the 9 positions, coupled with the plausible fluid dynamic scenario that it represents, suggests that the qualitative nature of the results may actually reflect the flows in the outer solar convection zone. Further examination of the vector velocity plots indicates that there may be a convective roll oriented east-west at a latitude of about $+10°$. The evidence for this is the convergent flows between subrasters 18 and 19 in the top row and the middle row of vectors at depth of 0.3 to 0.7 Mm, changing to divergent flows at depths of 1.4 to 8.4 Mm. This could be a sign of the presence of a toroidal convective roll.

While the amplitude of the flows may seem large, it should be recalled that jet streams in the Earth's atmosphere can reach amplitudes of 200 ms^{-1} . The solar flows

here may be eventually revealed to be solar jet streams.

The results can be compared with an earlier flow map inferred by Hill in 1990 from a different data set with a different ring fitting procedure, and a different set of inversion kernels. That map also showed rotating flows with the spiral structures. However, the flow was only seen to rotate over 90°, the direction of the rotation is the opposite to the showed here, and the maximum U_x was at a different depth than in this data set. This is not surprising since this data set corresponds to 1981, seven years apart from our data set. We may be just seeing the velocity flow evolution with time.

5.2 Further work

- The reliability of these results needs to be tested. For this, besides more measurements and new data analysis, we need to create a good set of simulations and apply the reduction process to them. Simulations should be based on a superposition of plane waves for the set of modes we expect to use in the reduction, i.e. on the order of 1700.

  The solar model applied in the inversions must be used to simulate the depth dependence of the wave field including the advection effect of the horizontal velocity flows. The final result will be the velocity state of the solar surface after the addition of the wave fields. A temporal series must be constructed, and the periods of the waves obtained from an accurate dispersion relation. Another posibility is the use of actual measurements of the frequency of the modes.

  The final test will consist of constructing these temporal series for different distributions of flow fields with depth and position, and applying the whole reduction process to them. Hopefully we would recover the input velocity flows.

- Interpolation processes introduce systematic errors. In the reduction process the two interpolations performed in the remapping and tracking can be reduced to one,

doing all the geometric transformation of both processes at once in a remaping-tracking procedure.

- A fine structure of the spatial distribution of the velocity flows in the solar disk can be obtained by choosing sections of data that overlap in the solar disk.

- It is vital to speed up the fitting procedure. Besides the use of new fitting procedures, a preliminary fit of parameters like amplitude and width of the Lorentzian profiles and the background of the power spectrum can be performed in the azimuthally averaged l–ν diagram. This is a two-dimensional fit with a reduced number of parameters in the fit. The three-dimensional fit will have only the two components of the velocity flows as parameters to fit, which will speed up the process.

- It is essential that more data be analyzed and the temporal behavior of the flows understood. This is particularly useful in order to correlate the flows with the surface solar activity. At the same time, some systematic errors could be detected.

- It is also important that the analysis be carried out on different yet similar data sets obtained simultaneously. This will be possible using the Mt. Wilson and NSO High-Degree Helioseismometer data sets, and the future data from SOI (Solar Oscillation Investigation) and TON (Taiwan Oscillations Network).

- Another test of the results could be done by following tracers on the solar surface, getting local values for surface flows and comparing them to the values of our data close to the solar surface.

- Additional future work includes the application of different inversion methods with improved mode sets.

- The more difficult fitting of the partial rings from subrasters closer to the limb should be studied. Some effort has been made to correct the foreshortening in the partial rings (Hill & Patrón 1992), however without success. The effect of the

foreshortening can be modeled as a special kind of convolution with a spatially varying point spread function. The initial idea was to remove the effect after the spatial FFT, taking advantage of the properties of the convolution theorem. However, the relation is not a convolution, and must be removed in some other way.

- Experiments with the tradeoffs of subraster size and spatial resolution should be tried. The two-dimensional spatial FFT performed on the subrasters has a averaging effect over the spatial distribution of the fitted parameters. Smaller sections will give more spatial resolution at the expense of less spatial wavenumber resolution.

- In section 2.2 of this dissertation, we remaped the solar disk onto a latitude-longitude grid, with an equally-spaced distribution of the pixel information. However, the spacing is equal in an angular way. Due to foreshortening, the final remapped image will have pixels that sample different areas of the solar surface as we move towards higher latitudes: one squared pixel of n by n degrees (n being the resolution of the image in degrees) at the equator subtends a bigger area than the same pixel at, say, 40° degrees of latitude (see Figure 5.2). The area depends on the spatial dimensions on the solar surface, and these depend on the distance to the symmetry axis (perpendicular to the equator) at a given latitude, which is shorter for higher latitudes.

  Another possibility is to remap using units of arclength, so the area of a unit pixel in the remapped image is the same regardless of the values of the coordinates. This remapping provides a better representation of the waves. Plane waves propagate in all possible orientations and there is no reason to believe that the pattern will be different if we look at the equator or if we look at the poles. If we assume a lat-long distribution, we are expecting to find at the poles something close to a 'dart board' picture, and not a 'chess pattern' as expected around the solar equator. But plane waves do not care about poles and equators. The wave just

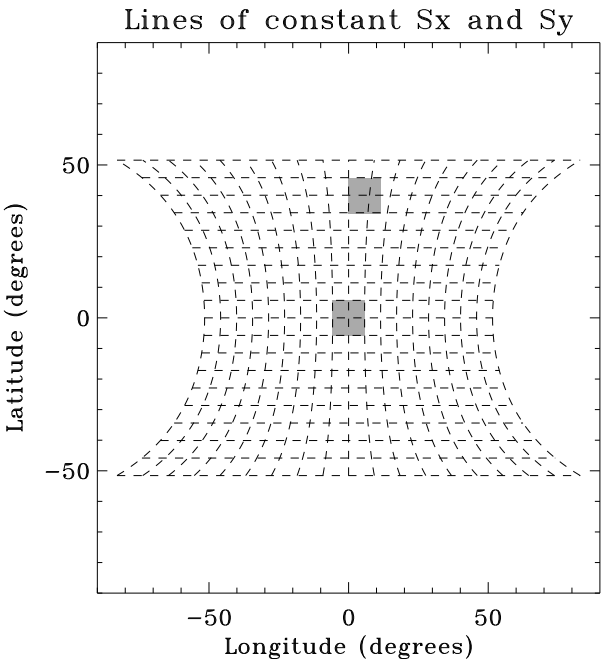

Figure 5.2: Lines of constant S_x and S_y (arclength coordinates) in a latitude-longitude grid. Notice how the shaded area at $L = B = 0$ in the angular grid covers a different area in the spatial coordinate system for a different position, and vice versa.

travels, and it does not behave differently when it goes towards the poles or when it goes towards the equator.

An equal arclength (or great circle) grid looks like the appropriate coordinate system for the remapping. Unfortunately, preliminary tests of this new remapping grid did not produce good results. But, considering that we are working with sections close to disk center (we never go further than $\pm 22°.3$ in latitude), the effect of the unequal sampling of areas is not large (a maximum of 7.4% of difference between the area at the center and the farthest one), and, after our unsuccessful experiment with the arclength grid, we decided to apply a latitude-longitude remapping for our images.

Later works in tridimensional power spectrum have been realized by Haber, Gough and F. Hill (personal communications) for great circle grids, and the results are

very promising. Working with an arclength grid, they have been able to find the patterns of the oscillations (the 'trumpets') in the power spectrum of sections taken as far as 70° in latitude. Doing the same analysis for a lat-long grid, the final results show basically no power distribution for such latitudes. This suggests that plane waves prefer equal arclength distributions instead of the equal angular distribution of a lat-long grid.

Bibliography

Anderson, E. R., Duvall, T. L., Jr., and Jefferies, S. M. 1990, *Astrophys. J.,* **364**, 699.

Backus, G. E., and Gilbert, J. F., 1968, *Geophys. J.*, **16**, 169.

Bahcall, J.N., and Ulrich, R.K., 1988, *Rev. Mod. Phys.*, **60**, 297.

van Ballegooijen, A. A., 1986, *Astrophys. J.,* **304**, 828.

Brookes, J. R., Isaack, G. R., and Van der Raay, H. B., 1976, *Nature* , **259**, 92.

Brown, T. M., 1986, in *Seismology of the Sun and the Distant Stars* , ed. D. O. Gough (Doldrecht: Reidel), 199.

Brown, T. M., Mihalas, B. W., and Rhodes, E. J. Jr., 1986, in *Physics of the Sun, Vol. I: The Solar Interior* , ed. P. A. Sturrock, T. E. Holzer, D. M. Mihalas, and R. K. Ulrich (Doldrecht: Reidel), Chap. 7, 177.

Brown, T. M., Stebbins, R. T., and Hill, H. A., 1978, *Astrophys. J.,* **223**, 324.

Brummell, N. H., Hurlburt, N. E., Toomre, J., 1992, in PASP Conference Series, Vol. **42**, *GONG 1992: Seismic Investigation of the Sun and Stars* , ed Timothy M. Brown, 437.

Christensen-Dalsgaard, J., 1988, in *Seismology of the Sun and Sun-like Stars* , ed. E. J.

Rolfe (Paris: ESA SP-286), 431.

Christensen-Dalsgaard, J., Gough, D.O., and Thompson, M.J., 1991, *Astrophys. J.,* **378**, 413.

Christensen-Dalsgaard, J., Schou, J., Thompson, M. J., 1990, *Mon. Not. R. astr. Soc.*, **242**, 353.

Claverie, A., Isaak, G. R., McLeod, C. P., van der Raay, H. B., and Roca Cortés, T., 1979, *Nature* , **282**, 591.

DeLuca, E. E., 1991, in *The Solar Interior and Atmosphere* , ed. A. N. Cox, and W. C. Livingston, (The University of Arizona Press), 275.

Deubner, F. L., 1975, *Astron. Astrophys.,* **44**, 371.

Deubner, F. L., Ulrich, R. K., and Rhodes, E. J., 1979, *Astron. Astrophys.,* **72**, 177.

Dicke, R. H., and Goldenberg, H. M., 1967, *Phys. Rev. Lett.*, **18**, 313.

Durney, B., 1970, *Astrophys. J.,* **161**, 1115.

Duvall, T. L. Jr., and Harvey, J. W., 1986, in *Seismology of the Sun and the Distant Stars* , ed. D. O. Gough (Dordrecht:Reidel), 105.

Duvall, T. L. Jr., Jefferies, S. M., Harvey, J. W., Osaki, Y., and Pomerantz, M. A., 1993, *Astrophys. J.,* **410**, 829.

Foukal, P., 1972, *Astrophys. J.,* **173**, 439

Gilman, P. A., 1986, in *Physics of the Sun, Vol. I: The Solar Interior* , ed. P. A. Sturrock, T. E. Holzer, D. M. Mihalas, and R. K. Ulrich (Doldrecht: Reidel), Chap. 5, 95.

Gough, D. O., 1969, *J. Atmos. Sci.*, bf 26, 448.

Gough, D. O., 1981, *Mon. Not. R. astr. Soc.*, **196**, 731.

Gough, D. O., 1985, *Solar Physics* , bf 100, 65.

Gough, D. O., and Toomre, J., 1983, *Solar Physics* , bf 82, 401.

Gough, D. O., and Toomre, J., 1991, *Annu. Rev. Astron. Astrophys.*, **29**, 627.

Gough, D. O., and Weiss, N. O., 1976, *Monthly Notices Roy. Astron. Soc.*, **176**, 589.

Hart, J. E., Glatzmaier, G. A., Toomre, J., 1986, *J. Fluid Mech.*, **173**, 519.

Harvey, J. W., 1985, in *Future Missions in Solar, Heliospheric, and Space Plasma Physics* , ed. E. J. Rolfe and B. Battrick (Paris: ESA SP-235), 199.

Harvey, J. W., and the GONG Instrument Development Team, 1988, in *Seismology of the Sun and Sun-like Stars* , ed. E. J. Rolfe (Paris: ESA SP-286), 203.

Hill, F., 1988, *Astrophys. J.,* **333**, 996.

Hill, F., 1990, *Solar Physics* , **128**, 321.

Hill, F., Deubner F.-L., and Issak, G., 1991a, in *The Solar Interior and Atmosphere* , ed. A. N. Cox, and W. C. Livingston, (The University of Arizona Press), 329.

Hill, F., Gough, D. O., Toomre, J., and Haber, D. A., 1988, in *Advances in Helio- and Asteroseismology* , ed. J. Christensesn-Dalsgaard and S. Frandsen, IAU, 45.

Hill, F., and Patrón, J., 1992, in *Bulletin of the American Astronomical Society* , **24**, 736.

Hill, F., Rhodes, E. J., Jr., Korzennik, S. G., Cacciani, A., and Brown, T. M. 1991b, in *Challenges to Theories of the Structure of Moderate-Mass Stars* , ed. D. O. Gough and J. Toomre, Berlin: Springer, 271.

Hill, H. A., Clayton, P. D, Patz, D. L., Healy, A. W., Stebbins, R. T., Oleson, J. R., and Zanoni, C. A., 1974, *Phys. Rev. Lett.*, **33**, 1495.

Hill, H. A., and Stebbins, R. T., 1975, *Astrophys. J.,* **200**, 471.

Howard, R., 1979, *Astrophys. J.,* **228**, L45.

Howard, R., and Gilman, P. A., 1986, *Astrophys. J.,* **307**, 389.

Howard, R., and LaBonte, B. J., 1980, *Astrophys. J.,* **239**, L33.

Korzennik, S. G., 1990, *Ph. D. dissertation* , Univ. of California.

Kumar, P., 1992, in PASP Conference Series, Vol. **42**, *GONG 1992: Seismic Investigation of the Sun and Stars* , ed Timothy M. Brown, 15.

LaBonte, B. J., Howard, R., and Gilman, P. A., 1981, *Astrophys. J.,* **250**, 796.

Latour, J., Toomre, J., Zahn, J.-P., 1983, *Solar Physics* , **82**, 387.

Leibacher, J. W., and Stein, R. F., 1971, *Astrophys. Lett.*, **7**, 191.

Leighton, R. B., Noyes, R. W., and Simon, G. W., 1962, *Astrophys. J.,* **135**, 471.

November, L. J., Toomre, J., Gebbie, K. B., and Simon, G. W., 1981, *Astrophys. J.,* , **245**, L123.

Ogura, Y., and Phillips, Na. A., 1962, *J. Atmos. Sci.*, **19**, 173.

Parker, E. N., 1955a, *Astrophys. J.,* **121**, 491.

Parker, E. N., 1955b, *Astrophys. J.,* **122**, 293.

Parker, R. L., 1977, *Ann. Rev. Earth Planet. Sci.*, **5**, 35.

Patrón, J., 1992, *Thesis Project* , University of La Laguna.

Patrón, J., Hill, F., Rhodes, E. J., Jr., Korzennik, S. G., Cacciani, A., and Brown, T. M., 1992, in PASP Conference Series, Vol. **42**, *GONG 1992: Seismic Investigation of the Sun and Stars* , ed Timothy M. Brown, 437.

Press, W. H., Teukolsky, S. A., Vetterling, W. T., Flannery, B. P. 1986, in *Numerical Recipes in FORTRAN* , Chapter 10 (Cambridge University Press), 289.

Rast, M.P., and Toomre, J., 1993, *Astrophys. J.,* **419**, 224 and 240.

Rhodes, E. J., Jr., Ulrich, R. K., and Simon, G. W., 1977, *Astrophys. J.,* **218**, 901.

Schröter, E. H., Wöhl, H., Soltun, D., and Vázquez, M., 1978, *Solar Physics* , **60**, 181.

Severny, A. B., Kotov, V. A., and Tsap, T. T., 1976, *Nature* , **259**, 87.

Simon, G. W., and Leighton, R. B., 1964, *Astrophys. J.,* , **140**, 1120.

Simon, G. W., and Weiss, N. O., 1968, *Z. F. Astrophy.*, **69**, 435.

Smart, W. M., 1971, *Textbook on Spherical Astronomy* (5th ed.; Cambridge: Cambridge University Press), 174.

Snodgrass, H. B., 1984, *Solar Physics* , **94**, 13.

Snodgrass, H. B., and Howard, R., 1984, *Astrophys. J.,* **284**, 848.

Spiegel, E. A., and Veronis, G., 1960, *Astrophys. J.,* **131**, 442.

Stix, M., 1991, in *The Sun, An Introduction* , ed. M. Harwit, R. Kippenhahn, V. Trimble, J.-P. Zahn, (Springer-Verlag), Chap. 6, 194.

Ulrich, R. K., 1970, *Astrophys. J.,* **162**, 993.

Unno, W., Osaki, Y., Ando, H., and Shibahashi, H., 1989, *Nonradial Oscillations of Stars* (Tokyo: University of Tokyo Press).